UNIVERSITI SAINS MALAYSIA

Laporan Akhir Projek Penyelidikan Jangka Pendek

Magnetophoretic Actuation Of Surface Functionalized Magnetic Nanoparticle(s) For Defouling Of Polymeric Membrane

by
Dr. Low Siew Chun
Prof. Abdul Latif Ahmad
Dr. Lim Jit Kang
Dr. Ooi Boon Seng

2014

BORANG ERGS – P3(R)

Kod Projek : 203/PJKIMIA/6730013

KEMENTERIAN PENDIDIKAN MALAYSIA

FINAL REPORT
EXPLORATORY RESEARCH GRANT SCHEME (ERGS)
Laporan Akhir Skim Geran Penyelidikan Eksploratori (ERGS) IPT
2014

A

PHASE : **FASA 1 - 2011**
Fasa

RESEARCH TITLE : **Magnetophoretic Actuation of Surface Functionalized Magnetic Nanoparticle(s) for Defouling of Polymeric Membrane**
Tajuk Penyelidikan

PROJECT LEADER : **Dr. Low Siew Chun**
Ketua Projek

PROJECT MEMBERS (including GRA) :
1. **Prof. Abdul Latif Ahmad**
2. **Dr. Lim Jit Kang**
3. **Dr. Ooi Boon Seng**

Ahli Projek

PROJECT ACHIEVEMENT *(Prestasi Projek)*

B

ACHIEVEMENT PERCENTAGE			
Project progress according to milestones achieved up to this period	**0 - 50%**	**51 - 75%**	**76 - 100%**
Percentage			√

RESEARCH OUTPUT		
Number of articles/ manuscripts/ books *(Please attach the First Page of Publication)*	**Refereed Journal**	***Non-Refereed Publication***
	4 (published) **2** (submitted - under review)	
Conference Proceeding *(Please attach the First Page of Publication)*	**International**	***National***
	3	
Intellectual Property *(Including Paten,Copyright, Industrial Design,layout Design of Integrated Circuit & Trademarks)*		

HUMAN CAPITAL DEVELOPMENT

Human Capital	**Number**				**Others** (please specify)
	On-going		**Graduated**		
Citizen	Malaysian	Non Malaysian	Malaysian	Non Malaysian	PhD Student: 1. Mr. Ng Qi Hwa Master Student: 1. Ms. Nur Atiah binti Azmi Undergraduate Student: 1. Mr. Ng Qi Hwa 2. Ms. Norfa'eizen binti Abdul Rahim Neyu
PhD Student	1				
Master Student			1		
Undergraduate Student			2		
Total	1		3		

EXPENDITURE *(Perbelanjaan)*

C

Budget Approved *(Peruntukan diluluskan)* : **RM 150,100.00**
Amount Spent *(Jumlah Perbelanjaan)* : **RM 150,096.86**

Balance *(Baki)* : **RM 3.14**
Percentage of Amount Spent : **99.99 %**
(Peratusan Belanja)

ADDITIONAL RESEARCH ACTIVITIES THAT CONTRIBUTE TOWARDS DEVELOPING SOFT AND HARD SKILLS
(Aktiviti Penyelidikan Sampingan yang menyumbang kepada pembangunan kemahiran insaniah)

D

International

Activity	Date (Month, Year)	Organizer
1) International Conference on Membrane Science and Technology	August 2012	Prince of Songkla University, Thailand
2) International Membrane Science & Technology Conference	November 2013	Membrane Society of Australasia (MSA), Melbourne, Australia
3) International Conference on Membrane Science and Technology	August 2013	Universiti Teknologi Malaysia, Malaysia

National

Activity	Date (Month, Year)	Organizer
(e.g : Course/ Seminar/ Symposium/ Conference/ Workshop/ Site Visit)		

PROBLEMS / CONSTRAINTS IF ANY *(Masalah/ Kekangan sekiranya ada)*

E

The project was performed well for the past 2.5 years with 7 paper publications (4 journals and 3 proceeding papers). Due to the budget constraint (allocated fund is ~ 50% of original proposal), we could only carried out the filtration performance study based on the dead-end cell set-up, without looking at the effects of cross-flow velocity.

RECOMMENDATION (*Cadangan Penambahbaikan*)

F

RESEARCH ABSTRACT – Not More Than 200 Words (*Abstrak Penyelidikan – Tidak Melebihi 200 patah perkataan*)

G

In the project, the highly monodispersed magnetite (Fe_3O_4) colloids were successfully produced via co-precipitation method, where its outer layer were functionalized using negatively charged polyacrylic acid (PAA). The as-made negatively charged PAA-MNPs colloids were then spin coated onto the surface of polysulfone (PSF) membrane through non-covalent interaction, with the exits of potassium persulfate (PP) as initiator. In current work, we combined both the functionality (hydrophilic and negatively charged of the PAA-MNPs colloids that repelled the same negatively charged humic acid, HA) as well as the mechanical (actuation of MNPs on the membrane surface) properties of the magnetic nano-colloids in suppressing the membrane fouling. The combinatorial role of MNPs and polymeric membrane in membrane defouling was then evaluated through ultrafiltration, based on its permeation and rejection performances. The membrane was found to have lower deposition of HA when the magneto ration motion was introduced. The success gentle rocking of these magnetite particles within the membrane structure by an externally applied magnetic field has help in mitigates the membrane fouling and increases the life time of the membrane. These findings have proved the practicability of this novel magnetite augmented polymeric membrane in removing organic foulant from the wastewater sources.

Please refer to attached document for the detail technical report.

Date : **15 February 2014**
Tarikh

Project Leader's Signature:
Tandatangan Ketua Projek

Dr. Low Slew Chun
Senior Lecturer
School of Chemical Engineering
Universiti Sains Malaysia

COMMENTS, IF ANY/ ENDORSEMENT BY RESEARCH MANAGEMENT CENTER (RMC)
(Komen, sekiranya ada/ Pengesahan oleh Pusat Pengurusan Penyelidikan)

H

Good output.

Name:
Nama:

Signature:
Tandatangan:

Date:
Tarikh: 7/3/14

PROF. MADYA LEE KEAT TEONG
Pengarah
Pejabat Pengurusan & Kreativiti Penyelidikan
Universiti Sains Malaysia
11800 USM, Pulau Pinang.

KEMENTERIAN PENDIDIKAN MALAYSIA

UNIVERSITI SAINS MALAYSIA

LAPORAN TEKNIKAL
SKIM GERAN PENYELIDIKAN EKSPLORATORI (ERGS)

TAJUK:
MAGNETOPHORETIC ACTUATION OF SURFACE FUNCTIONALIZED MAGNETIC NANOPARTICLE(S) FOR DEFOULING OF POLYMERIC MEMBRANE (A/C NO: 6730013)

Abstract

In the project, the highly monodispersed magnetite (Fe_3O_4) colloids were successfully produced via co-precipitation method, where its outer layer were functionalized using negatively charged polyacrylic acid (PAA). The as-made negatively charged PAA-MNPs colloids were then spin coated onto the surface of polysulfone (PSF) membrane through non-covalent interaction, with the exits of potassium persulfate (PP) as initiator. In current work, we combined both the functionality (hydrophilic and negatively charged of the PAA-MNPs colloids that repelled the same negatively charged humic acid, HA) as well as the mechanical (actuation of MNPs on the membrane surface) properties of the magnetic nano-colloids in suppressing the membrane fouling. The combinatorial role of MNPs and polymeric membrane in membrane defouling was then evaluated through ultrafiltration, based on its permeation and rejection performances. The membrane was found to have lower deposition of HA when the magneto ration motion was introduced. The success gentle rocking of these magnetite particles within the membrane structure by an externally applied magnetic field has help in mitigates the membrane fouling and increases the life time of the membrane. These findings have proved the practicability of this novel magnetite augmented polymeric membrane in removing organic foulant from the wastewater sources.

Selective Research Findings:

Objective 1: To synthesize highly monodispersed magnetite (Fe_3O_4) colloids

Precipitation agent plays an important role in the MNPs formation as they provide the base agent (OH^- group) need to complete the precipitation process. Two types of precipitation agent i.e ammonium hydroxide (NH_4OH) and sodium hydroxide (NaOH) were prepared at different pH condition. The pH for both NH_4OH and NaOH were first being adjustedusing 0.05M NaOH and 0.05M HCL prior added into with the Fe^{2+} and Fe^{3+}reaction mixture. It was observed that, different precipitate colour were obtained when co-precipitation process carried under the different pH conditions for both types of precipitation agents. Black precipitate solutions were observed at pH11.0 and pH12.0 for NH_4OH in Figure 1 and pH14.0 for NaOH in Figure 2. These black solutions were shown to have magnetophoretic responses when exposed to the external magnetic field (magnetic bar). In this regards, the synthesized MNPs were expected to be able to perform the magneto rotation motions when bound on the membrane surface and further detached the foulants away from the membrane surface.

By close observation on both Plates 4.1 and 4.2, the clear yellow solutions were observed throughout the reaction of NH_4OH at pH9.0 and pH10.0 (Plate 4.1) and NaOH from pH9.0 to pH13.0 (Plate 4.2). These yellow colour solutions were the MNPs intermediate form due to insufficient OH^- ion in precipitation agent. This intermediate forms were expected to change to the black colour if the precipitation agent was continuously added to the process until the OH^- ions were sufficient to

precipitate MNPs. Knowing that, NaOH solution contain higher alkalinity than NH_4OH solution with the same molarities. Thus, the use of NaOH is supposed to produce a better quality of MNPs. However the use of strong alkaline media such as NaOH, can caused the formation of non-magnetic iron compound (Gnanaprakash *et al.*, 2007) such as α-FeOOH and other ion compounds (Martínez-Mera *et al.*, 2007).

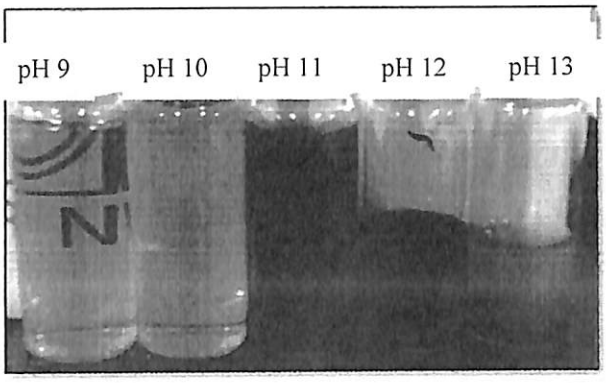

Figure 1: MNPs prepared at different pH of ammonium hydroxide (NH_4OH)

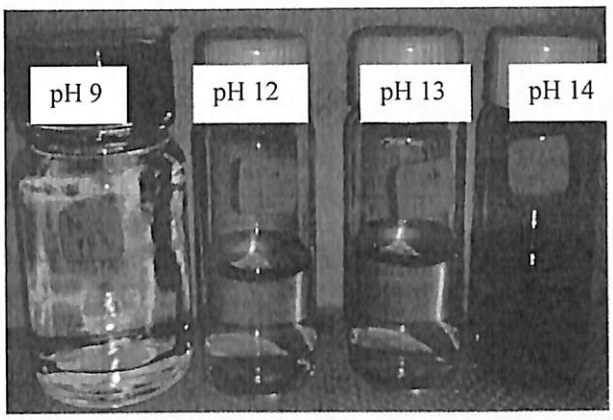

Figure 2: MNPs prepared at different pH of sodium hydroxide (NaOH)

When the magnetophoretic MNPs were formed, intermolecular repulsion between the nanoparticles should exist and create smaller hydrodynamic diameter. Unfortunately, when NH_4OH was used as the precipitation agent in co-precipitation process, the particles showed both highest and lowest of hydrodynamic diameter (Figure 3) at pH11.0 to pH12.0, respectively. The MNPs showed the average hydrodynamic diameter (Figure 3) of 1046.4nm ± 200.0 at pH11.0 and only 132.1nm ± 0.6 at pH12.0. MNPs carry negative surface charge at pH higher than its isoelectric point (Hu *et al.*, 2010, Illés and Tombácz, 2006). For MNPs formed at pH11, we suspect although the black colour solution was formed; the magnetophoretic properties were not high. In turns, less repulsion occurred and agglomeration happened.

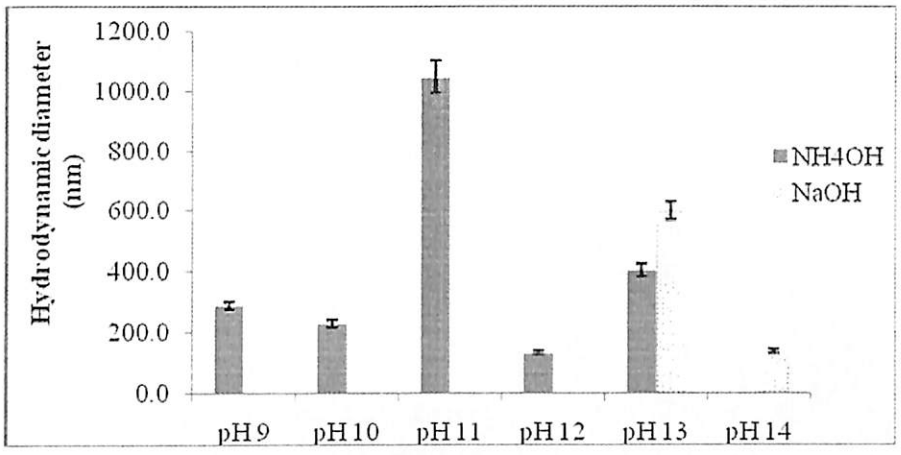

Figure 3: Hydrodynamic diameter of MNPs synthesized at different pH ratio and precipitation agent. Error bar indicates the standard deviation

As for NaOH, MNPs were only able to produce at pH14.0. As mentioned earlier, the strong base NaOH created non-magnetic iron compound such as α-FeOOH. In this regard, more OH^- ions are needed to produce the magnetophoretic MNPs. This is why when NaOH was used as the precipitation agent, the higher pH value was required. In Figure 3, NaOH solution at pH below 12 resulted to have low density of ions OH^-, thus, restricted the formation of magnetic responsive nanoparticles and maintained as intermediate form of solutions. At pH13.0, the non-magnetic iron compound started to form and responded to the higher hydrodynamic diameter and PDI values. When the reaction was prepared at pH14.0, the magnetically responsive MNPs (black colour of solution) formed. At pH14.0, the produced MNPs appeared in small hydrodynamic diameters of 134.2nm ± 2.3 and low PDI of 0.345 ± 0.012. Under the consideration of small hydrodynamic diameter and low PDI, both NH_4OH and NaOH gave similar characteristics to produced MNPs. In this study, NH_4OH was selected as precipitation agent for further study since lower pH condition (pH12.0) was preferred for membrane filtration process.

The precipitation agent (NH_4OH) volumes were then varied to 10mL and 25mL. When different volumes of NH_4OH were used to prepare MNPs at pH12, the synthesized MNPs were produced at different hydrodynamic diameter, as shown in Figure 4. The results show that, MNPs produced by using 25mL of NH_4OH exhibited lower hydrodynamic diameter than the MNPs produced by using 10mL of NH_4OH. The reaction mechanism when NH_4OH is employed as the precipitation agent is shown in Equation 1. The NH_4OH will ionize to NH^{4+} ions and OH^- ions. The OH^- ions responsible for the precipitation of the Fe^{3+} and Fe^{2+} ion resulting in the formation of Fe_3O_4 nanoparticles. Basically, 25mL of NH_4OH tends to have more OH^- ions compared to 10mL of the same NH_4OH stock solution. This explains the lower hydrodynamic diameter and PDI value obtained at higher volume of NH_4OH solution.

$$NH_4OH \leftrightarrow NH_4^+ + OH^- \qquad \text{(Eqn. 1)}$$

Besides, a more stable hydrodynamic diameter (Figure 4) trend was observed when 25mL of NH_4OH was used as the precipitation agent. It was because in the 10mL of NH_4OH, the OH^- ions were insufficient to react with the available Fe^{3+} and Fe^{2+} ion. Therefore, this excess Fe^{3+} and Fe^{2+} in the solution caused this unstable trend and further increased the PDI value due to the production of intermediate forms and the aggregation between the particles.

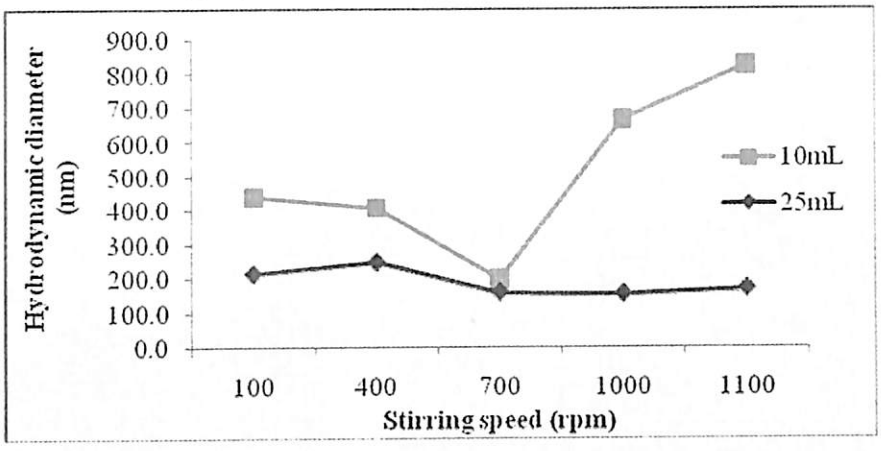

Figure 4: Hydrodynamic diameter of MNPs synthesis using NH_4OH as precipitation agent at pH12.0 and at different volume

Figure 5(a) and (b) shows TEM micrograph of MNPs synthesis at stirring speed of 1000rpm using 25mL of NH_4OH and NaOH respectively. The micrographs show the morphology of agglomerated MNPs, their shapes and size distribution. The MNPs prepared using NH_4OH was observed to be spherical in shape and homogeneous size distribution with mean size of 7nm. The MNPs obtained in Figure 5(b) showed less homogeneous particle size distributiondue to the formation of other compounds when synthesized using NaOH.

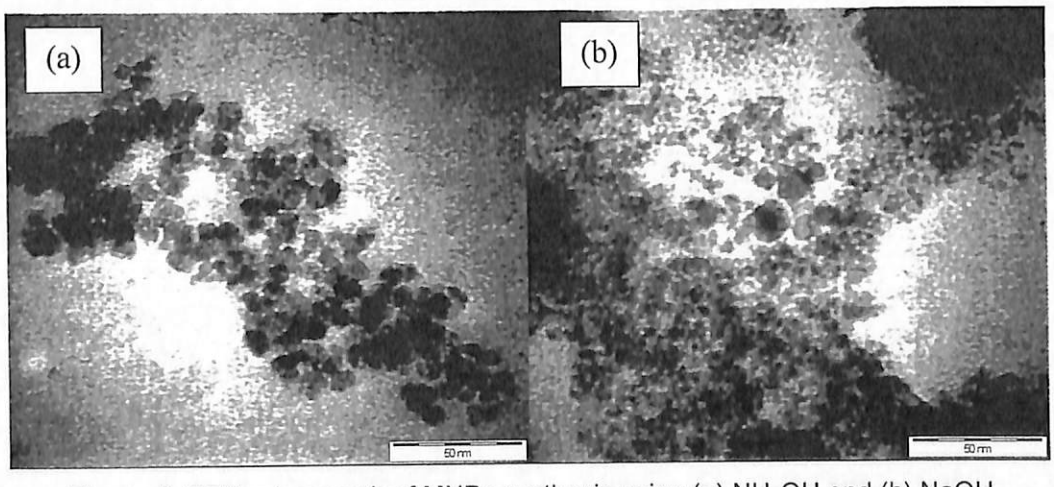

Figure 5: TEM micrograph of MNPs synthesis using (a) NH_4OH and (b) NaOH

Stability is of utmost importance in the storage of ferrofluids. Magnetite nanoparticle (MNPs) could easily aggregate and formed large clusters due to their hydrophobic surfaces with a large

surface area-to-volume ratio. As shown in Figure 6, the bare MNPs carried hydrodynamic diameters of 376.7nm ± 90.4 and polydispersity index (PDI) of 0.500 ± 0.130. In order to achieve sufficient repulsive interactions so as to obtain a stable colloidal solution, the present of proper surface coating is crucial. The stabilizing mechanism proposed here is to partition a carboxylate group coating around the surface of MNPs. The polymer carboxylic functional groups were exposed around the surface of MNPs when the PAA polymer was interacted with the MNPs colloids through physiosorption process.

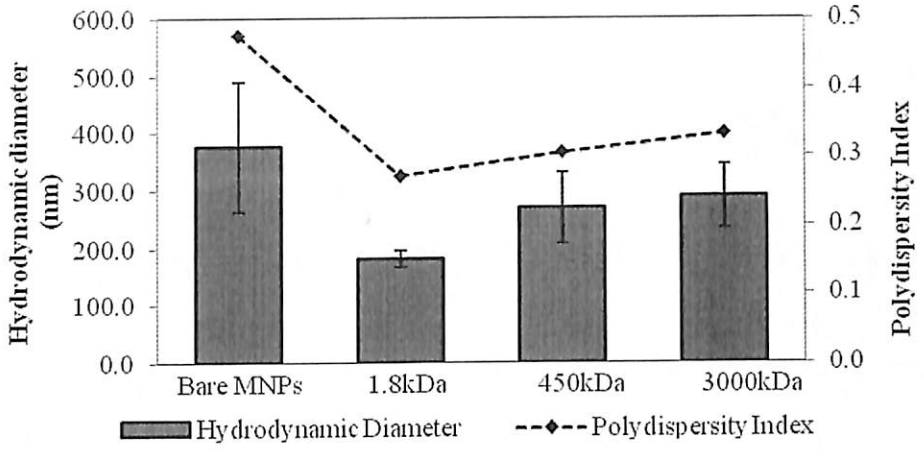

Figure 6: Hydrodynamic diameter and polydispersity index of MNPs functionalized using different polyacrylic acid (PAA) polymer at 1wt% of polymer concentration and pH6.0

PAA with carboxylate group was expected to be able to help to increase the MNPs water solubility (Erban and Chapman, 2007). Generally, PAA-MNPs composite have been shown to have lower hydrodynamic diameter and PDI compared to bare MNPs (Figure 6). This result demonstrated that PAA efficiently coated onto MNPs particle surfaces. The presence of negatively charged polyelectrolytes (PAA) coated on the MNPs surface has enhanced the steric and electrostatic repulsion that prevents the agglomeration of particles. The steric stabilization factor induced by this coated polyelectrolyte strongly dictated the colloidal stability, leads to the decrease of their hydrodynamic diameter and PDI (Ghosh *et al.*, 2011).

When the lowest molecular weight of PAA (1.8kDa) was employed to passivate the surface of the iron oxide, the functionalized MNPs were showed to have the lowest hydrodynamic diameter and PDI of 180.0nm ± 14.2 and 0.271 ± 0.020, respectively. It means, 1.8kDa molecular weight of PAA have enough repulsive forces to overcome the attractive forces acting on the MNPs. PAA polymer compositions were kept constant at 1wt% throughout this study. Therefore, increasing in the PAA molecular weight will increase the viscosity of the suspension. A higher viscosity enhances the formation of dense layer that wraps around the surface of iron oxide. Thus, MNPs functionalized using 450kDa and 3000kDa demonstrated larger hydrodynamic diameter (268.7nm ± 61.2 and 289.3nm ± 55.4, respectively) and PDI values (0.305 ± 0.040 and 0.333 ± 0.003), respectively. These PAA dense layers at 450kDa and 3000kDa will give the adverse effects, which attract each

other by the strong carboxylic groups of PAA and further lead to coagulation. It might be due to chained-up effects caused by the longest chain of PAA at high molecular weight that interact with more than one iron oxide particle. The stability of the MNPs suspension could be affected by the chain length of coated polymer. The use of polymer with extremely low molecular weight might only able to coat a thin film layer which in fact will increase their aggregation kinetic due to the Van der Waals attractive forces. The extremely high molecular weights of polymer, on the other hand might cause the polymer begin to bridge between the particles and aggregated to form cluster (Ditsch *et al.*, 2005). This explains why the larger hydrodynamic diameter and PDI value for the PAA-MNPs composite were observed when the higher molecular weight of PAA was utilised (Figure 6).

The coated yield of PAA on the MNPs surface was further determined using thermogravimetric analysis (TGA). Figure 7 illustrates TGA curves of MNPs samples prepared at different PAA molecular weight, revealing a decrease in amount of weight loss with increasing reaction time. There are two phase of weight loss. The first phase occurred at around 100°C due to the water loss. The second phases continued at 230°C referred to the weight loss of MNPs functionalized using 1.8kDa, 450kDa, and 3000kDa of PAA, showed to have weight remains of 53.20wt%, 48.95wt% and 20.05wt%, respectively (Figure 7). No significant weight changes observed after 350°C for all three samples due to the presence of only MNPs after 350°C. The degradation temperature obtained from this research was comparable with the findings from other researchers where the major weight loss of PAA was found at the temperature of 250°C (Nguyen and Shim, 2012) and 260°C (Chen and Huang, 2004) when functionalized using 10wt% and 15wt% of PAA, respectively. In this study, a minor weight loss was observed due to the use of low PAA concentration (1wt%) during the functionalization process.

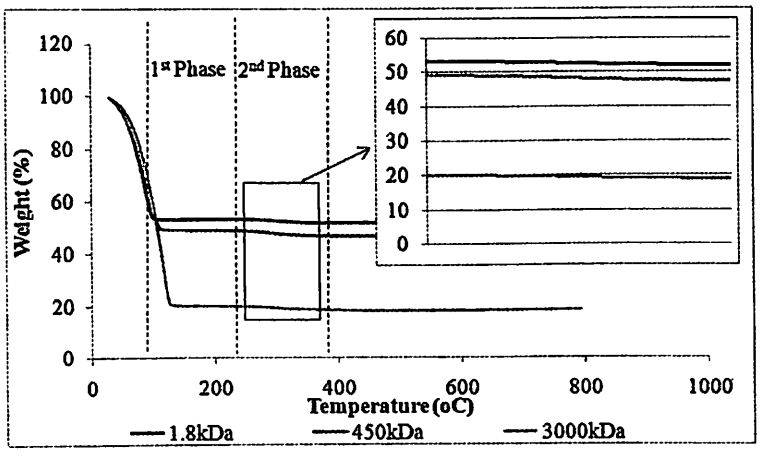

Figure 7: TGA curve PAA-MNPs composite at (a) 1.8kDa, (b) 450kDa and (c) 3000kDa

When a constant amount of PAA polymer (1wt%) used in each sample, the change in the weight loss is related to the variation of amount PAA coated on the MNPs surface. By utilizing the weight loss information from TGA, the coated amount of PAA onto MNPs could be quantified by using Equation 2.

$$\text{Amount PAA coated (mg/g MNPs)} = \frac{\text{TGA weight loss (\%)}}{\text{100-TGA weight loss (\%)}} \times 1000 \quad \text{(Eqn. 2)}$$

It was observed that the amount PAA coated on MNPs increased with the increased of PAA molecular weight (Table 1). The amounts of PAA coated onto the MNPs were 12.13mg/g MNPs, 16.73mg/g MNPs and 18.17mg/g MNPs for PAA molecular weight of 1.8kDa, 450kDa and 3000kDa, respectively. It seems that the amount of PAA polymer coated on the surface of MNPs were markedly greater when higher molecular weight of the polymer was used. The difference in amount of PAA coated on MNPs was hypothetically due to variation of their polymer long chain and density on the surface of MNPs. Moreover, carboxyl group at the higher PAA molecular weight was higher compared to the lower PAA molecular weight which could also affect the amount of polymer coated. Again, this has proved the successful coating of PAA around MNPs.

Table 1: The mass of coated PAA on functionalized MNPs

PAA molecular weight (kDa)	Mass of grafted on PAA (mg/g MNPs)
1.8	12.13
450	16.73
3000	18.17

The MNPs aggregation should be avoided for better MNPs performance in water. Therefore, the flocculation kinetic study of bare MNPs and PAA-MNPs composite was observes by dispersing 6ppm MNPs colloidal suspension in water for 16h. Figure 8 shows the flocculation kinetic of bare and functionalized MNPs. As expected, bare MNPs start to flocculate into large clusters within a few minutes as the initial hydrodynamic diameter was 333.9nm and increases up to almost 1270.0nm. Increase in the hydrodynamic diameter of the bare MNPs shows the increasing aggregation kinetics for the MNPs colloidal suspension, due to the intention to reduce the its energy associated with high surface area to volume ratio (Yeap *et al.*, 2012). Consequently, caused the aggregations of the particles and formed larger cluster.

The collision and interaction among nano-scaled structure are almost inevitable in a colloidal system with no surface modification. Here, theusing 1.8kDa PAA polymer was showed to successfully promote the colloidal stability to the MNPs,as shown by the flocculation kinetic study in Figure 8. Bare MNPs tend to interact with each other forming aggregates in order to minimize the surface energy as explained, that increasing of the hydrodynamic diameter at the beginning of the study (Lu *et al.*, 2007, Wu *et al.*, 2008). In contrast, when the MNPs were functionalized with three different molecular weight of PAA, the functionalized MNPs do not exhibit any obvious clustering behavior in the same time scale. PAA at molecular weight of 1.8kDa and 450kDa exhibited almost constant line throughout the testing time. However, PAA at 3000kDa shows the cluster formation at

the beginning of the testing time and stable after 10hrs of flocculation test at hydrodynamic diameter of 1000.0 - 1500.0nm. This was probably due to the high chain PAA polymer at 3000kDa that wrapped-up few iron oxides with its high polymer linkage. However, the MNPs that functionalized using the 3000kDa PAA polymer havesomehow demonstrated lower flocculation effect than the bare MNPs. This was mainly because of the electrostatic repulsion and steric repulsion by the PAA functionalized MNPs that caused them to disperse better in solution compared to the bare MNPs suspension (Mak and Chen, 2004).

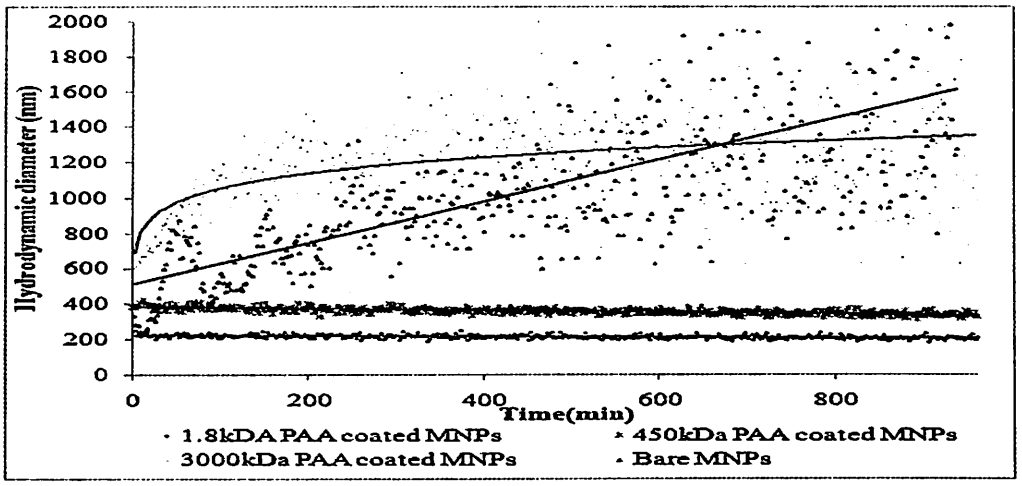

Figure 8: Flocculation kinetic profile of (a) bare MNPs, PAA-MNPs at (b) 1.8kDa, (c) 450kDa, and (d) 3000kDa

Objective 2: To integrate the as-made magnetite particles onto polymeric membrane surface through either phase inversion or covalent attachment of the magnetic particles with the cross-linking of polymer films.

The 1.8kDa PAA-MNPs composite were further mixed with potassium persulfate (PP) and PSF polymer, in preparation of the coating layer as shown in Table 2. This magnetophoretic nano-composite solution was then spin coated onto the surface of support PSF ultrafiltration membrane. The presence of this magnetophoretic nano-composite films were characterized using ATR-FTIR. Figure 9 shows the ATR-FTIR spectra of neat (uncoated) and coated PSF membrane, which confirm the magnetophoretic nano-composite thin film was deposited onto the PSF membrane. The coated PSF membrane produced new and strong absorption signal at 1670cm^{-1} which corresponded to the C=O from the carboxylic groups of PAA. In contrast, there is no C=O peak observed at neat PSF membrane. The higher intensity for the peak of 1670cm^{-1}indicates the successful coating of magnetophoretic nano-composite film (PAA-MNPs) on the PSF support membrane.

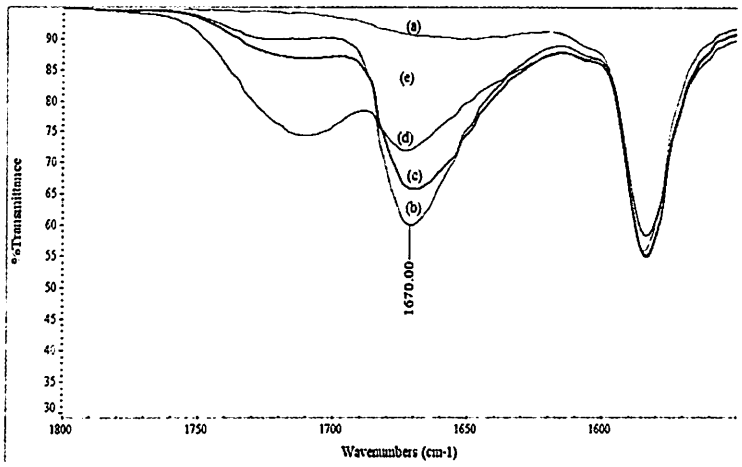

Figure 9: ATR-FTIR of (a) neat PSF membrane (b) PSF Mem-1, (c) PSF Mem-2, (d) PSF Mem-3 and (e) PSF Mem-4

The hydrophilic property of the membrane prepared at different thin film compositions were evaluated via contact angle measurements. Table 2 shows that all the PAA-MNPs coated PSF membrane demonstrated a decrease in their contact angle compared to neat PSF membrane. In this case, the additional of the hydrophilic carboxylic group from PAA was the main factor that contributed to the increased hydrophilicity of coated PSF membranes. It is presume that, the additional potassium persulfate (PP) as polymerization agent to the nano-composite solution (PSF Mem-2 and PSF Mem-4) helped to increase the amount of free carboxylic group of the PAA and further increased their hydrophilicity properties and attachment to the surface of the MNPs. The PP was acted as the polymerization initiator where PP will dissociate the H^+ and COO^- ions from the PAA polymer to further increased the free carboxyl group (from PAA) to be interacted with the ferum ions of Fe_3O_4.

Table 2: PSF membrane contact angles at different thin film nano-composite composition

Sample	Contact Angle (°)
PSF Mem-1	62.02±6.08
PSF Mem-2	48.96±1.14
PSF Mem-3	55.80±3.36
PSF Mem-4	30.92±6.42
Neat PSF membrane	78.06±0.66

The PAA-MNPs composite coated to the surface of PSF membrane should retained certain level of binding strength to ensure the magnetophoretic actuation of the iron oxide imposed by the external magnetic field. Therefore, the MNPs detachment study from PSF membrane surface was carried out. First of all, PSF Mem-2 (Table 2) was tested under continuous shaking at 90rpm with the

data taken for every 10min interval times to determine the optimum detachment level of MNPs without magneto rotation motion assistance. As expected, the higher detachment amount of MNPs obtained when a longer operating time (Figure 10) was imposed. However, the detachment phenomenon ceased when the binding strength of coated PAA composite film has overcome the flashing forces from the operating solution. The flashing force is the force produced during the shaking process.This force would able to detach the unstable MNPs that bind on the PSF membrane surface without the introduction of external magnetic field. As determined from Figure 10, the PSF Mem-2 achieved constant detachment level at time of 25min. At this saturated level, only 14% of MNPs was removed from the membrane surface. As observed (Figure 10), there was no further detachment after 25min of flashing operation which means that the PAA-MNPs coated PSF membrane has achieved the stability of binding.

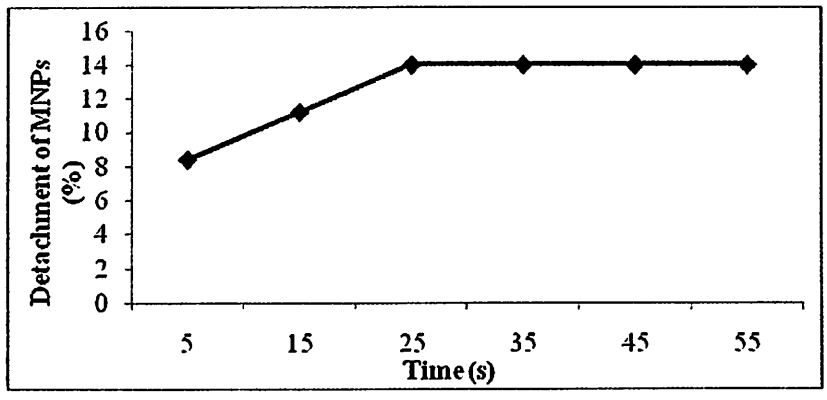

Figure 10: Detachments of MNPs from PSF membrane surface without magneto rotation motion

This saturated time of 25min was then further used as the testing time for the rest combinations of magnetophoretic nano-composite membrane (Table 2) towards detachment of MNPs from support PSF membranes. Figure 11 shows the detachment level of MNPs from the PSF membrane, at condition of without and with magneto rotation motion imposed by the external magnetic field. Among of all combination strategies of magnetite nano-composite layer coated onto PSF membranes, PSF Mem-3 (PAA-MNPs dissolved in PSF polymer) appears to have the highest detachment of MNPs. 36.64% and 67.64% of MNPs has been detached from the coated PSF membrane under conditions without and with magneto rotation motion. In contrast, coated support PSF membrane with nano-composite layer consists of PAA-MNPs mixed with potassium persulfate (PSF Mem-2) showed to have the lowest MNPs detachment of 8.46% and 11.27%, without and with magneto rotation motion, respectively. This might be due to the addition of potassium persulfate (PP) which helps the polymerization of PAA polymer and further increased the thin layer stability on the PSF membrane. The presence of this polymerization agent lead to the covalent attachment of the MNPs to PAA matrix and strengthen the interaction between the nanoparticle and polymer network and decrease the detachment of MNPs from PSF membrane surface. In the research carried by Madaeni *et al.* (2011), the presence of PP as polymerization agent was found to enhance the

interaction between carboxylic group of acrylic acid and the nanoparticle surface, which lead to minimizing the agglomeration and further strengthen the bonding between the nanoparticles and polymer matrix.

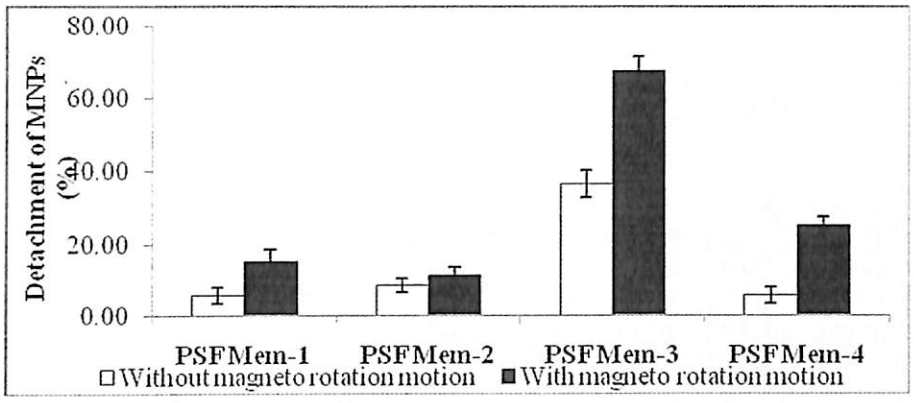

Figure 11: Detachment of MNPs from PSF membrane surface without and with magneto rotation motion at different thin layer solution composition

The concentration of MNPs coated on the membrane surface would affect their antifouling performance. Hypothetically, increasing in MNPs concentration will increase the MNPs actuation probability on the membrane surface. Where, at higher MNPs actuation, more HA could be removed from the membrane surface. In this study the MNPs concentrations were varied from 0.01wt%, 0.05wt% and 0.10wt%. Figure 12 show that, MNPs concentration at 0.01wt% appears to have lowest MNPs detachment level with 25.37% of MNPs detached from the membrane surface. While the highest detachment level obtained at 33.82% of MNPs detachment was observed at 0.10wt% of MNPs concentration. The higher detachment obtained at higher MNPs concentration might be due to the increase of MNPs concentration deposited onto membrane during coating process. However, the increase in MNPs concentration might increase the possibility of MNPs actuation motion that enhances the detachment of humic acid from the membrane surface.

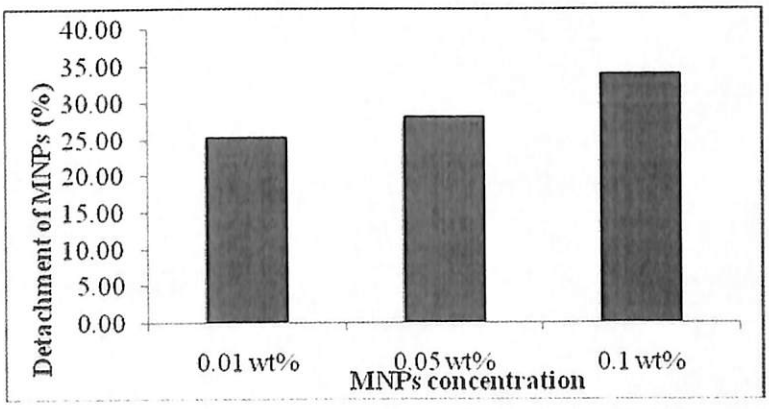

Figure 12: Detachments of MNPs from PSF membrane and with magneto rotation motion at different magnetite nanoparticles concentration

FESEM micrograph (Figure 13) was further employed to observe the MNPs distribution pattern on the membrane surface. At certain conditions, MNPs tends to aggregate which affect the arrangement and uniformity on the membrane surface.

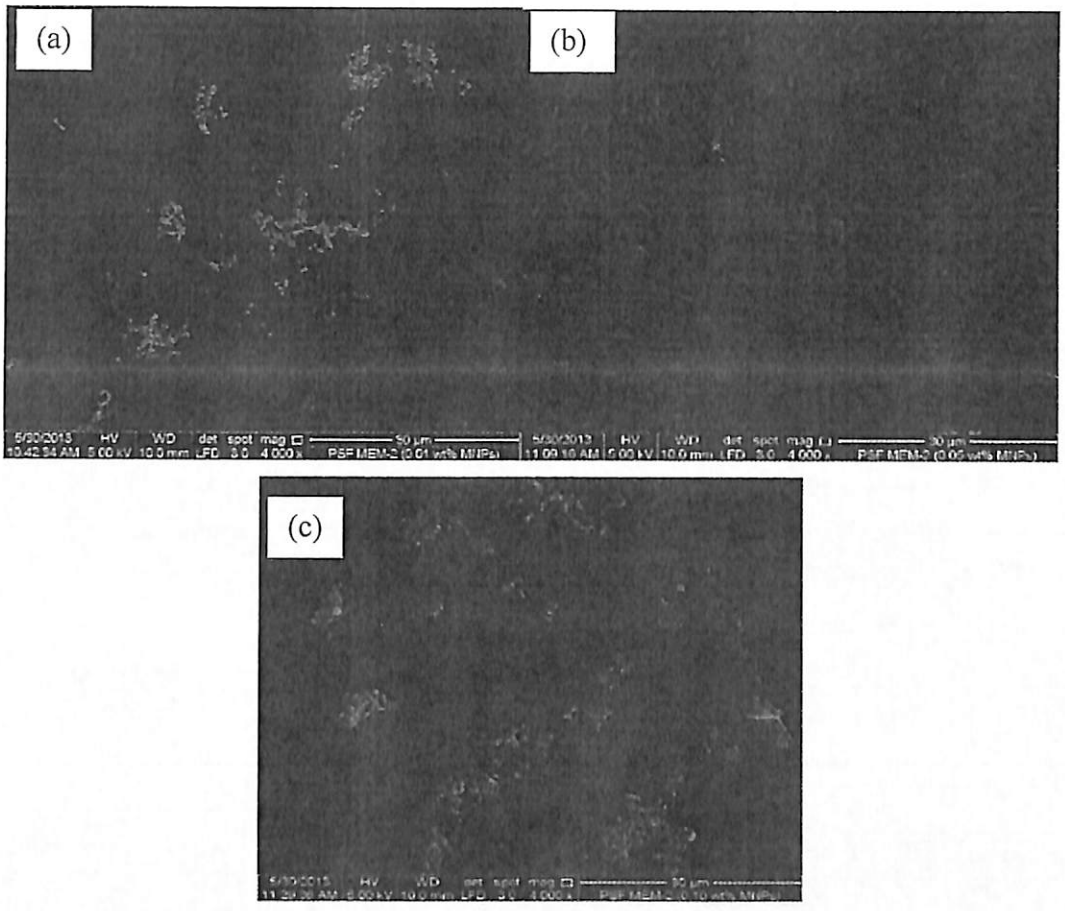

Figure 13: FESEM micrographs of nano-composite membrane (a) 0.01wt%, (b) 0.05wt% and (c) 0.10wt% of MNPs concentration

A uniform MNPs distribution on the membrane surface will secure a better antifouling performance. It was found that, MNPs concentration of 0.05wt% (Figure 13b) distributed in more uniform MNPs arrangement on the membrane surface compared to the other two conditions (Figure 13a and c). The MNPs was not well distributed (Figure 13a) on the membrane surface although a very low concentration was employed (0.01wt%). Figure 13a showed a lot of uncoated membrane space and MNPs agglomerate in the coated area. This uncoated space and MNPs aggregation in the coated area was due to the use of high PAA concentration (1wt%) at low MNPs concentration (0.01wt%) which produced high PAA viscosity and cause the formation of the bridging effect in between PAA polymer prior to surface coating. The aggregated particles could not be re-suspended after washing (Golas *et al.*, 2010). Meanwhile, the membrane prepared at 0.10wt% MNPs concentration (Figure 13c) appeared to have more MNPs coated onto membrane surface but less in particle uniformity due to the particles agglomeration. The MNPs colloids were initially well dispersed

in the thin film solution but MNPs suspension start to agglomerate and form big clusters on the membrane to reduce its surface energy during the drying process.

Objective 3: To employ and design the magnetite augmented polymeric membrane module to treat humic substances contaminated water.

To investigate the effectiveness of the magnetite nano-composite membrane (sample 1), an in-house fabricated magnetic field rotator connected to a magnetic source and a programmable logic controller (PLC) rotator was designed, as shown in Figure 14. During the filtration process, the PLC controlled rotator was set to change the position of the magnet field source every 30s. The introduction of the magneto-induced rotation motions helped in aligning the MNPs in a single direction at the specific interchange position. The changing position of the magnetic field would promote the magnetophoretic actuation of MNPs colloids on the membrane surface and further detach the foulants from the membrane surface (Figure 14). After 13h, both membrane samples were then dried under room condition for 24h prior to further characterization using ATR-FTIR (Nicolet iS10, USA) to determine the fouling level of humic acid deposited onto the magnetite nano-composite membrane.

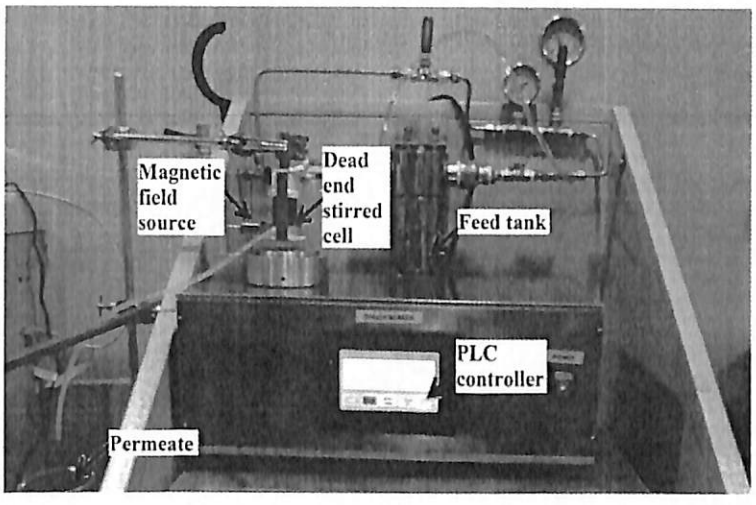

Figure 14: Magnetite augmented polymeric membrane module

Objective 4: To investigate the defouling mechanism of magnetic augmented polymeric membrane by fine tuning the physical properties of nanoparticles used the working conditions of the water purification process

Since PSF Mem-2 appeared to be the highest potential membrane with antifouling property, it was tested at both conditions with and without the magneto rotation motion. The ATR-FTIR of magnetite nano-composite membranes (PSF Mem-2) at conditions before and after HA immersion

tests were compared, as shown in Figure 15. From preliminary results, the aromatic rings of C=C bending at 1583cm^{-1} was the main constituent for HA molecule skeleton. It is expected that the fouled membrane should have higher intensity at this peak. On the other hand, the peak intensity at wavenumber 1670cm^{-1} which attributed to the C=O stretching of PAA is expected to become weaker when higher HA was fouled and covered on the membrane surface.

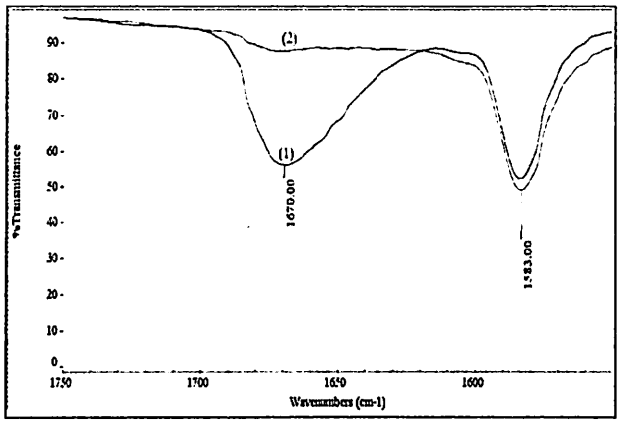

Figure 15: ATR-FTIR spectra of (1) clean PSF Mem-2 and (2) fouled PSF Mem-2 after immersion in HA at condition without magneto rotation motion

It was observed that, a broader peak at 1583cm^{-1} which represent HA appeared to become stronger, while the peak at 1670cm^{-1} becomes weaker after immersion in HA without magneto rotation motion, as shown in Figure 4.20.This means, the membrane surface (PSF Mem-2) was seriously fouled by the HA substances when there was no magneto rotation motion of MNPs was applied. The foulant was easily deposited onto the static surface of the magnetite nano-composite PSF membrane (PSF Mem-2). The fouling observations on Figure 15 was further quantitatively tabulated based on the area of peaks at 1670cm^{-1}(C=Ostretching of PAA) and 1583cm^{-1}(C=C bending of aromatic HA substances), as shown in Table 3. The area of peak at 1670cm^{-1} has reduced from 7.580 to 0.413 and the area of peak at 1583cm^{-1} was increased from 4.039 to 4.880 when the clean PSF Mem-2 was immersed in HA solution. In this case, the HA fouling occurred on the PSF Mem-2 surface with no MNPs actuation.

Table 3: Peak area of clean PSF Mem-2 and PSF Mem-2 after immersion in HA at condition without magneto rotation motion

	Area of peak 1670cm^{-1}	**Area of peak 1583cm^{-1}**
Clean PSF Mem-2 membrane	7.580	4.039
PSF Mem-2 membrane after immersion in HA at condition without magneto rotation motion	0.413	4.880

It was expected that, magneto rotation motion could increase the MNPs actuation and reduce the HA fouling on the membrane surface. Thus, in this study, the membrane antifouling performance was further investigated by introducing the external magnetic force toward the MNPs colloid that binds to the PSF Mem-2, as presented in Figure 16. Figure 16 shows the ATR-FTIR spectrum of PSF Mem-2 in condition with (sample 1) and without magneto rotation motion (sample 2). In this case, a significant stronger peak of C=O stretching (1670cm^{-1}) of PAAand slightly lower intensity at the peak of 1583cm^{-1} were observed at sample 1. This means, more C=Ostretching of PAA was observed and less C=C bending of aromatic HA group at 1583cm^{-1} was found on the membrane, which indicating less HA fouling.

The peak area of PSF Mem-2 after immersion in HA with the magneto rotation motion was also quantitatively tabulated based on the area of peaks at 1670cm^{-1}(C=O stretching of PAA) and 1583cm^{-1} (C=C bending of aromatic HA substances), as shown in Table 4. In contrast to Table 3, the PSF Mem-2 membrane shown to have significantly improved antifouling properties when induced of the MNPs actuation by the external magnetic field. From Table 4, the PSF Mem-2 at condition with magneto rotation motion showed to have the area of peak 1670cm^{-1}at 4.949 and 1583cm^{-1} at 4.249, respectively. The large area of peaks at 1670cm^{-1} implicated higher HA foulant was successfully removed from the PSF Mem-2 membrane surface at condition with MNPs actuation. Moreover, as compared to the PSF Mem-2 membrane at condition without magneto rotation motion (Table 3), the membrane with MNPs actuation has shown a much smaller area of peak at 1583cm^{-1}, which was relatively comparable to the peak area of the clean PSF Mem-2 membrane (Table 3). This result proved the magneto rotation motion could improve the membrane antifouling behaviour by the actuation of MNPs, which in turn imposed a twisting effect that promoted the detachment of HA from membrane surface.

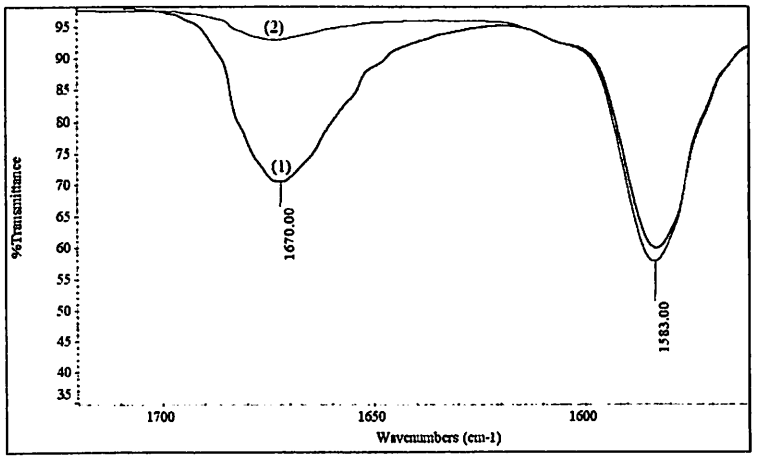

Figure 16: ATR-FTIR spectra of PSF Mem-2 at conditions (1) with and (2) without magneto rotation motion

Table 4: Peak area of PSF Mem-2 after immersion in HA at condition with magneto rotation motion

	Area of peak $1670cm^{-1}$	Area of peak $1583cm^{-1}$
PSF Mem-2 membrane after immersion in HA at condition with magneto rotation motion	4.949	4.249

Objective 5: To understand the combinatorial role of magnetite particles and polymeric membrane in membrane defouling

Flux recorded throughout the filtration run in Figure 17 shows the change in water flux at different operating pressure. The experiments were run over period of 30min. Flux at operating pressure varied from 0.5 bar to 3.0 bar was calculated according to Equation 3. It was observed that, the fluxincreased with increases in the operating pressure from 0.5 bar to 2.0 bar. The increase of the operating pressure has raised the driving force in ultrafiltration process, where increases in the driving force would help the transport of solute across the membrane and further higher flux.

$$\text{Flux, } J_w = \frac{\Delta V}{t \times A_{eff}}; \Delta V = V_2 - V_1 \qquad \text{(Eqn. 3)}$$

J_w, ΔV, Δt and A_{eff} are the pure water flux, filtrate volume, time and membrane effective area, respectively.

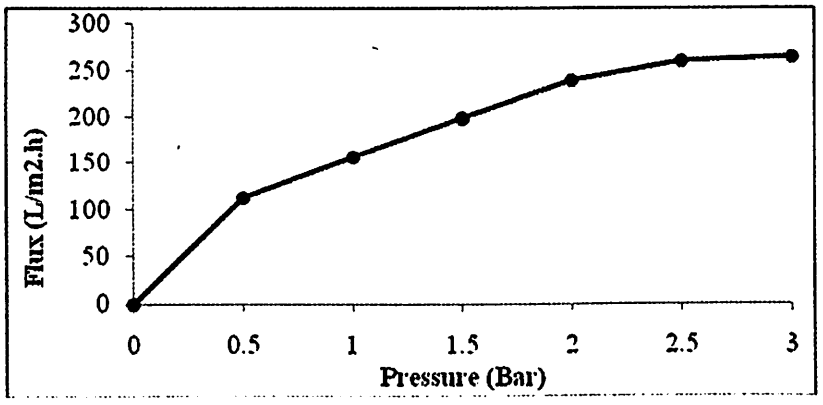

Figure 17: Neat PSF membrane flux in pure water at different operating pressure

In order to observe the fouling phenomenon, the study on the pure water flux as a function of time was shown in Figure 18. The studies were performed by using the same neat PSF membrane as the operating pressure was increased from 0.5 bar to 3.0 bar for every 30 min throughout the study. The membrane flux was decreasedregardless of the operating pressure were observed, means some extends of fouling wereoccurred. This might be due to the impurities that were present in the distilled water which used as the feed solution. It was observed that at the operating pressure of 2.5 bar and 3.0 bar, the increment of driving force through the membrane was not significant. There was not much difference in terms of flux at these particular pressures (261.65L/m^2h at 2.5 bar

and 265.47 L/m^{2}h at 3.0 bar). In this regards, operating pressure of 2.0 bar was selected to study the flux of neat PSF membrane and magnetite nano-composite membrane (PSF Mem-2) in humic acid (HA) because of the high flux, at relatively lower pressure.

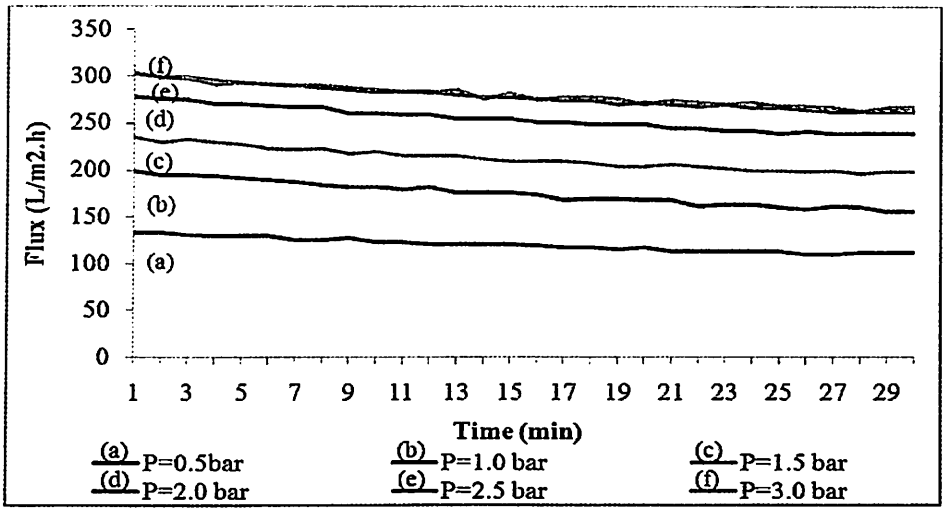

Figure 18: Flux of neat PSF membrane in pure water at different operating time

Humic acid was then used as the feed in this ultrafiltration study. A 50ppm of freshly prepared HA solution at ~pH 7.5 was prefiltered by using 0.45 µm filter paper. Flux as a function of time for neat PSF membrane and PSF Mem-2 were shown in Figure 19. As for the neat PSF membrane, the highest flux was obtained at 168.88L/m^{2}h. The neat PSF membrane started to foul at the early of filtration process. This was due to the high HA solution concentration (50ppm) used as the feed source. It was observed that, the PSF Mem-2 appeared to have relatively higher flux of 232.05L/m^{2}h when the magneto rotation motion was introduced during the filtration process. Similar to the neat PSF membrane, the flux started to reduce at the beginning of the filtration. First of all, the increasing flux of the PSF Mem-2 was due to the increase in the membrane hydrophilicity when the PSF membrane was modified by PAA-MNPs composite. Increases in the hydrophilicity helps in improving the membrane flux performance. Moreover, the magnetite nano-composite membrane (PSF Mem-2) contains negatively charge surface PAA-MNPs colloid that helps to produce stern layer on the membrane surface. This stern layer would prevent the deposition of HA particle as HA appeared to have the same negative surface charge. Hence, higher membrane permeability was expected.

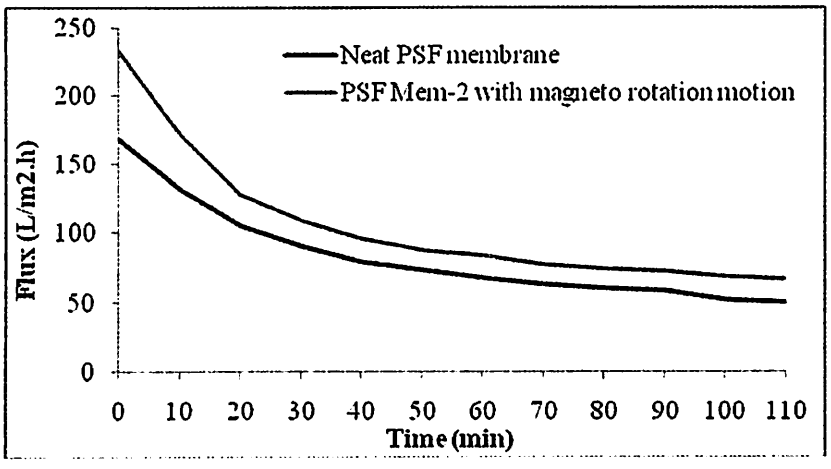

Figure 19: Flux of neat PSF membrane and PSF Mem-2 with magneto rotation motion in HA

As the operating time increases, the fouling was became more severe, thus, more HA were deposited onto membrane surface and reduced the membrane permeability. However, when the magneto rotation motion was introduced to the PSF Mem-2 in at every 30s interval time, the flux was relatively improved (Figure 19). PSF Mem-2 with the introduction of magneto rotation motion had the relatively higher flux compared to neat PSF membrane. Introduction of magneto rotation motion towards PSF Mem-2 induces the MNPs actuation on the membrane surface and further removed the HA foulant deposited on the membrane surface. This phenomenon proved that the magnetite nano-composite membrane with magneto rotation motion could improve the membrane antifouling performance in HA. The membrane selectivity was then observed.

The solute rejection for neat PSF membrane and PSF Mem-2 with magneto rotation motion in HA was observed in Table 5. The HA permeate concentration, Cp was taken after 110min of the filtration process and characterized using UV-visible spectrophotometer at 254nm. The rejection (R%) was calculated according to Equation 4 and compared to the prepared HA standard curve. The initial HA feed concentration was set at 50ppm.

$$\text{Solute rejection, } R(\%) = \left[1 - \frac{C_p}{C_f}\right] \times 100\% \qquad \text{(Eqn. 4)}$$

Table 5: Solute rejection in humic acid

Membrane	Solute rejection, R(%)
Neat PSF membrane	83.33
PSF Mem-2 membrane with magneto rotation motion	86.85

Increases in the solute rejection means increase in the number of HA molecules that were not able pass through the membrane and contributed to the better membrane separation ability. Thus, lower HA concentration would be observed in the permeate solution if the solute rejection was high. Table 5 shows that PSF Mem-2 with the magneto rotation motion showed relatively higher HA solute rejection of 86.85% compared to the neat PSF membrane (83.33%). The greater flux ratio

achieved in Figure 4.24 suggested that magnetite nano-composite membrane was less sensitive to HA deposition, mainly due to its relatively smaller pore sizes on the modified PSF membrane surface after surface coated by PAA-MNPs composite thin film. Smaller membrane pore size preventedHA solutes from entering pore length, minimizing the possibility of pore blockage and/or pore narrowing.

The PAA-MNPs composite layer coated on the membrane surface has also increased the solute rejection by altering the membrane hydrophilicity properties and surface charge. Moreover, the introduction of magneto rotation motion would further increase the membrane antifouling performance due to the MNPs actuation on the membrane surface which allowed the HA deposited/blocked to be removed. Even though, there were slightly higher solute rejection of PSF mem-2 in compared to neat PSF membrane, but the constant and higher flux of PSF Mem-2 was improved throughout the membrane performance. This has shown the high potential of this magnetite nano-composite membrane in improving the membrane antifouling properties.

References:

Chen D.-H. & S.-H. Huang, (2004). Fast separation of bromelain by polyacrylic acid-bound iron oxide magnetic nanoparticles, Process Biochemistry, **39** 2207-2211

Ditsch A., P. E. Laibinis, D. I. C. Wang & T. A. Hatton, (2005). Controlled clustering and enhanced stability of polymer-coated magnetic nanoparticles, Langmuir, **21** 6006-6018

Erban R. & S. J. Chapman, (2007). On Chemisorption of Polymers to Solid Surfaces, Journal of Statistical Physics, **127** 1255-1277

Ghosh S., W. Jiang, J. D. Mcclements & B. Xing, (2011). Colloidal stability of magnetic iron oxide nanoparticles: Influence of natural organic matter and synthetic polyelectrolytes, Langmuir, **27** 8036-8043

Gnanaprakash G., S. Mahadevan, T. Jayakumar, P. Kalyanasundaram, J. Philip & B. Raj, (2007). Effect of initial pH and temperature of iron salt solutions on formation of magnetite nanoparticles, Materials Chemistry and Physics, **103** 168-175

Golas P. L., S. Louie, G. V. Lowry, K. Matyjaszewski & R. D. Tilton, (2010). Comparative study of polymeric stabilizers for magnetite nanoparticles using ATRP, Langmuir, **26** 16890-16900

Hu J.-D., Y. Zevi, X.-M. Kou, J. Xiao, X.-J. Wang & Y. Jin, (2010). Effect of dissolved organic matter on the stability of magnetite nanoparticles under different pH and ionic strength conditions, Science of The Total Environment, **408** 3477-3489

Illés E. & E. Tombácz, (2006). The effect of humic acid adsorption on pH-dependent surface charging and aggregation of magnetite nanoparticles, Journal of Colloid and Interface Science, **295** 115-123

Lu A., E. L. Salabas & F. Schüth, (2007). Magnetic Nanoparticles: Synthesis, Protection, Functionalization, and Application, Angewandte Chemie International Edition, **46** 1222-1244

Madaeni S. S., S. Zinadini & V. Vatanpour, (2011). A new approach to improve antifouling property of PVDF membrane using in situ polymerization of PAA functionalized TiO_2 nanoparticles, Journal of Membrane Science, **380** 155-162

Mak S.-Y. & D.-H. Chen, (2004). Fast adsorption of methylene blue on polyacrylic acid-bound iron oxide magnetic nanoparticles, Dyes and Pigments, **61** 93-98

Martínez-Mera I., M. E. Espinosa-Pesqueira, R. Pérez-Hernández & J. Arenas-Alatorre, (2007). Synthesis of magnetite (Fe_3O_4) nanoparticles without surfactants at room temperature, Materials Letters, **61** 4447-4451

Nguyen V. H. & J.-J. Shim, (2012). Covalently Bonded Poly(Acrylic Acid)-Fe_3O_4 Nanocomposite Prepared in Supercritical CO_2 and Its Adsorption Capacity for Methylene Blue, Synthesis and Reactivity in Inorganic, Metal-Organic, and Nano-Metal Chemistry, **42** 449-454

Yeap S. P., A. L. Ahmad, B. S. Ooi & J. Lim, (2012). Electrosteric stabilization and its role in cooperative magnetophoresis of colloidal magnetic nanoparticles, Langmuir, **28** 14878-14891

OUTPUT

J. Applied Membrane Science & Technology, Vol.15 June, 2012, 15-20

Development of Magnetite Nano-composite Membrane for Membrane Defouling

A. N. Atiah[1], Q. H. Ng[2], A. L. Ahmad[3], S. C. Low[4*]

[1-4]School of Chemical Engineering Campus, Universiti Sains Malaysia, Seri Ampangan, 14300 Nibong Tebal S.P.S. Penang, Malaysia

ABSTRACT

This research proposes to untangle the membrane fouling by introducing nanostructured magnetite (Fe_3O_4) colloids into the polymeric membrane. In present study, nanostructure magnetite nanoparticles (MNPs) were synthesized via co-precipitation method with ammonium hydroxide and sodium hydroxide as the precipitation agents at different pH condition. The synthesized MNPs were functionalized with poly(diallyldimethylammonium chloride) (PDDA) and then spin coated on the surface of the ultrafiltration cellulose acetate (CA) membrane. Intrinsic properties for this nano-composite membrane, in regards to the physical structures, surface negative charge density and the membrane filtration performance, on surface fouling by humic acid solutions were investigated. Experimental results demonstrated that, the nano-composite membrane has significantly reduced the humic acid fouling on the membrane surface. This could be explained by the electrostatic interactions between negatively charged humic acid molecules and the nano-composite membrane. Throughout the study, the results provide some fundamental insights into the physical interactions that governing the membrane fouling during filtration.

Keywords: Fouling; magnetite nanoparticles, humic acids, nano-composite membrane, water treatment

1.0 INTRODUCTION

In recent years, various water treatment technologies are actively being pursued in both academic world and industry due to the rapid deterioration of water quality worldwide. The stringent regulations for drinking water quality have stimulated the membrane filtration to become one of the best alternatives that replacing the conventional drinking water treatment technologies [1-3].

Fouling remains a critical issue in many water filtration processes and serves as the dominant factor that restricts its widespread application [3, 4]. The fouling causes a rapid irreversible loss of flux through the membrane which leads to the progressive deterioration of membrane performance [5].

Periodic hydraulic backwash procedures were usually employed in reducing the effects of fouling. However, the used of hydraulic backwash is practical in removing the reversible foulant. Some deposited matter on the membrane surface and inside the pores cannot be removed and formed the irreversible part of fouling [6].

Recently, the synthesized of nanosized magnetic material have drawn much attention due to their unique properties and potential applications in biomedical [7, 8], heat transfer enhancement and environmental applications [9-11]. Magnetite (Fe_3O_4) nanoparticles are preferred because of its high magnetic susceptibility, non-toxic, low cost instrument and low detection limit [12].

Currently the magnetic actuated membrane is an improvement of the membrane process in removing

* *Corresponding to: S. C. Low* (email: chsclow@eng.usm.my)

the foulant. The nano-composite membrane consist of a highly elastic polymer matrix with embedded nanosized of magnetic particles [13], which is sensitive to the magnetic field. In the presence of a local magnetic field, the magnetic membrane could be stiffened. This will reduced the object and membrane contact area and allowed the object to be either relocated or released.

The aimed of the present study is to untangle the fouling mechanism through magnetically actuated nano-composite membrane. The research efforts were dedicated to formularize a simple experimental protocol for surface functionalization of the polymeric membrane. Through electrostatic interaction between nanostructure magnetite (Fe_3O_4) colloids and membrane, it provided the flexibility on the motion control of magnetite nanoparticles on the membrane surface. Defouling performance of the nano-composite membrane was tested accordingly by using humic acid substances as the foulant.

2.0 RESEARCH METHODOLOGY

2.1 Materials

Iron (III) chloride hexahydrate ($FeCl_3.6H_2O$), iron (II) chloride tetrahydrate ($FeCl_2.4H_2O$), sodium hydroxide (NaOH) and hydrochloric acid fuming 37% (HCL) were purchased from Merck (Darmstadt, Germany). Ammonium hydroxide solution 28% in water (NH_4OH) and poly(diallyl-dimethyl ammonium chloride) (PDDA) were supplied by Sigma-Aldrich (St. Louis, MO). All chemicals used in this study were analytical grade standards and used without further purification.

2.2 Synthesis of Fe_3O_4 Nanoparticles

The magnetite nanoparticles were prepared via co-precipitation method. 4mL of 0.5M $FeCl_3 \cdot 6H_2O$ was mixed with 1mL of 1M $FeCl_2 \cdot 4H_2O$ at 25°C and stirred at stirring speed of 1100rpm. A 25mL of NH_4OH or NaOH (with pH ranging from 9 to 14) that acted as the precipitating agent was immediately added into the mixture and stirred for 30min. Upon the completion of the co-precipitation process, the synthesized magnetite nanoparticles were collected by an NdFeB permanent magnet. Collected magnetite nanoparticles were washed with deionized water (DI) and centrifuged to ensure that pure magnetite was obtained (repeated three times). The magnetites were then sonicated to allow monodisperse of magnetite in DI water.

2.3 Functionalization of Fe_3O_4 Nanoparticles

1000 ppm of magnetite nanoparticles suspension was prepared using DI water and sonicated. Similarly, 0.01667 g/mL of PDDA was prepared and undergo sonication. The pH of both magnetite nanoparticles (MNPs) suspension and PDDA solution was adjusted to pH~8.0 to facilitate physisorption of PDDA on MNPs via electrostatic attraction for 1 day in rotator mixer. The PDDA-coated magnetite nanoparticles were then collected using an Nd-FeB permanent magnet and pre-washed before dispersed in DI water.

2.4 Development of Nano-composite Membrane

The nano-composite membrane was prepared using Flat sheet CA membrane was placed onto the glass plate and fitted onto the vacuum chuck of spin coater. Subsequently, polymer solution containing PDDA-coated magnetite nanoparticles was dispersed onto the membrane surface at rotation speed of 300 rpm and rotation time of 900s until a homogeneous thin film polymer was formed. The nano-composite membrane was then air dried.

2.5 Membrane Performance Test

The performance of the nano-composite membrane toward reducing the nano-composite membranes were test. CA membranes were cut into the dimension of 1×1cm and labeled as sample 1 and sample 2. Both samples were immersed in humic acid (HA) solutions for 13 hours, where the external magnetic field (magnetic bar) was imposed to the sample 1. The introduction of external magnetic field at sample 1 would induce magneto rotation motions of MNPs that bound on the membrane surface and further removed the deposited HA molecules. After 13 hours, the membrane samples were air dried for 24 hours prior analyzed using ATR-FTIR.

2.6 Characterization

2.6.1 Particle Size and Polydispersity Index of Fe_3O_4 Nanoparticles

Average particle size and polydispersity index of magnetite nanoparticles were determined using DLS

(Malvern Instruments Nanosizer ZS). The light scattering intensity autocorrelation function was fitted by the CONTIN algorithm to produce an intensity-weighted distribution of hydrodynamic radii. For DLS measurement, the sample was prepared by dispersed the 0.01 ml of magnetite suspension to 3.5 ml of DI water.

2.6.2 Attenuated Total Reflection Fourier *Transform Infrared (ATR-FTIR)*

The fouling level of the nano-composite membrane was investigated using Thermo Scientific FTIR spectrometer system (NICOLET iS10, USA). The membranes spectra were analyzed using Diamond crystal over wavenumber range of 4000-600 cm^{-1} with 32 scans at 4 cm^{-1} resolutions.

3.0 RESULTS AND DISCUSSION

3.1 Synthesis of Magnetite Nanoparticles

Ammonium hydroxide and sodium hydroxide were selected as the precipitation agents to synthesis the magnetite nanoparticles under different pH condition (from pH 9 to pH 14). It was observed that, different precipitate colour were obtained when co-precipitation process were carried under the different pH conditions. Black precipitate solutions were observed at pH 11 and pH 12 in Fig. 1 and pH 14 in Fig. 2. These solutions were shown to have magnetophoretic responses when imposed to the external magnetic field (magnetic bar). In this regards, the synthesized MNPs were magnetite responsive which is expected able to perform the magneto rotation motions when bound on the membrane surface and further detached the foulants away from the membrane surface.

However, clear yellow solutions were observed throughout the reaction of NH_4OH at pH 9 and pH 10 in Fig. 1 and NaOH from pH 9 and pH 12 in Fig. 2. These yellow colour solutions were the intermediate form of solutions due to the insufficient of precipitation agent. This intermediate forms would change if the precipitation agent continuously added to the process until the OH^- ions sufficient to form MNPs. Knowing that, NaOH solution contained of higher density of OH^- than NH_4OH solution with the same molarities. However the used of strong alkaline media such as NaOH, can caused the formation of non-magnetic

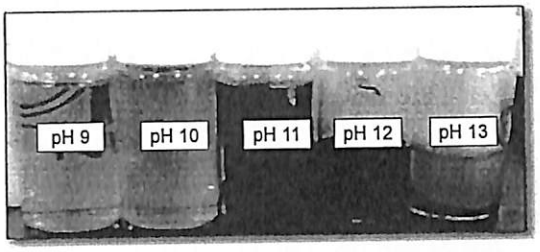

Figure 1 Magnetite nanoparticle prepared at different pH of ammonium hydroxide (NH_4OH)

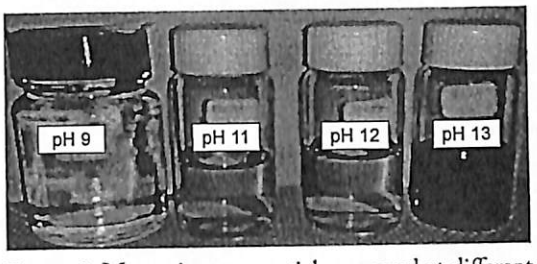

Figure 2 Magnetite nanoparticle prepared at different pH of sodium hydroxide (NaOH)

iron compound [14] such as α-FeOOH and other ion compounds [15].

Fluctuate trends were observed for both hydrodynamic diameter size (Fig. 3) and PDI (Fig. 4) of MNPs when NH_4OH was used as the precipitation agent in co-precipitation process. The interesting finding is that both highest and lowest readings were found at the narrow pH range within pH 11 to pH 12, respectively. MNPs showed to have the average hydrodynamic size of 1046.4 ± 200 nm at pH 11 and only 132.1 ± 0.55 nm at pH 12. PDI was also followed the trend of hydrodynamic size where showed to be 0.798 at pH 11 and monodisperse 0.253 at pH 12. The monodisperse of MNPs at pH 12 might due to electrostatic interaction that leads the repulsion between the negatively charge MNPs. MNPs carry negative surface charge at pH higher than its point zero charge [16, 17].

As for NaOH, MNPs were only able to produce at pH 13 or higher. This might be due to the density of OH^- ions in the NaOH solution at certain pH. It is well known that pH value is responsible for the charge density of OH^- ions, which responsible for the formation of MNPs. NaOH solution at pH below 12 resulted to have low density of ions OH^-, thus, restricted the formation of magnetic responsive nanoparticles and maintained as intermediate form of solutions. However, the interest was focused on pH 14 since the MNPs were magnetite responsive (black color of solution) under this pH condition. At pH 14, the produced MNPs

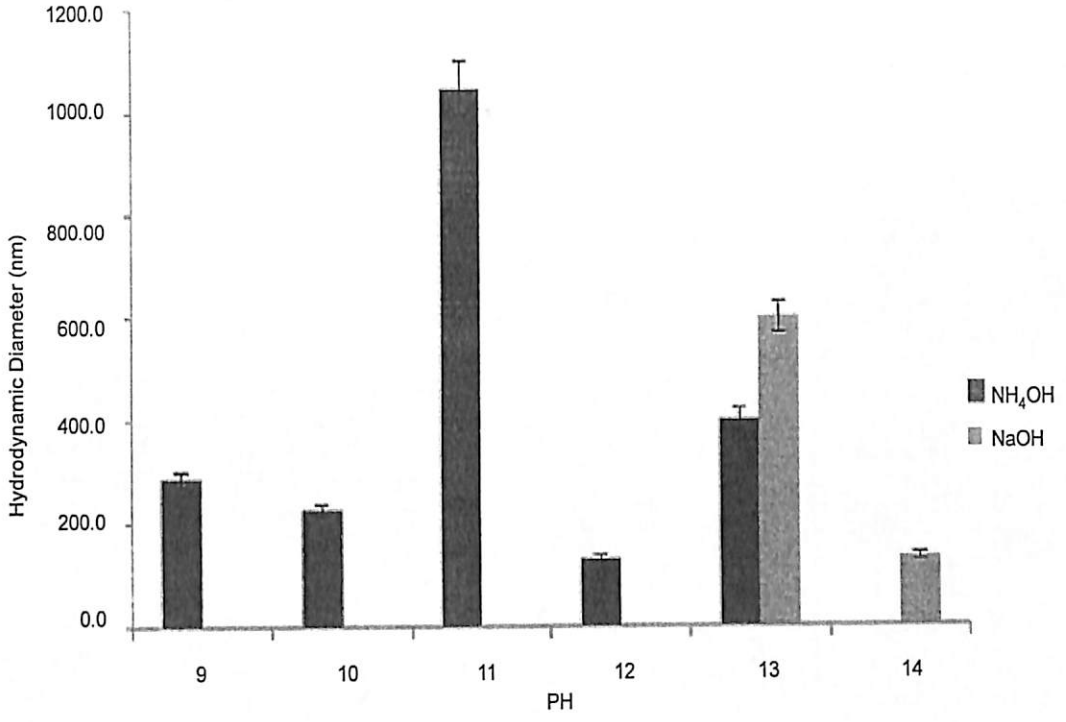

Figure 3 Hydrodynamic diameter of magnetite nanoparticle synthesize at different pH ratio and precipitation agent

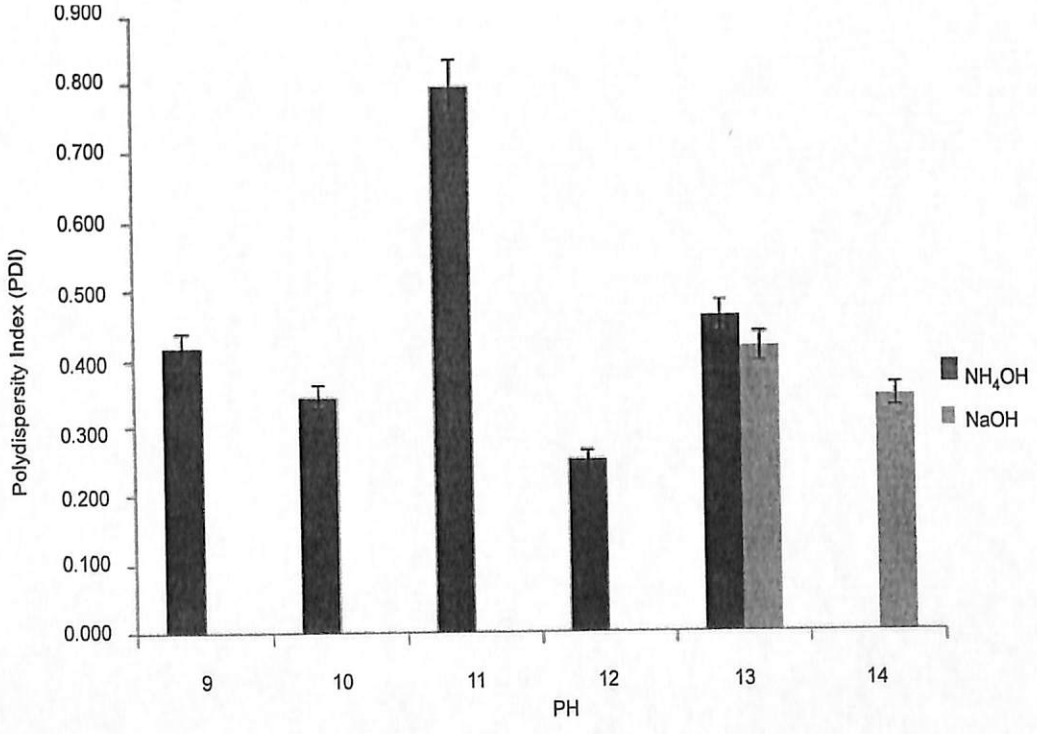

Figure 4 PDI of magnetite nanoparticle synthesize at different pH ratio and precipitation agent

appeared in small hydrodynamic diameters of 134.2 ± 2.27 nm and low PDI of 0.345. Under the consideration of both small hydrodynamic diameter and low PDI, both NH_4OH and NaOH were giving the similar characteristics of produced MNPs. However, NH_4OH was selected as precipitation agent for further study due to the lower pH condition (pH 12) was preferred for membrane filtration process.

3.2 Defouling Performance of Magnetite Nano-composite Membrane

Membrane defouling study was carried out by immersing the membrane sample in HA solution for 13 hours. The fouling level of HA onto membrane surface was analyzed using ATR-FTIR spectrophotocopy, as shown in Fig. 5. Samples 1 (membrane that exposed to the external magnetic field) and sample 2 (membrane that did not exposed to the external magnetic field) showed two significantly different transmission peaks at 1733 and 1636-1581 cm^{-1} wavenumber respectively.

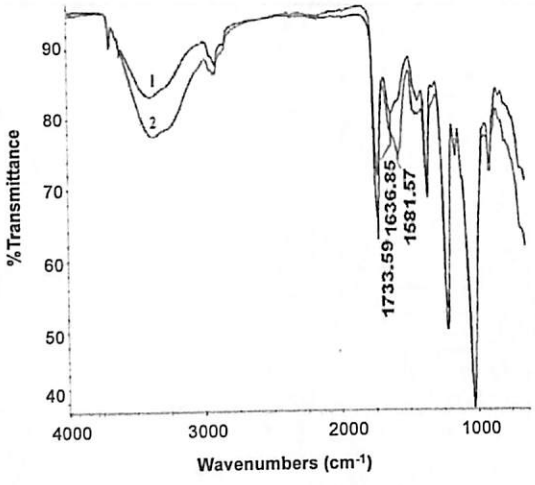

Figure 5 ATR-FTIR spectra for nano-composite membrane (1) with and (2) without the introduction of external magnetic field

The peak at 1733 cm^{-1} could be attribute to the presence of C=O stretching in carboxylic acid groups. The peak at 1636 and 1581 cm^{-1} attribute to the presence of C=C and N-H group respectively. At peak of 1733 cm^{-1}, sample 1 with the exposed to the external magnetic field was found to have a stronger absorption band and vice versa at the overlapping peak of 1581-1636cm^{-1}. Based on these two peaks, it shows that the membrane sample 2 contained higher number of HA molecules that deposited on the membrane surface. These prove that, magnetite nano-composite membrane with the introducing of external magnetic field was could detached the HA precipitation on the membrane surface, thus, reduced the membrane fouling. When the magnetic nano-composite membrane was exposed to the external magnetic field, it will promote the alignment of MNPs that bound onto the membrane surface in one direction. In this regards, the magneto-induced rotation motions within the membrane polymer matrix were performed if two opposite directions were take placed in sequence. The rotational motions of the MNPs, promoted the detachment of the HA from the CA membrane. In turn, HA could easily remove from the MNPs and membrane surface and reduce fouling.

4.0 CONCLUSION

In present study, MNPs with small particle size and polydispersity index were successfully synthesis by using 25 mL of NH_4OH at pH 12 with average hydrodynamic diameters of 132.1 nm and PDI of 0.253. The synthsised MNPs were further stabilized using PDDA and coated onto CA membrane to form magnetic nano-composite membrane. The results demonstrated high efficiency of the removal of humic acid from the membrane surface, in the advantage that the movement of the magnetically responses of MNPs on the membrane surface suppresses fouling.

ACKNOWLEDGMENT

The authors wish to thank the financial support granted by The Institution of Higher Education ERGS grant (6730013) and USM Membrane Science and Technology Cluster.

REFERENCES

[1] Z. Domany, *et al.* 2002. Humic substances removal from drinking water by membrane filtration. *Desalination.* 145 : 333-337.

[2] V. Siyanytsya, *et al.* 2008. Natural organic matter removal from water by complexation-ultrafiltration. *Desalination.* 223 : 91-96.

[3] X. Fu, *et al.* 2008. Effect of surface morphology on membrane fouling by humic acid with the use of cellulose acetate butyrate hollow fiber membranes. *Journal of Membrane Science.* 320 : 483-491.

[4] D. B. Mosqueda-Jimenez, *et al.* 2008. Fouling characteristics of an ultrafiltration membrane used in drinking water treatment. *Desalination.* 230 : 79-91.

[5] K. Katsoufidou, *et al.* 2005. A study of ultrafiltration membrane fouling by humic acids and flux recovery by backwashing: Experiments and modeling. *Journal of Membrane Science.* 266 : 40-50.

[6] G. F. Crozes, *et al.* 1997. "Impact of ultrafiltration operating conditions on membrane irreversible fouling. *Journal of Membrane Science.* 124 : 63-76.

[7] J. Mürbe, *et al.* 2008. Synthesis and physical characterization of magnetite nanoparticles for biomedical applications. *Materials Chemistry and Physics.* 110 : 426-433.

[8] K. Nishio, *et al.* 2007. Preparation of size-controlled magnetite nanoparticles for biomedical applications. *Journal of Magnetism and Magnetic Materials.* 310 : 2408-2410.

[9] X. M. Li, *et al.* 2011. Magnetic Fe 3O 4 nanoparticles: Synthesis and application in water treatment. *Nanoscience and Nanotechnology - Asia.* 1 : 14-24.

[10] W. Yantasee, *et al.* 2007. Removal of heavy metals from aqueous systems with thiol functionalized superparamagnetic nanoparticles. *Environmental Science and Technology.* 41 : 5114-5119.

[11] F. Ge, *et al.* 2012. Effective removal of heavy metal ions Cd 2+, Zn 2+, Pb 2+, Cu 2+ from aqueous solution by polymer-modified magnetic nanoparticles. *Journal of Hazardous Materials.* 211-212 : 366-372.

[12] H. Guo, *et al.* 2010. Application of magnetic nanoparticles for UF membrane integrity monitoring at low-pressure operation. *Journal of Membrane Science.* 350 : 172-179.

[13] C. Schlemmer, *et al.* 2009. The design of thin polymer membranes filled with magnetic particles on a microstructured silicon surface. *NANOTECHNOLOGY.* 9.

[14] G. Gnanaprakash, *et al.* 2007. Effect of initial pH and temperature of iron salt solutions on formation of magnetite nanoparticles. *Materials Chemistry and Physics.* 103 : 168-175.

[15] I. Martínez-Mera, *et al.* 2007 Synthesis of magnetite (Fe3O4) nanoparticles without surfactants at room temperature. *Materials Letters.* 61 : 4447-4451.

[16] J.-D. Hu, *et al.* 2010. Effect of dissolved organic matter on the stability of magnetite nanoparticles under different pH and ionic strength conditions. *Science of The Total Environment.* 408 : 3477-3489.

[17] E. Illés and E. Tombácz. 2006. The effect of humic acid adsorption on pH-dependent surface charging and aggregation of magnetite nanoparticles. *Journal of Colloid and Interface Science.* 295 : 115-123.

Journal of Colloid and Interface Science 421 (2014) 170–177

Contents lists available at ScienceDirect

Journal of Colloid and Interface Science

www.elsevier.com/locate/jcis

Magnetophoresis of iron oxide nanoparticles at low field gradient: The role of shape anisotropy

JitKang Lim [a,b,*], Swee Pin Yeap [a], Chee Hoe Leow [a,1], Pey Yi Toh [a,1], Siew Chun Low [a]

[a] School of Chemical Engineering, Universiti Sains Malaysia, Nibong Tebal 14300, Penang, Malaysia
[b] Department of Physics, Carnegie Mellon University, Pittsburgh, PA 15213, USA

ARTICLE INFO

Article history:
Received 18 November 2013
Accepted 31 January 2014
Available online 7 February 2014

Keywords:
Magnetic nanoparticles
Colloidal stability
Cooperative magnetophoresis
Low gradient magnetic separation
Shape anisotropy

ABSTRACT

Magnetophoresis of iron oxide magnetic nanoparticle (IOMNP) under low magnetic field gradient (<100 T/m) is significantly enhanced by particle shape anisotropy. This unique feature of magnetophoresis is influenced by the particle concentration and applied magnetic field gradient. By comparing the nanosphere and nanorod magnetophoresis at different concentration, we revealed the ability for these two species of particles to achieve the same separation rate by adjusting the field gradient. Under cooperative magnetophoresis, the nanorods would first go through self- and magnetic field induced aggregation followed by the alignment of the particle clusters formed with magnetic field. Time scale associated to these two processes is investigated to understand the kinetic behavior of nanorod separation under low field gradient. Surface functionalization of nanoparticles can be employed as an effective strategy to vary the temporal evolution of these two aggregation processes which subsequently influence the magnetophoretic separation time and rate.

1. Introduction

Iron oxide magnetic nanoparticles (IOMNPs) have been used extensively in processes ranging from biomedical [1–3] to environmental waste and pollutant removal [4–6]. There are several advantages exhibited by IOMNP which make them a unique nano-agent for aforementioned applications, such as high specific surface area [7], catalytically active [8], magnetically responsive [9], optically tunable [10], and can be easily synthesized by a large selection of chemical and physical methods [2,6]. Out from all these features of IOMNP, the ability of this particle to response to an externally applied magnetic field is crucial for its application in separation processes [11,12]. Here, IOMNPs are typically being employed to imparting a paramagnetic dipole moment to the targeted non-magnetic compounds. These IOMNPs tagged compounds become magnetically susceptible and can be separated out from solution through magnetophoretic collection.

Under the influence of a magnetic field, the IOMNPs would migrate toward the region where the field gradient is the highest [13]. This motion of particles relative to their surrounding fluid is known as magnetophoresis. The ability to capture the IOMNPs from suspension media sets the foundation for various magnetic separation technologies and its core working principles under high gradient ($\nabla B > 1000$ T/m) [14] and low gradient ($\nabla B < 100$ T/m) [15] magnetic field have been actively studied. Traditionally, the removal of magnetic nanoparticles (plus all the magnetically tagged compounds) in solution is carried out through high gradient magnetic separation (HGMS). This HGMS technology has been successfully employed for various applications and is capable to capture particles with sizes from microns to tens of nanometers [16]. However, two major drawbacks of HGMS are (1) high initial investment cost to setup automated separator [17], and (2) inhomogeneous magnetic field associated to the operational of HGMS make it difficult to develop numerical and/or analytical solutions to aid the design of a separation process used for specific applications [18].

On the other hand, low gradient magnetic separation (LGMS) does not involve the use of loading matrix. A nice review article on this topic is recently published by Faraudo and coworkers with detail descriptions on fundamental physics involved [19]. In short, under LGMS the separation of magnetic nanoparticles is first driven by aggregation of particles by an externally applied magnetic field, and later the particle clusters formed can be easily collected through cooperative magnetophoresis [15,20,21]. Since LGMS of IOMNPs is relying on the formation of particle clusters, hence, this

* Corresponding author at: School of Chemical Engineering, Engineering Campus, Universiti Sains Malaysia, Seri Ampangan, 14300 Nibong Tebal, Penang, Malaysia. Fax: +60 4 594 1013.
E-mail address: chjitkangl@eng.usm.my (J. Lim).
[1] These authors contributed equally.

http://dx.doi.org/10.1016/j.jcis.2014.01.044
0021-9797/

process is highly concentration dependent [20]. It is anticipated that the increment of particles concentration will lead to higher collision frequency between the particles, and eventually, higher change for the formation of particle clusters. Furthermore, the chaining of particles due to magnetic dipole–dipole and hydrodynamic interactions also play a significant role in LGMS as enhancement factors to accelerate the collection of IOMNPs [21]. Besides, our group has recently demonstrated the important of surface modification in dictating the magnetophoretic separation rate [22]. From our experimental results, the more colloidal stable the IOMNP is, the harder it is to be magnetophoretically collected. This observation can also be generalized to HGMS process [23].

In previous research on magnetic separation of IOMNPs, by using either HGMS or LGMS, almost all the efforts were dedicated to the understanding of magnetophoretic behavior of spherical particles. Even though rod-like magnetic nanoparticles have been used for various interesting applications [24,25], there are very limited works have been done on the magnetophoresis of nanorod that exhibit magneto-shape anisotropy [26]. Despite its interesting and added benefits in rapid magnetic separation [12], numbers of uncertainties and issues remain unexplored related to the use of magnetic nanorod for separation process. In addition, it is also equally unclear about the contributing factors that would influence the performance of magnetic nanorod in magnetophoretic separation. It is our interest in this paper to show the comparison of cooperative magnetophoresis for spherical and rod-like IOMNPs under low gradient magnetic separation. By monitoring the migration of iron oxide nanorod with respect to an externally applied magnetic field in two and three dimensional space, we investigate the underlying mechanisms and time scale involved within each stage of nanorod magnetophoresis. In addition, we also evaluate the effects of particle concentration and magnetic field gradient on the separation kinetics of nanorod. All these studies are important to establish design rule for LGMS by using rod-like particles as a magnetic tagging agent.

2. Experimental section

2.1. Materials

Iron oxide nanosphere, Fe_3O_4 (APS, 98 + % purity) (Fig. 1a), was purchased from Nanostructured & Amorphous Materials, Inc. Iron oxide nanorods (Fig. 1b) employed in this work were generously supply by TODA American, Inc. (refer to Fig. SI of supporting information for size distribution of these particles). The saturation magnetization M_s for these two species of IOMNPs was measured previously with value at ~90 emu/g and 74.61 emu/g for nanorod and nanosphere, respectively [12]. Water soluble cationic polyelectrolyte poly(diallyldimethylamonium chloride) (PDDA) with average molecular weight ~100,000–200,000 Da (20 wt.% in H_2O) was supplied by Sigma–Aldrich. Sodium chloride, NaCl used in zeta potential measurement was purchased from Merck Sdn.Bhd. Cylindrical shaped N50-graded Neodymium Boron Ferrite (NdBFe) and Aluminium Nickel Cobalt (Alnico) permanent magnet with 14 mm in diameter and 15 mm in length were purchased from Ningbo YuXiang E&M Int'l Co., Ltd. The remanence B_r for these two magnets is 1.20 Tesla and 1.45 Tesla for Alnico and NdFeB, respectively. All the chemicals were used as received without further modification or purification.

2.2. Preparation of PDDA-coated IOMNPs

Suspension of IOMNPs at 1000 mg/L in deionized water was prepared by ultrasonication to disperse the black powder obtained commercially. At the same time, PDDA solution with concentration at ~0.005 g/mL was prepared by addition of 1.25 mL of as accepted PDDA solution into 48.75 mL of deionized water. This mixture was immediately subjected to intermittent ultrasonication for at least 30 min to promote their dissolution and left overnight on an end-to-end rotator with mixing rate of 40 rpm. This concentration of PDDA is chosen to ensure the available PDDA molecules are at least 500 times more than the estimated amount needed to form monolayer on the particles surface [23]. Before mixing, the IOMNPs solution was subjected to intense sonication for 2 min. Drop wise addition of IOMNPs suspension into PDDA solution was carried under intense sonicafication within a sonicator bath. Successful attachment of PDDA onto IOMNPs was verified by monitoring the electrophoretic mobility changes before and after the PDDA adsorption with Malvern Instruments Nanosizer ZS. By using the same analytical equipment, the particles size distribution before and after the PDDA attachment was measured through dynamic light scattering method (see Fig. SI in supporting information).

2.3. Monitoring magnetophoresis of IOMNPs

A custom built optical sensing system was employed to obtain the kinetic profile of IOMNPs under magnetophoresis [22]. Depends on the extent of light transmitted through the IOMNP suspension, by using a light dependent resistor (LDR), we monitored the voltage changes associate to the changes in intensity of detected light from a light-emitting diode (LED). The wavelength of the LED employed is at around 620 nm and the suspension

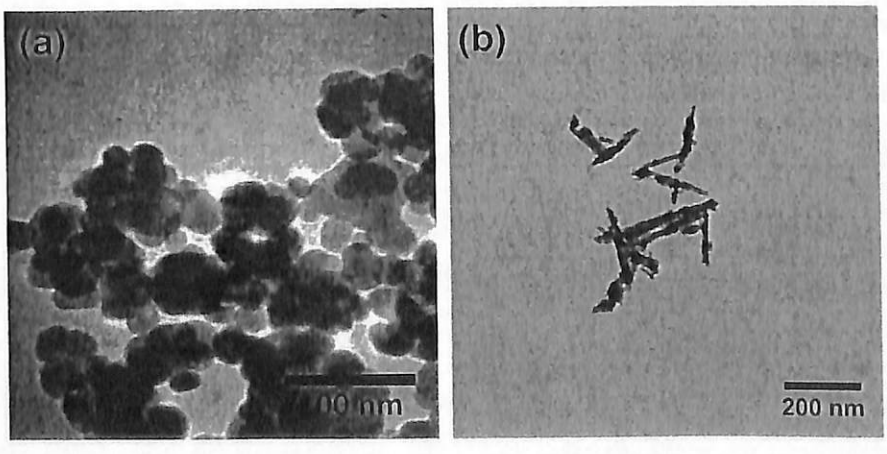

Fig. 1. Transmission electron micrographs of iron oxide (a) nanosphere and (b) nanorod used in this work.

was confined within a standard rectangular 3.5 mL cuvette. These measurements can then be translated into normalized opacity $\theta(t)$ at time t by following equation [15]:

$$\theta(t) = \frac{V(t) - V_{\min}}{V(0)}, \tag{1}$$

where $V(0)$ is the initial voltage readout at time zero, $V_{\min}$ is the lowest voltage registered and $V(t)$ is the voltage output at time t. At $\theta(t)$ equal to one, the transmitted light is fully blocked correspond to the full dispersion of the particles. Whereas, at $\theta(t)$ equal to zero indicates full transmission of light due to the complete magnetophoretic collection of the IOMNPs.

For optical microscopy monitoring is concerned, we used Olympus BX53 microscope to record the magnetophoresis of IOMNPs. CellSens Dimension imaging software was employed to capture the brightfield images and the magnetophoretic pathway of particles was analyzed by using ImageJ software. In all microscopy observation, NdFeB magnet was used to introduce magnetic field into our system and was positioned at the upper left hand side of the images (front left corner of the microscope) with separation distance of less than 1 cm.

3. Results and discussions

3.1. Magnetophoresis of nanorod and nanosphere

Magnetophoresis of spherical (magnetic core diameter ~50 nm) and rod-like IOMNPs (20 × 300 nm) induced by a cylindrical NdFeB permanent magnet showed remarkably different kinetic behaviors (Fig. 2). In general, nanorod takes significantly less time than nanosphere to be fully separated. This nanorod suspension turned crystal clear at around 90 s after exposure to a permanent magnet. Whereas, the light brown color of a nanosphere suspension can still be observed after 180 s subjected to magnetophoretic separation. The experimental evidence that nanorods could be magnetophoretically collected much rapidly than nanosphere is generally true for both species of particle with or without surface coating. This scenario is mainly due to the fact that the magnetophoresis is favored in anisometric particles [27]. For low Reynolds number ($Re \ll 1$) magnetophoresis in a Newtonian fluid, by taking into consideration of drag force, magnetophoretic force and shape factor, the rod geometry gives almost 200 times higher magnetophoretic velocity compared to spherical structure with equivalent volume [28]. In addition, the induced magnetic dipole

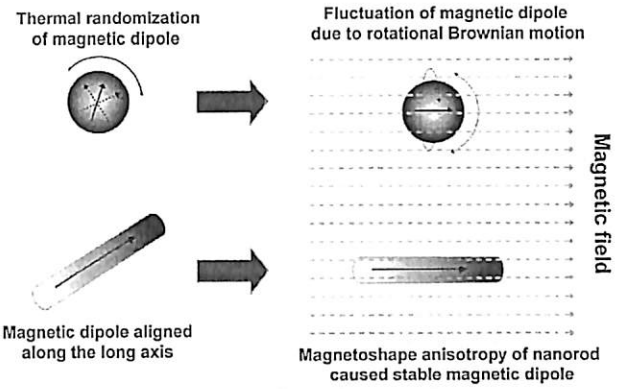

Fig. 3. Alignment of magnetic dipole parallels to the external applied magnetic field. For the case of spherical IOMNP, thermal randomization not only disrupts the magnetophoretic pathway of the particles but also disorients its magnetic dipole orientation within the magnetic field.

aligned along the long axis of nanorod (see Fig. 3) is more stable [29], and hence, less susceptible to the thermal disruption [26,30].

For a spherical IOMNP, its steady state magnetophoretic velocity can be calculated as

$$u_{mag} = \frac{F_{mag}}{6\pi\eta R} \tag{2}$$

where η is the viscosity of the suspension and R is the radius of the IOMNP. F_{mag} is the magnetophoretic force experienced by the IOMNP and can be defined as

$$F_{mag} = (MV_{mag} \cdot \nabla)B \tag{3}$$

where M is the field dependent magnetization, V_{mag} is the magnetic particle volume, and B is the magnetic induction. By taking a 30 nm nanosphere exposed to magnetic field gradient ($\nabla B = 100$ T/m) from a NdFeB magnet like the one showed in Fig. 2, with the assumption of its reached saturation magnetization, the calculated magnetophoretic velocity u_{mag} for none interacting particle is at around 3.26 μm/s [30]. Even by overestimating the field gradient involved, this calculated velocity is still too low to achieve separation kinetic as observed in Fig. 2. With a total travelling distance of 25.4 mm (the diameter of the glass vial in Fig. 2), it will take approximately 130 min for the non-interacting particle on the other side of the vial to be magnetophoretically collected. So in most

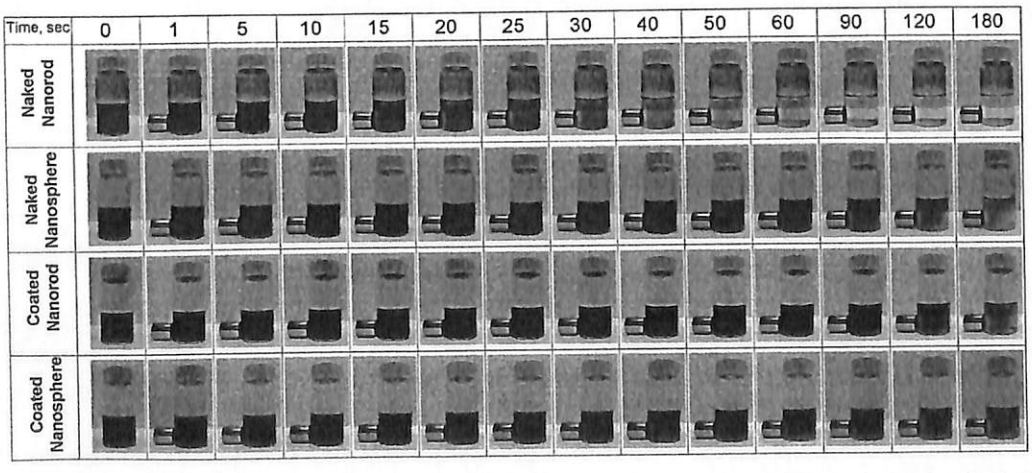

Fig. 2. Temporal evolution of suspension opacity for spherical and rod-like IOMNPs before and after surface functionalization by PDDA under the influence of a NdFeB cylindrical magnet. All particle concentration is at 50 mg/L.

likelihood, the IOMNPs have to undergo certain level of interactions, forming large magnetic clusters and migrate cooperatively towards the permanent magnet [15,21]. This hypothesis can be further confirmed with the magnetophoresis experiment as depicted in Fig. 2. According to the magnetophoresis experiments shown in Fig. 2, the major difference between surface modified and none surface modified particles is in the previous case the magnetophoretic collection time increased quite drastically for both nanorod and nanosphere. At the end of the experiment, the coloring of suspension remained for surface functionalized particles whilst naked IOMNP suspension, both nanorod and nanosphere, turned almost colorless. The adsorbed PDDA layer used to promote colloidal stability has also mitigated the attractive interaction between the IOMNPs, and hence, suppressed aggregation of the particles which is the pre-requirement for rapid cooperative magnetophoresis [22,23]. This unique feature of magnetophoresis, where the kinetic of the particle's motion under low field gradient is dependent on the surface functionalization, is crucial from engineering perspective. It allows the fine tuning of magnetophoretic separation time by changing the surface coating of the magnetic nanoparticles with same size, shape and composition.

3.2. Kinetic behavior of cooperative magnetophoresis

In order to have a more quantitative and better understanding on the cooperative behavior of IOMNP magnetophoresis under low field gradient, we monitored the opacity changes of the particle suspension (Fig. 4) over the time course of 500 s after its exposure to a NdFeB. Here we assumed that light transmitted through the suspension can be directly related to the remained particles concentration after magnetophoresis by protocol developed by Schaller and coworkers [21]. This assumption might not be necessary true as spatial distribution of the magnetic field strength causes variation in the magnetophoretic velocity of IOMNPs, and hence, non-uniform blocking of light. Nevertheless, the magnetophoretic collection rate can be crudely estimated by linear fit to the first half of the graph where rapid decay of opacity occurred [31].

By referring to Fig. 4a and b, both the magnetophoretic collection rate and time are dependent on the suspension concentration. As the initial concentration of the IOMNPs increased, for both nanorod and nanosphere, the collection time has been shorten with the increment of collection rate. This observation is in accordance to the cooperative magnetophoresis model discussed earlier [15,18]. At concentration below 100 mg/L, the overall decay rate of suspension opacity for nanorod is steeper than nanosphere at same particle concentration indicating that the rapid magnetophoresis of rod-like particle. With the increment of particle concentration from 25 mg/L to 100 mg/L, the collection rate has also been increased from 0.0030 a.u./s to 0.0124 a.u./s for nanosphere and 0.0043 a.u./s to 0.0122 a.u./s for nanorod. At this stage, the influence of magneto-shape anisotropy on the magnetophoretic collection rate becomes irrelevant as the particle concentration increased. Transition of magnetophoretic curve from two independent lines as shown in Fig. 4c collapsed onto a single curve in Fig. 4d implied that not only the collection rate has become particle-shape independent at 100 mg/L but also the separation time. Coincidentally, the magnetophoresis becomes size independent

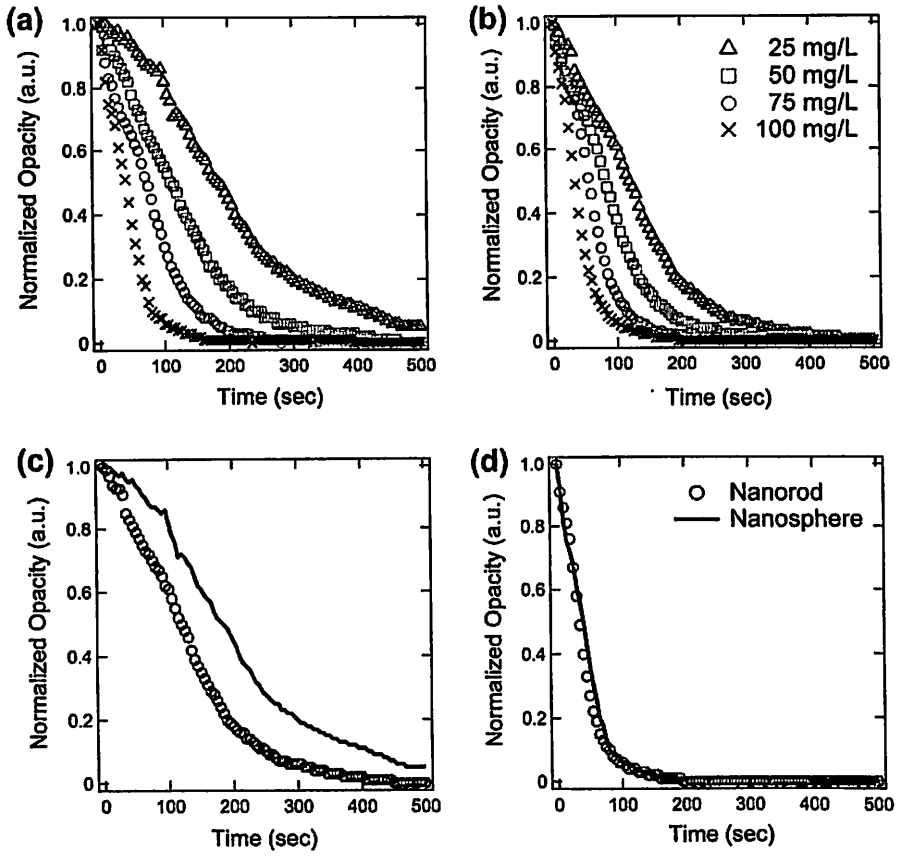

Fig. 4. Concentration dependency of PDDA coated (a) nanosphere and (b) nanorod under low magnetic field gradient magnetophoresis and comparison of magnetophoretic collection of nanorod and nanosphere suspension at (c) 25 mg/L and (d) 100 mg/L. Noted that figures (c) and (d) are redrawn from the same data sets as presented in (a) and (b).

as the particle concentration go beyond 100 mg/L [21], even though the F_{mag} is proportional to the volume of the particles. Since the collision frequency between the single particles depends directly on the particle concentration [32], as concentration increased there is a better chance for aggregation to occur which leading to rapid magnetophoresis. Thus from these results we can concluded that at high concentration the particle's shape will influence the magnetophoresis of an individual particle but not the cooperative magnetophoresis of a particle cluster.

Since the magnetophoretic force is influenced by both the magnetic field strength and gradient (see Eq. (3)), we repeated the magnetophoresis measurement of both PDDA decorated nanosphere and nanorod at the concentration of 50 mg/L to evaluate the influence of these parameters on the separation kinetic (Fig. 5). This working concentration was chosen to ensure higher probability for the distinctive contribution of magneto-shape anisotropy be detected for the ease of comparison. By replacing NdFeB cylindrical magnet with Alnico magnet of same dimension with much lower field gradient at (and also field strength as shown in Fig. 5a), one of the most obvious consequences is the prolonged collection time for both nanorod and nanosphere. By taking linear interpolation on the portion of the magnetophoresis curve that undergo rapid decay (Fig. 5b), we found out that the collection rate of nanorod under the influence of Alnico magnet at 0.0041 a.u./s is approaching the collection rate of nanosphere at 0.0045 a.u./s by NdFeB magnet. For any engineering related application, this unique feature of LGMS allows the optimization of particle shape and/or profile of magnetic field (both strength and gradient) selectively in order to achieve comparable collection rate. This has otherwise provides extra degree of freedom for the design of separation process driven by low magnetic field gradient. It should be noted that our observation in Fig. 5 have directly proven the complex influence of magnetic field gradient in cooperative magnetophoresis which is still an pending issue for further research.

It should also be noted that the initial time lag as observed in Alnico magnet induced magnetophoresis is mainly due to its weak magnetic field strength to cause particles aggregation. In addition, the enhanced colloidal stability introduced by adsorbed layer of PDDA might also play an important role to further aggravate the problem of slow collection time [22].

3.3. Nanorod magnetophoresis in microscopic scale

For cooperative magnetophoretic motion of nanorod, the migration process involved three phases, namely aggregation, alignment and movement. Typical rod-like nanoparticles would spontaneously assemble into small isotropic structure in order to minimize their surface energy [33]. For magnetic nanorods, the extensive aggregation is most likely caused by the magnetic dipole–dipole and van der Waals interactions [34,35]. Even though the nanorod has been electrosterically stabilized by PDDA through physisorption, the formation of submicron particle clusters is almost inevitable [23,36]. In addition to this high tendency for self-aggregation which leading to the formation of large particle cluster, magnetic alignment of nanorod under the influences of an externally applied magnetic field [37], as depicted in Fig. 3, contributes to the rapid magnetophoretic behavior of rod-like IOMNPs. The stable alignment of nanorod with respect to the magnetic field lines due to its magneto-shape anisotropy making the particles less susceptible to the thermal randomization displacement during magnetophoresis [30].

Besides self aggregation, a colloidally stable suspension composed of iron oxide nanocluster will also undergo aggressive magnetically induced aggregation within few seconds after exposed to magnetic field [22]. This process is almost instantaneous and for magnetic nanoparticles with 100 nm in radius and magnetic Bjerrum length of 2 μm the time taken is ~0.06 s [38]. Here, the Bjerrum length is defined as the distance between particles with parallel dipoles at which the attractive magnetic energy that favor aggregation is equal to the thermal energy. Nevertheless, it should also be noted that for well dispersed individual IOMNPs (not clusters), this aggregation phase under magnetic field gradient of 60 T/m can be further prolonged to 300 s by using citric acid treated spherical superparamagnetic nanoparticles [20].

During the alignment phase, inertial forces play a minor role in nanorod dynamics [39]. Governing equation describing the nanorod rotation can then be obtained by balancing the magnetic torque with the viscous torque, and hence, leading to the relevant drag coefficient γ around the short axes of the rod [40]:

$$\gamma = \frac{\eta\pi}{3}\frac{l^3}{\ln(P) + C_r} \tag{4}$$

$$C_r = -0.662 + \frac{0.917}{P} - \frac{0.05}{P^2} \tag{5}$$

where l is the nanorod length and P is the length to diameter ratio of the nanorod. At such the time t for rotation of a nanorod toward its equilibrium orientation is only depends on the its initial

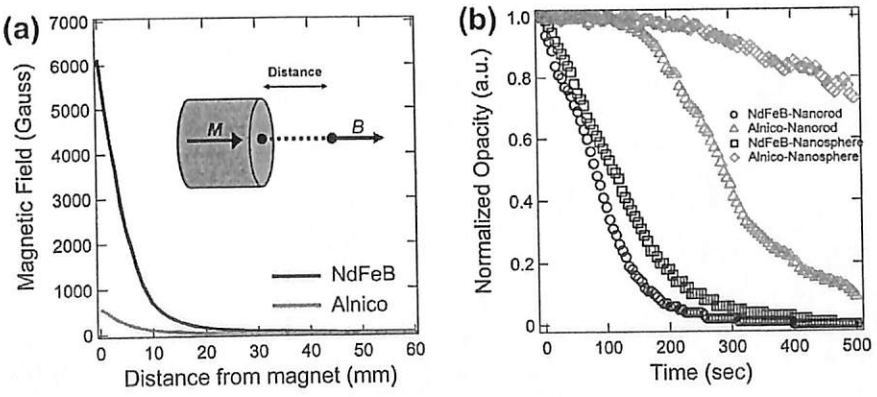

Fig. 5. (a) Magnetic field strength extended out perpendicularly from the surface of a cylindrical magnet (data for NdFeB magnet is extracted from the supporting document of ref 12. By linearized the slope of the graph within first 10 mm from the magnet (equivalent to our working range for magnetophoretic measurement by using a standard cuvette) gives the field gradient ∇B at 53.65 Tesla/m and 4.86 Tesla/m for NdFeB and Alnico magnet, respectively. These approximated values for ∇B have also indirectly proven that all our experiments were carried out under LGMS condition. (b) Magnetophoresis curves of PDDA coated iron oxide nanosphere and nanorod with respect to magnetic field from NdFeB and Alnico permanent magnet. All the IOMNP concentration is at 50 mg/L.

orientation and is directly proportional to β ($t \propto 1/\beta$), which is defined as [37]:

$$\beta = \frac{mB}{\gamma} \tag{6}$$

where m is the magnetic moment of the nanorod. By consider the nanorod has a magnetization very close to saturation throughout the entire duration of magnetophoresis process, which is not necessary true but this estimation serves as the upper bound of our analysis, the magnetic moment can therefore be estimated as $m \approx M_s V_{pt} \rho_{pt}$ [38]. Here M_s is the saturation magnetization per unit mass of the particle (know through magnetometry measurement at 90 emu/g), V_{pt} and ρ_{pt} is the volume and density of the particle, respectively.

The magnetic alignment time needed for a Ni nanorod with 5 μm in length and less than 200 nm in diameter ($\beta = 12.1\ s^{-1}$) is around 0.7 s [37]. For the iron oxide nanorod employed in this work, with dimension at around 300 nm × 20 nm (see Fig. 1) [26], the estimated β by using Eq. (5) is approximately $1.98 \times 10^6\ s^{-1}$. Since the alignment time is linearly dependent on $1/\beta$, so by having β which is almost five orders of magnitude larger than the aforementioned Ni nanorod would lead to drastic reduction in alignment time. However, as illustrated in Fig. 6, it takes roughly 0.75 s for the iron oxide nanorods to achieve full alignment. At such, it is very likely that the alignment of nanorod as observed in Fig. 6 is also a cooperative phenomenon in which the collective rotation of the entire clusters with respect to the magnetic field has been heavily suppressed. Besides the large nanoclusters size in micrometer range (larger drag coefficient than individual nanorod) and hydrodynamic interactions [41], interparticle interactions should also play an important role in determining the associated time scale for the transition of randomly oriented nanorod clusters (Fig. 6a) to partially aligned clusters (Fig. 6b and c), and subsequently leading to fully aligned clusters (Fig. 6d).

Continuous exposure of a fully aligned nanorod cluster to an external magnetic field would lead to its magnetophoresis (Fig. 7). By inspecting magnetophoretic pathway of ten nanorod clusters, it was found that the averaged magnetophoretic velocity is at around 16 μm/s (Table 1). Within the viewable area of our microscopy study, all the clusters investigated are travelling at terminal velocity with no sign of acceleration. It is very likely that the observed clusters have not travelled into the 'capture' zone where the field gradient is the steepest [30]. Even though this measured 2D magnetophoretic velocity is one order of magnitude higher than the calculated nanosphere velocity based upon non-interacting particle assumption discussed earlier, but, it is still insufficient to explain the rapid magnetophoretic collection as demonstrated in Fig. 2. Within our experimental condition, the nanorod suspension is sandwiched within a thin layer of fluid, with thickness at around 136 μm by using adhesive tape as spacer, between a microscope slide and cover slip. Clearly, this confined movement of nanorod clusters (in Fig. 7) is affected by the friction forces, such as viscous drag or friction with the slide surface [42]. More notably, some of the clusters are non-mobile while others migrated toward the magnetic field source suggesting their adhesion to the slide surface. Besides, fattening of the clusters was witnessed if the magnetophoresis experiments were carried in prolonged period >1 min (see Fig. SII in supporting information). Here, two possible results

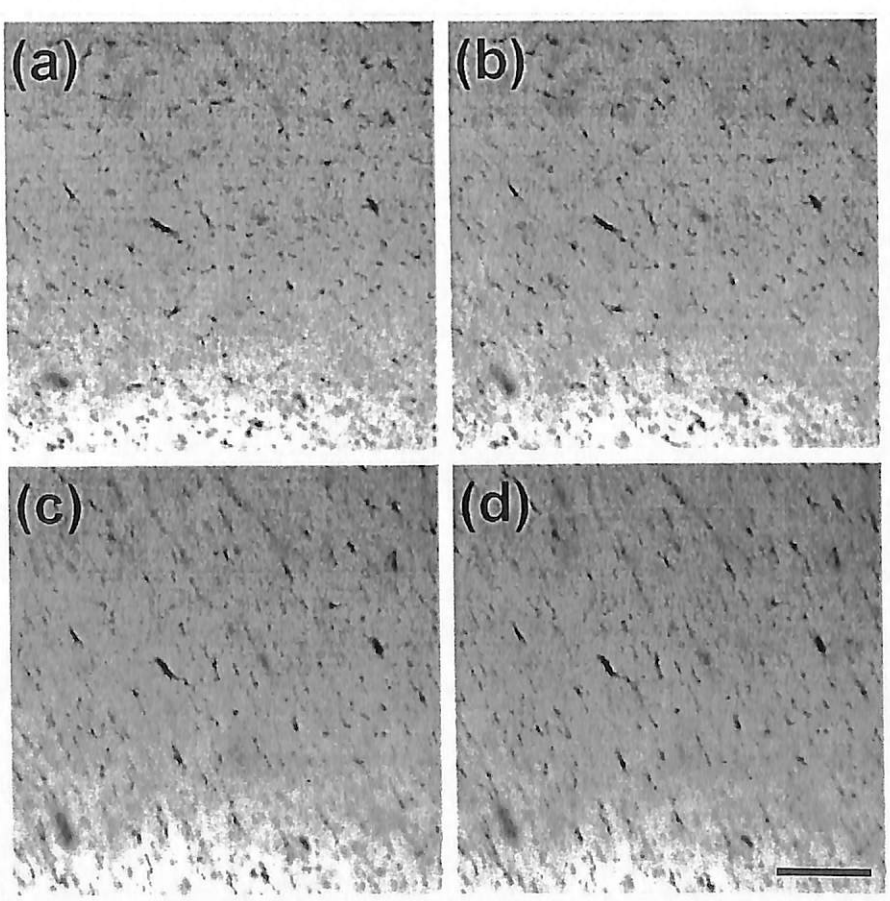

Fig. 6. Transient behavior of nanorod clusters undergoing magnetic alignment from (a) random orientation to (b and c) partial alignment and finally (d) full alignment. The scale bar is 100 μm and time interval between each image is 0.25 s.

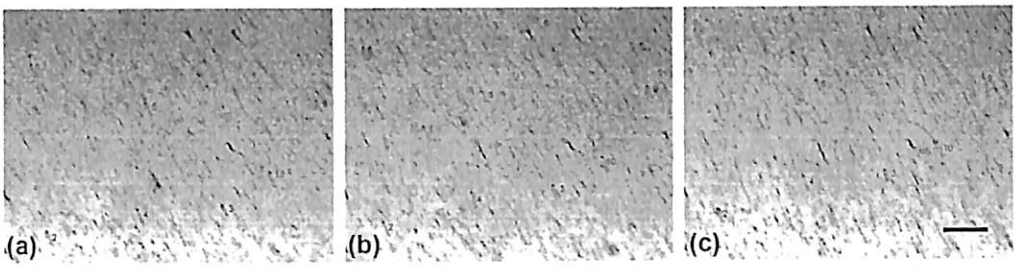

Fig. 7. Time lapse images showing rapid magnetophoresis of nanorod clusters after their alignment with an externally applied magnetic field. All ten groups of nanoclusters are moving toward the left hand corner of the micrograph where the magnet is located and the magnetic field gradient is the steepest. The scale bar is 100 μm and time interval between each image is 2 s.

Table 1
Summarized magnetophoresis results for ten groups of nanorod cluster shown in Fig. 7.

Cluster label	Cluster length (μm)	Travelling distance (μm)	Average velocity (μm/s)
1	27.74	57.36	14.34
2	35.23	52.02	13.01
3	28.95	83.99	21.00
4	45.31	79.09	19.77
5	27.01	53.78	13.45
6	35.70	80.52	20.13
7	34.54	57.81	14.45
8	29.52	38.73	9.68
9	28.89	67.98	17.00
10	43.89	70.18	17.55

of aggregation could still happened as the clusters collided to each other: (1) the formation of longer cluster chain due to tip-to-tip aggregation, or (2) the formation of thicker cluster chain due to lateral aggregation [38]. Our results in which the thicker aggregates is favored over longer chain in collision during magnetophoresis is consistent with their observation and might be the reason for the speedy magnetophoretic collection of nanorods as observed in Fig. 2.

4. Conclusions

We have clearly shown that at low particle concentration the contribution of shape anisotropy is crucial in speeding up the collection rate and shortening the collection time of IOMNPs at low field gradient magnetophoresis. This dependency, however, is highly related to particle concentration. At high particle concentration of 100 mg/L, both the magnetophoretic collection rate and time achieved by nanosphere and nanorod are comparable. In addition, it is possible for nanosphere to match the magnetophoretic collection rate of nanorod, even at low particle concentration of 50 mg/L, by changing the magnetic field gradient. Simultaneous tuning of particle shape and field gradient provides new option for the design of separation strategy which is workable at low field gradient. Combined with the cooperative magneophoresis data in macroscale, our optical microscopy experiments suggested that the entire cooperative magnetophoretic process of nanorod involved three phases, namely aggregation, alignment and movement. The first two phases typically happened in less than a second unless a very weak magnetic field source is used, such as Alnico magnet. These two processes are very likely driven by the cooperative nature of particle interactions. For rapid magnetophoresis is concerned, the measured 2D magnetophoretic velocity at ~16 μm/s is still an underestimated value mainly due to frictional forces arise from the confined motion of the IOMNPs. We anticipated that further collision between the nanorod clusters during the cooperative magnetophoresis process, which leading to the formation of larger aggregate, is the key factor that contributes to their rapid separation.

Author contributions

The manuscript was written through contributions of all authors. All authors have given approval to the final version of the manuscript.

Acknowledgments

This material is based on the work supported by Research University Grant (RUI) (Grant No. 1001/PJKIMIA/811219) from Universiti Sains Malaysia (USM), Exploratory Research Grants Scheme (ERGS) (Grant No. 203/PJKIMIA/6730013) from the Ministry of Higher Education of Malaysia, and eScience Fund (Grant No. 205/PJKIMIA/6013412) from MOSTI Malaysia. All authors are affiliated to the Membrane Science and Technology Cluster of USM.

Appendix A. Supplementary material

Supplementary data associated with this article can be found, in the online version, at http://dx.doi.org/10.1016/J.JCIS.2014.01.044.

References

[1] A.K. Gupta, M. Gupta, Biomaterials 25 (2005) 3995–4021.
[2] J. Gao, H. Gu, B. Xu, Acc. Chem. Res. 42 (2009) 1097–1107.
[3] N.L. Adolphi, D.L. Huber, H.C. Bryant, T.C. Monson, D.L. Fegan, J.K. Lim, J.E. Trujillo, T.E. Tessier, D.M. Lovato, K.S. Butler, P.P. Provencio, H.J. Hathaway, S.A. Majetich, R.S. Larson, E.R. Flynn, Phys. Med. Biol. 55 (2010) 5985–6003.
[4] J. Hu, I.M.C. Lo, G. Chen, Sep. Purif. Technol. 56 (2007) 249–256.
[5] P. Xu, G.M. Zeng, D.L. Huang, C.L. Feng, S. Hu, M.H. Zhao, C. Lai, Z. Wei, C. Huang, G.X. Xie, Z.F. Liu, Sci. Total Environ. 242 (2012) 1–10.
[6] J.S. Hu, L.S. Zhong, W.G. Song, L.J. Wan, Adv. Mater. 20 (2008) 2977–2982.
[7] M. Uota, H. Arakawa, N. Kitamura, T. Yoshimura, J. Tanaka, T. Kijima, Langmuir 21 (2005) 4724–4728.
[8] M. Hermanek, R. Zboril, I. Medrik, J. Pechousek, C. Gregor, J. Am. Chem. Soc. 129 (2007) 10929–10936.
[9] K. Woo, J. Hong, S. Choi, H.W. Lee, J.P. Ahn, C.S. Kim, S.W. Lee, Chem. Mater. 16 (2004) 2814–2818.
[10] V. Mahendran, J. Philip, Langmuir 29 (2013) 4252–4258.
[11] M. Zborowski, G.R. Ostera, L.R. Moore, S. Milliron, J.J. Chalmers, A.N. Schechtery, Biophys. J. 84 (2003) 2264–2638.
[12] J.K. Lim, C.J.C. Derek, S.A. Jalak, P.Y. Toh, N.H. Mat Yasin, B.W. Ng, A.L. Ahmad, Small 8 (2012) 1683–1692.
[13] M. Zborowski, J.J. Chalmers, Magnetic Cell Separation, vol. 32, Elsevier, Oxford, UK, 2008.
[14] G.D. Moeser, K.A. Roach, W.H. Green, T.A. Hatton, P.E. Laibinis, AIChE J. 50 (2004) 2835–2848.
[15] L.G. Cuevas, J. Faraudo, J. Camacho, J. Phys. Chem. C 112 (2008) 945–950.
[16] J. Svoboda, Magnetic Techniques for the Treatment of Material, Kluwer Academic, Dordecht, 2004.
[17] P.Y. Toh, S.P. Yeap, L.P. Kong, B.W. Ng, D.J.C. Chan, A.L. Ahmad, J.K. Lim, Chem. Eng. J. 211–212 (2012) 22–30.
[18] J.S. Andreu, J. Camacho, J. Faraudo, M. Benelmekki, C. Rebollo, Phys. Rev. E 84 (2011) 021402.

[19] J. Faraudo, J.S. Andreu, J. Camacho, Theory Simul. Soft Matter. 9 (2013) 6654–6664.
[20] M. Benelmekki, C. Caparros, A. Montras, R. Gonçalves, S. Lanceros-Mendez, L.M. Martinez, J. Nanopart. Res. 13 (2011) 3199–3206.
[21] V. Schaller, U. Kräling, C. Rusu, K. Petersson, J. Wipenmyr, A. Kozer, G. Wahnström, A. Sanz-Velasco, P. Enoksson, C. Johansson, J. Appl. Phys. 104 (2008) 093918.
[22] S.P. Yeap, P.Y. Toh, A.L. Ahmad, S.C. Low, S.A. Majetich, J.K. Lim, J. Phys. Chem. C 116 (2012) 22561–22569.
[23] S.P. Yeap, A.L. Ahmad, B.S. Ooi, J.K. Lim, Langmuir 28 (2012) 14878–14891.
[24] K.B. Lee, S. Park, C.A. Mirkin, Angew. Chem. Int. Ed. 116 (2004) 3110–3112.
[25] M.K. Gupta, D.D. Kulkarni, R. Geryak, S. Naik, V.V. Tsukruk, Nano Lett. 13 (2013) 36–42.
[26] J.K. Lim, D.X. Tan, F. Lanni, R.D. Tilton, S.A. Majetich, J. Magn. Magn. Mater. 321 (2009) 1557–1562.
[27] A.G. Roca, R. Costo, A.F. Rebolledo, S. Veintemillas-Verdaguer, P. Tartaj, T. González-Carreño, M.P. Morales, C.J. Serna, J. Phys. D: Appl. Phys. 42 (2009) 224002.
[28] J.A. Cribb, T.D. Meehan, S.M. Shah, K. Skinner, R. Superfine, Ann. Biomed. Eng. 38 (2010) 3311–3322.
[29] V.F. Puntes, K.M. Krishnan, A.P. Alivisatos, Science 291 (2001) 2115–2117.
[30] J.K. Lim, C. Lanni, E.R. Evarts, F. Lanni, R.D. Tilton, S.A. Majetich, ACS Nano 5 (2011) 217–226.
[31] L.E. Helseth, T. Skodvin, Meas. Sci. Technol. 20 (2009) 095202.
[32] M. Elimelech, J. Gregory, X. Jia, R.A. Williams, Particle Deposition and Aggregation: Measurement, Modelling and Simulation, Butterworth-Heinemann, Woburn, MA, 1995.
[33] F. Kim, S. Kwan, J. Akana, P. Yang, J. Am. Chem. Soc. 123 (2001) 4360–4361.
[34] P. Evans, W.R. Hendren, R. Atkinson, G.A. Wurtz, W. Dickson, A.V. Zayats, R.J. Pollard, Nanotechnology 17 (2006) 5746–5753.
[35] C.T. Lo, W.T. Lin, J. Phys. Chem. B 117 (2013) 5261–5270.
[36] A. Ditsch, P.E. Laibinis, D.I.C. Wang, A. Hatton, Langmuir 21 (2005) 6006–6018.
[37] Y. Gu, R. Burtovyy, J. Townsend, J.R. Owens, I. Luzinov, K.G. Korney, Soft Matter. 9 (2013) 8532–8539.
[38] J. Faraudo, J. Camacho, Colloid Polym. Sci. 288 (2010) 207–215.
[39] A. Tokarev, I. Luzinov, J.R. Owens, K.G. Kornev, Langmuir 28 (2012) 10064–10071.
[40] A. Ortega, J.G. de la Torre, J. Chem. Phys. 119 (2003) 9914–9919.
[41] A. Ghosh, P. Mandal, S. Karmakar, A. Ghosh, Phys. Chem. Chem. Phys. 15 (2013) 10817–10823.
[42] K. Ommering, J.H. Nieuwenhuis, Appl. Phys. Lett. 89 (2006) 142511.

Lim et al. Nanoscale Research Letters 2013, 8:381
http://www.nanoscalereslett.com/content/8/1/381

Nanoscale Research Letters
a SpringerOpen Journal

NANO REVIEW Open Access

Characterization of magnetic nanoparticle by dynamic light scattering

JitKang Lim[1,2*], Swee Pin Yeap[1], Hui Xin Che[1] and Siew Chun Low[1]

Abstract

Here we provide a complete review on the use of dynamic light scattering (DLS) to study the size distribution and colloidal stability of magnetic nanoparticles (MNPs). The mathematical analysis involved in obtaining size information from the correlation function and the calculation of *Z*-average are introduced. Contributions from various variables, such as surface coating, size differences, and concentration of particles, are elaborated within the context of measurement data. Comparison with other sizing techniques, such as transmission electron microscopy and dark-field microscopy, revealed both the advantages and disadvantages of DLS in measuring the size of magnetic nanoparticles. The self-assembly process of MNP with anisotropic structure can also be monitored effectively by DLS.

Keywords: Dynamic light scattering; Magnetic nanoparticles; Colloidal stability; Surface functionalization; Review

Review

Introduction

Magnetic nanoparticles (MNPs) with a diameter between 1 to 100 nm have found uses in many applications [1,2]. This nanoscale magnetic material has several advantages that provide many exciting opportunities or even a solution to various biomedically [3-5] and environmentally [6-8] related problems. Firstly, it is possible to synthesize a wide range of MNPs with well-defined structures and size which can be easily matched with the interest of targeted applications. Secondly, the MNP itself can be manipulated by an externally applied magnetic force. The capability to control the spatial evolution of MNPs within a confined space provides great benefits for the development of sensing and diagnostic system/techniques [9,10]. Moreover MNPs, such as Fe^0 and Fe_3O_4, that exhibit a strong catalytic function can be employed as an effective nanoagent to remove a number of persistent pollutants from water resources [11,12]. In addition to all the aforementioned advantages, the recent development of various techniques and procedures for producing highly monodispersed and size-controllable MNPs [13,14] has played a pivotal role in promoting the active explorations and research of MNPs.

In all of the applications involving the use of MNPs, the particle size remained as the most important parameter as many of the chemical and physical properties associated to MNPs are strongly dependent upon the nanoparticle diameter. In particular, one of the unique features of a MNP is its high-surface-to-volume ratio, and this property is inversely proportional to the diameter of the MNP. The smaller the MNP is, the larger its surface area and, hence, the more loading sites are available for applications such as drug delivery and heavy metal removal. Furthermore, nanoparticle size also determines the magnetophoretic forces (F_{mag}) experienced by a MNP since F_{mag} is directly proportional to the volume of the particles [15]. In this regard, having size information is crucial as at nanoregime, the MNP is extremely susceptible to Stoke's drag [16] and thermal randomization energy [17]. The successful manipulation of MNP can only be achieved if the F_{mag} introduced is sufficient to overcome both thermal and viscous hindrances [18]. In addition, evidences on the (eco)toxicological impacts of nanomaterials have recently surfaced [19]. The contributing factors of nanotoxicity are still a subject of debate; however, it is very likely due to either (1) the characteristic small dimensional effects of nanomaterials that are not shared by their bulk counterparts with the same chemical composition [20] or (2) biophysicochemical interactions at the nano-bio interface dictated by colloidal forces [21]. For either reason, the MNP's size is one of the determining factors.

* Correspondence: chjitkangl@eng.usm.my
[1]School of Chemical Engineering, Universiti Sains Malaysia, Nibong Tebal, Penang 14300, Malaysia
[2]Department of Physics, Carnegie Mellon University, Pittsburgh, PA 15213, USA

The technique of dynamic light scattering (DLS) has been widely employed for sizing MNPs in liquid phase [22,23]. However, the precision of the determined particle size is not completely understood due to a number of unevaluated effects, such as concentration of particle suspension, scattering angle, and shape anisotropy of nanoparticles [24]. In this review, the underlying working principle of DLS is first provided to familiarize the readers with the mathematical analysis involved for correct interpretation of DLS data. Later, the contribution from various factors, such as suspension concentration, particle shape, colloidal stability, and surface coating of MNPs, in dictating the sizing of MNPs by DLS is discussed in detail. It is the intention of this review to summarize some of the important considerations in using DLS as an analytical tool for the characterization of MNPs.

Overview of sizing techniques for MNPs

There are numerous analytical techniques, such as DLS [25], transmission electron miscroscopy (TEM) [26], thermomagnetic measurement [27], dark-field microscopy [17,18], atomic force microscopy (AFM) [28], and acoustic spectrometry measurement [29], that have been employed to measure the size/size distribution of MNPs (Table 1). TEM is one of the most powerful analytical tools available which can give direct structural and size information of the MNP. Through the use of the short wavelengths achievable with highly accelerated electrons, it is capable to investigate the structure of a MNP down to the atomic level of detail, whereas by performing image analysis on the TEM micrograph obtained, it is possible to give quantitative results on the size distribution of the MNP. This technique, however, suffered from the small sampling size involved. A typical MNP suspension composed of 10^{10} to 10^{15} particles/mL and the size analysis by measuring thousands or even tens of thousands of particles still give a relatively small sample pool to draw statistically conclusive remarks.

Thermomagnetic measurement extracts the size distribution of an ensemble of superparamagnetic nanoparticles from zero-field cooling (ZFC) magnetic moment, m_{ZFC} (T), data based on the Néel model [27]. This method is an indirect measurement of particle size and relies on the underlying assumption of the mathematical model used to calculate the size distribution. In addition, another limitation of this analytical method includes the magnetic field applied for ZFC measurements which must be small compared to the anisotropy field of the MNPs [30], and it also neglects particle-particle dipolar interactions which increase the apparent blocking temperature [31]. This technique, however, could give a very reliable magnetic size of the nanoparticle analyzed.

Table 1 Common analytical techniques and the associated range scale involved for nanoparticle sizing

Techniques	Approximated working size range
Dynamic light scattering	1 nm to approximately 5 μm
Transmission electron microscopy	0.5 nm to approximately 1 μm
Atomic force microscopy	1 nm to approximately 1 μm
Dark-field microscopy	5 to 200 nm
Thermomagnetic measurement	10 to approximately 50 nm

Dark-field microscopy relies on direct visual inspection of the optical signal emitted from the MNP while it undergoes Brownian motion. After the trajectories of each MNP over time t are recorded, the two-dimensional mean-squared displacement $\langle r^2 \rangle = 4Dt$ is used to calculate the diffusion coefficient D for each particle. Later on, the hydrodynamic diameters can be estimated via the Stokes-Einstein equation for the diffusion coefficients calculated for individual particles, averaging over multiple time steps [18]. Successful implementation of this technique depends on the ability to trace the particle optically by coating the MNP with a noble metal that exhibits surface Plasmon resonance within a visible wavelength. This extra synthesis step has significantly restricted the use of this technique as a standard route for sizing MNPs. The size of an MNP obtained through dark-field microscopy is normally larger than the TEM and DLS results [17]. It should be noted that dark-field microscopy can also be employed for direct visualization of a particle flocculation event [32]. As for AFM, besides the usual topographic analysis, magnetic imaging of a submicron-sized MNP grown on GaAs substrate has been performed with magnetic force microscopy equipment [33]. Despite all the recent breakthroughs, sample preparation and artifact observation are still the limiting aspect for the wider use of this technology for sizing MNPs [34].

The particle size and size distribution can also be measured with an acoustic spectrometer which utilizes the sound pulses transmitted through a particle suspension to extract the size-related information [29]. Based on the combined effect of absorption and scattering of acoustic energy, an acoustic sensor measures attenuation frequency spectra in the sample. This attenuation spectrum is used to calculate the particle size distribution. This technique has advantages over the light scattering method in studying samples with high polydispersity as the raw data for calculating particle size depend on only the third power of the particle size. This scenario makes contribution of the small (nano) and larger particles more even and the method potentially more sensitive to the nanoparticle content even in the very broad size distributions [35].

DLS, also known as photon correlation spectroscopy, is one of the most popular methods used to determine the size of MNPs. During the DLS measurement, the

MNP suspension is exposed to a light beam (electromagnetic wave), and as the incident light impinges on the MNP, the direction and intensity of the light beam are both altered due to a process known as scattering [36]. Since the MNPs are in constant random motion due to their kinetic energy, the variation of the intensity with time, therefore, contains information on that random motion and can be used to measure the diffusion coefficient of the particles [37]. Depending on the shape of the MNP, for spherical particles, the hydrodynamic radius of the particle R_H can be calculated from its diffusion coefficient by the Stokes-Einstein equation $D_f = k_B T/6\pi\eta R_H$, where k_B is the Boltzmann constant, T is the temperature of the suspension, and η is the viscosity of the surrounding media. Image analysis on the TEM micrographs gives the 'true radius' of the particles (though determined on a statistically small sample), and DLS provides the hydrodynamic radius on an ensemble average [38]. The hydrodynamic radius is the radius of a sphere that has the same diffusion coefficient within the same viscous environment of the particles being measured. It is directly related to the diffusive motion of the particles.

DLS has several advantages for sizing MNPs and has been widely used to determine the hydrodynamic size of various MNPs as shown in Table 2. First of all, the measuring time for DLS is short, and it is almost all automated, so the entire process is less labor intensive and an extensive experience is not required for routine measurement. Furthermore, this technique is noninvasive, and the sample can be employed for other purposes after the measurement. This feature is especially important for the recycle use of MNP with an expensive surface functional group, such as an enzyme or molecular ligands. In addition, since the scattering intensity is directly proportional to the sixth power of the particle radius, this technique is extremely sensitive towards the presence of small aggregates. Hence, erroneous measurement can be prevented quite effectively even with the occurrences of limited aggregation events. This unique feature makes DLS one of the very powerful techniques in monitoring the colloidal stability of MNP suspension.

Table 2 Hydrodynamic diameter of different MNPs determined by DLS

Type of MNPs	Surface coating	Hydrodynamic diameter by DLS (nm)	Reference
Fe^0	Carboxymethyl cellulose	15-19	[39]
	Guar gum	350-700	[40]
	Poly(methacrylic acid)-poly(methyl methacrylate)-poly (styrenesulfonate) triblock copolymer	100-600	[41]
	Poly(styrene sulfonate)	30-90	[22]
γ-Fe_2O_3	Oleylamine or oleic acid	5-20	[42]
	Poly(*N*,*N*-dimethylacrylamide)	55-614	[43]
	Poly(ethylene oxide)-block-poly(glutamic acid)	42-68	[44]
	Poly(ethylene Imine)	20-75	[45]
	Poly(ε-caprolactone)	193 ± 7	[46]
Fe_3O_4	Phospholipid-PEG	14.7 ± 1.4	[47]
	Polydimethylsiloxane	41.2 ± 0.4	[48]
	Oleic acid-pluronic	50-600	[49]
	Polyethylenimine (PEI)	50-150	[23,50]
	Polythylene glycol	10-100	[51]
	Triethylene glycol	16.5 ± 3.5	[52]
	Poly(*N*-Isopropylacrylamide)	15-60	[53]
	Pluronic F127	36	[54]
	Poly(sodium 4-styrene sulfonate)	~200	[55]
	Poly(diallyldimethylammonium chloride)	107.4 ± 53.7	[56]
FePt	Poly(diallyldimethylammonium chloride)	30-100	[57]
NiO	Cetyltrimethyl ammonium bromide	10-80	[58]
	Fetal bovine serum	39.05	[59]
	Not specified	750 ± 30	[60]
CoO, Co_2O_3	Poly(methyl methacrylate)	59-85	[61]
CoFe	Hydroxamic and phosphonic acids	6.5-458.7	[62]

The underlying principle of DLS

The interaction of very small particles with light defined the most fundamental observations such as why is the sky blue. From a technological perspective, this interaction also formed the underlying working principle of DLS. It is the purpose of this section to describe the mathematical analysis involved to extract size-related information from light scattering experiments.

The correlation function

DLS measures the scattered intensity over a range of scattering angles θ_{dls} for a given time t_k in time steps Δt. The time-dependent intensity $I(q, t)$ fluctuates around the average intensity $I(q)$ due to the Brownian motion of the particles [38]:

$$[I(q)] = \lim_{t_k\to\infty} 1/_{t_k} \int_0^{t_k} I(q,t)\cdot dt \approx \lim_{k\to\infty} \frac{1}{K} \Sigma_{i=1}^{k} I(q, i\cdot\Delta t) \quad (1)$$

where $[I(q)]$ represents the time average of $I(q)$. Here, it is assumed that t_k, the total duration of the time step measurements, is sufficiently large such that $I(q)$ represents average of the MNP system. In a scattering experiment, normally, θ_{dls} (see Figure 1) is expressed as the magnitude of the scattering wave vector q as

$$q = (4\pi n/\lambda)\sin(\theta_{dls}/2) \quad (2)$$

where n is the refractive index of the solution and λ is the wavelength in vacuum of the incident light. Figure 2a illustrates typical intensity fluctuation arising from a dispersion of large particles and a dispersion of small particles. As the small particles are more susceptible to random forces, the small particles cause the intensity to fluctuate more rapidly than the large ones.

The time-dependent intensity fluctuation of the scattered light at a particular angle can then be characterized with the introduction of the autocorrelation function as

$$c(q,\tau) = \lim_{t_k\to\infty} 1/_{t_k} \int_0^{t_k} I(q,t)\cdot I(q,t+\tau)\cdot dt \quad (3)$$

$$\approx \lim_{k\to\infty} \frac{1}{K} \Sigma_{j=0}^{k} I(q, i\cdot\Delta t)\cdot I(q, (i+j)\cdot\Delta t)$$

where $\tau = i\ \Delta t$ is the delay time, which represents the time delay between two signals $I(q,i\ \Delta t)$ and $I(q,(i + j)\ \Delta t)$. The function $C(q,\tau)$ is obtained for a series of τ and represents the correlation between the intensity at t_1 ($I(q,t_1)$) and the intensity after a time delay of τ ($I(q,t_1 + \tau)$). The last part of the equation shows how the autocorrelation function is calculated experimentally when the intensity is measured in discrete time steps [37]. As for nanoparticle dispersion, the autocorrelation function decays more rapidly for small particles than for the large particles as depicted in Figure 2b. The autocorrelation function has its highest value of $[I(q,0)]^2$ at $\tau = 0$. As τ becomes sufficiently large at long time scales, the fluctuations becomes uncorrelated and $C(q,\tau)$ decreases to $[I(q)]^2$. For non-periodic $I(q,t)$, a monotonic decay of $C(q,\tau)$ is observed as τ increases from zero to infinity and

$$C(q,\tau)/_{[I(q)]^2} = g^{(2)}(q,\tau) = 1 + \xi\left|g^{(1)}(q,\tau)\right|^2 \quad (4)$$

where ξ is an instrument constant approximately equal to unity and $g^{(1)}(q,\tau)$ is the normalized electric field correlation function [63]. Equation 4 is known as the Siegert relation and is valid except in the case of scattering volume with a very small number of scatterers or when the motion of the scatterers is limited. For monodisperse, spherical particles, $g^{(1)}(\tau)$ is given by

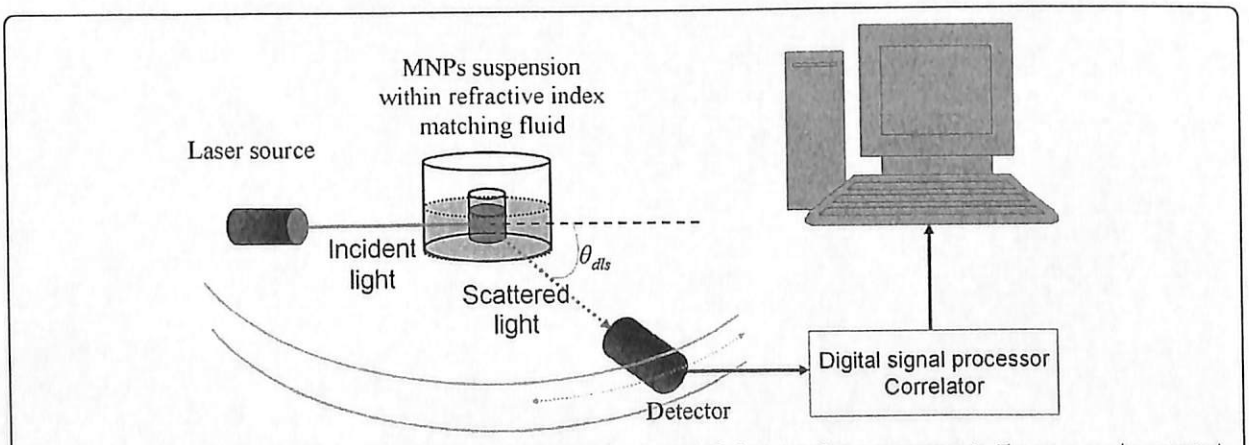

Figure 1 Optical configuration of the typical experimental setup for dynamic light scattering measurements. The setup can be operated at multiple angles.

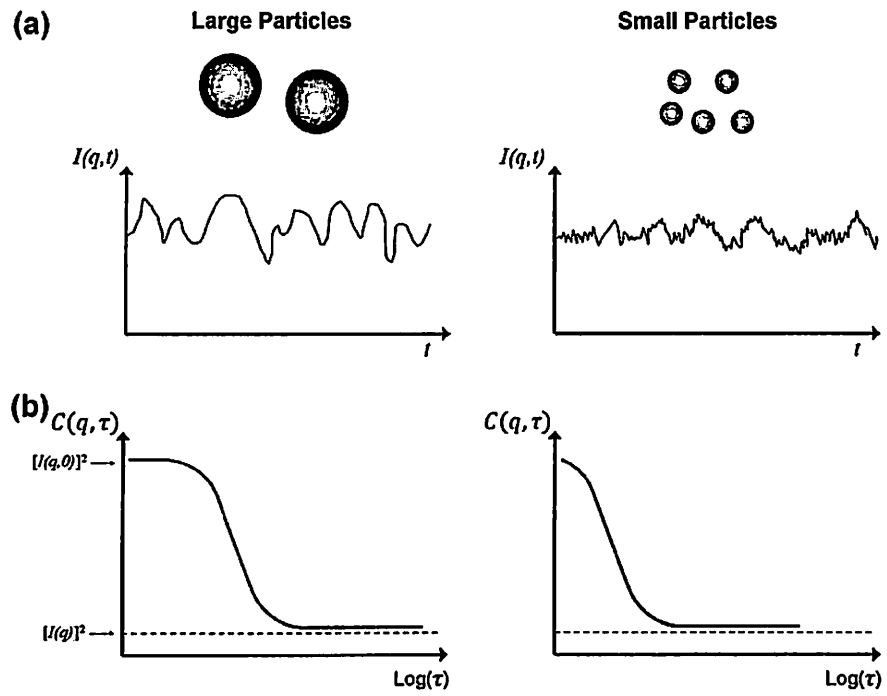

Figure 2 Schematic illustration of intensity measurement and the corresponding autocorrelation function in dynamic light scattering. The figure illustrates dispersion composed of large and small particles. **(a)** Intensity fluctuation of scattered light with time, and **(b)** the variation of autocorrelation function with delay time.

$$g^{(1)}(q,\tau) = \exp\left(-D_f q^2 \tau\right).$$

Once the value of D_f is obtained, the hydrodynamic diameter of a perfectly monodisperse dispersion composed of spherical particles can be inferred from the Stokes-Einstein equation. Practically, the correlation function observed is not a single exponential decay but can be expressed as

$$g^{(1)}(q,\tau) = \int_0^\infty G(\Gamma) e^{-\Gamma\tau} d\Gamma \tag{6}$$

where $G(\Gamma)$ is the distribution of decay rates Γ. For a narrowly distributed decay rate, cumulant method can be used to analyze the correlation function. A properly normalized correlation function can be expressed as

$$\ln\left(g^{(1)}(q,\tau)\right) = -\langle\Gamma\rangle\tau + \frac{\mu_2}{2}\tau^2 \tag{7}$$

where $\langle\Gamma\rangle$ is the average decay rate and can be defined as

$$\langle\Gamma\rangle = \int_0^\infty G(\Gamma)\Gamma d\Gamma \tag{8}$$

and $\mu_2 = \langle\Gamma\rangle^2 - \langle\Gamma^2\rangle$ is the variance of the decay rate distribution. Then, the polydispersity index (PI) is defined as PI = $\mu_2/\langle\Gamma\rangle^2$. The average hydrodynamic radius is obtained from the average decay rate $\langle\Gamma\rangle$ using the relation

$$R_H = \frac{k_B T}{6\pi\eta\langle\Gamma\rangle} q^2 \tag{9}$$

Z-average

In most cases, the DLS results are often expressed in terms of the *Z*-average. Since the *Z*-average arises when DLS data are analyzed through the use of the cumulant technique [64], it is also known as the "cumulant mean." Under Rayleigh scattering, the amount of light scattered by a single particle is proportional to the sixth power of its radius (volume squared). This scenario causes the averaged hydrodynamic radius determined by DLS to be also weighted by volume squared. Such an averaged property is called the *Z*-average. For particle suspension with discrete size distribution, the *Z*-average of some arbitrary property y would be calculated as

$$\langle y\rangle = \frac{\Sigma_i n_i R_{H,i}^6 y_i}{\Sigma_i n_i R_{H,i}^6} \tag{10}$$

where n_i is the number of particles of type i having a hydrodynamic radius of $R_{H,i}$ and property y. If we assume that this particle dispersion consists of exactly two sizes of particles 1 and 2, then Equation 10 yields

$$\langle y \rangle = \frac{n_1 R_{H,1}^6 y_1 + n_2 R_{H,2}^6 y_2}{n_1 R_{H,1}^6 + n_2 R_{H,2}^6} \tag{11}$$

where $R_{H,i}$ and y_i are the volume and arbitrary property for particle 1 (i = 1) and particle 2 (i = 2). Suppose that two particles 1 combined to form one particle 2 and assume that we start with n_0 total of particle 1, some of which combined to form n_2 number of particle 2. With this assumption, we have $n_1 = n_0 - n_2$ number of particle 1. Moreover, under this assumption $R_{H,2} = 2\ R_{H,1}$. Substitute these relations into Equation 11; then, the Z-average of property y becomes

$$\frac{\langle y \rangle}{y_1} = \frac{1 + \left(2\left(\frac{y_2}{y_1}\right) - 1\right) 2\left(\frac{n_2}{n_0}\right)}{1 + 2\left(\frac{n_2}{n_0}\right)} \tag{12}$$

where $2n_2/n_0$ is the fraction of total particle 1 existing as particle 2. Solving this fraction, we obtained

$$\frac{2n_2}{n_0} = \frac{\frac{\langle y \rangle}{y_1} - 1}{\frac{2y_2}{y_1} - \frac{\langle y \rangle}{y_1} - 1} \tag{13}$$

However, it should be noted that Z-average should only be employed to provide the characteristic size of the particles if the suspension is monomodal (only one peak), spherical, and monodisperse. As shown in Figure 3, for a mixture of particles with obvious size difference (bimodal distribution), the calculated Z-average carries irrelevant size information.

DLS measurement of MNPs

The underlying challenges of measuring the size of MNPs by DLS lay in the facts that (1) for engineering applications, these particles are typically coated with macromolecules to enhance their colloidal stability (see Figure 4) and (2) there present dipole-dipole magnetic interactions between the none superparamagnetic nanoparticles. Adsorbing macromolecules onto the surface of particles tends to increase the apparent R_H of particles. This increase in R_H is a convenient measure of the thickness of the adsorbed macromolecules [65]. This section is dedicated to the scrutiny of these two phenomena and also suspension concentration effect in dictating the DLS measurement of MNPs. All DLS measurements were performed with a Malvern Instrument Zetasizer Nano Series (Malvern Instruments, Westborough, MA, USA) equipped with a He-Ne laser (λ = 633 nm, max 5 mW) and operated at a scattering angle of 173°. In all measurements, 1 mL of particle suspensions was employed and placed in a 10 mm × 10 mm quartz cuvette. The iron oxide MNP used in this study was synthesized by a high-temperature decomposition method [17].

Size dependency of MNP in DLS measurement

In order to demonstrate the sizing capability of DLS, measurements were conducted on three species of Fe_3O_4 MNPs produced by high-temperature decomposition method which are surface modified with oleic acid/oleylamine in toluene (Figure 5). The TEM image analyses performed on micrographs shown in Figure 5 (from top to bottom) indicate that the diameter of each particle species is 7.2 ± 0.9 nm, 14.5 ± 1.8 nm, and 20.1 ± 4.3 nm, respectively. The diameters of these particles obtained from TEM and DLS are tabulated in Table 3. It is very likely that the main differences between the measured diameters from these two techniques are due to

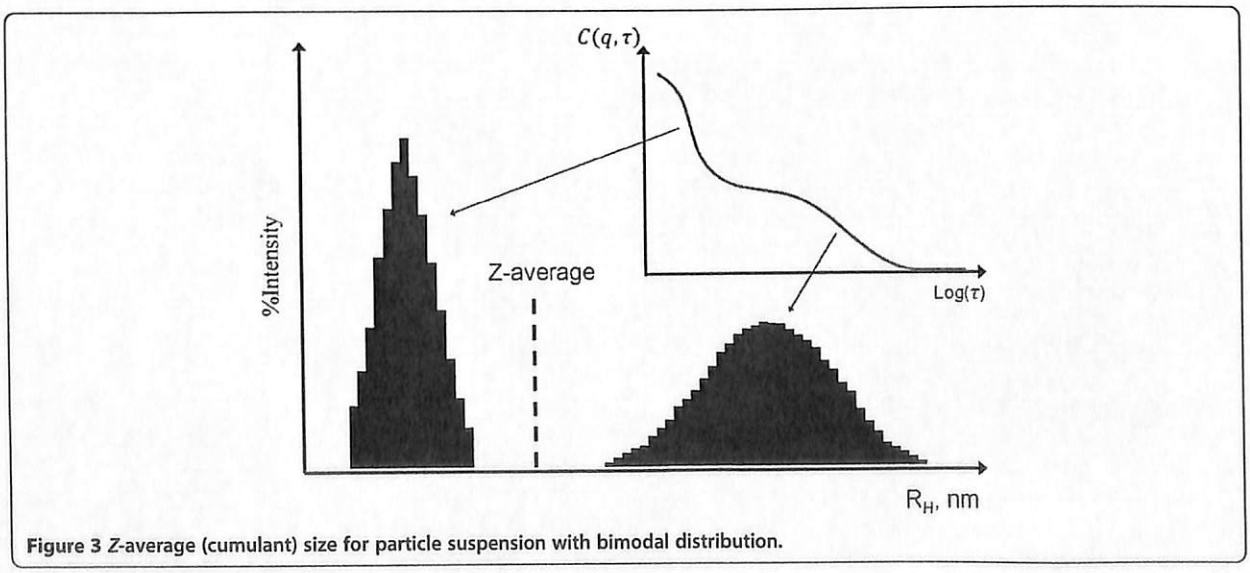

Figure 3 *Z*-average (cumulant) size for particle suspension with bimodal distribution.

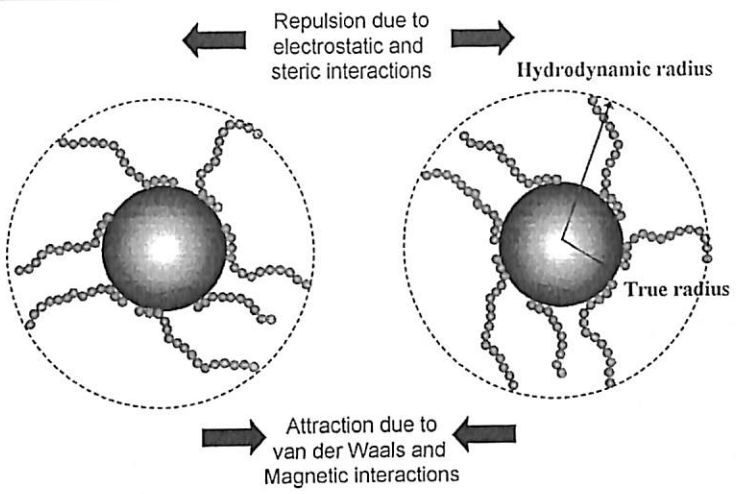

Figure 4 Pictorial representation of two MNPs and major interactions. The image shows two MNPs coated with macromolecules with repeated segments and the major interactions involved between them in dictating the colloidal stability of MNP suspension.

the presence of an adsorbing layer, which is composed of oleic acid (OA) and oleylamine (OY), on the surface of the particle. Small molecular size organic compounds, such as OA and OY, are electron transparent, and therefore, they did not show up in the TEM micrograph (Figure 5). Given that the chain lengths of OA and OY are approximately 2 nm [66,67], the best match of DLS and TEM, in terms of measured diameter, can be observed from middle-sized Fe_3O_4 MNPs.

For small-sized MNPs, the radius of curvature effect is the main contributing factor for the large difference observed on the averaged diameter from DLS and TEM. This observation has at least suggested that for any inference of layer thickness from DLS measurement, the particles with a radius much larger than the layer thickness should be employed. In this measurement, the fractional error in the layer thickness can be much larger than the fractional error in the radius with the measurement standard deviation of only 0.9 nm for TEM but at a relatively high value of 5.2 nm for DLS. At a very large MNP size of around 20 nm (bottom image of Figure 5), the *Z*-average hydrodynamic diameter is 23 nm larger than the TEM size. Moreover, the standard deviation of the DLS measurement of this particle also increased significantly to 14.9 nm compared to 5.2 and 5.5 nm for small- and middle-sized MNPs, respectively. This trend of increment observed in standard deviation is consistent with TEM measurement. Both the shape irregularity and polydispersity, which are the intrinsic properties that can be found in a MNP with a diameter of 20 nm or above, contribute to this observation. For a particle larger than 100 nm, other factors such as electroviscous and surface roughness effects should be taken into consideration for the interpretation of DLS results [68].

MNP concentration effects

In DLS, the range of sample concentration for optimal measurements is highly dependent on the sample materials and their size. If the sample is too dilute, there may be not enough scattering events to make a proper measurement. On the other hand, if the sample is too concentrated, then multiple scattering can occur. Moreover, at high concentration, the particle might not be freely mobile with its spatial displacement driven solely by Brownian motion but with the strong influences of particle interactions. This scenario is especially true for the case of MNPs with interparticle magnetic dipole-dipole interactions.

Figure 6 illustrates the particle concentration effects on 6- and 18-nm superparamagnetic iron oxide MNPs, with no surface coating, dispersed in deionized water. Both species of MNPs show strong concentration dependency as their hydrodynamic diameter increases with the concentration increment. The hydrodynamic diameter for small particles increases from 7.1 ± 1.9 nm to 13.2 ± 3.3 nm as the MNP concentration increases from 25 to 50 mg/L. On the other hand, the hydrodynamic diameter of large particles remains to be quite constant until around 100 mg/L and then only experiences a rapid jump of the detected size from 29.3 ± 4.6 nm (at 100 mg/L) to 177.3 ± 15.8 nm (at 250 mg/L). Since the concentration of the MNP is prepared in mass basis, the presence of an absolute number of particles in a given volume of solution is almost two orders of magnitude higher in a small-particle suspension. For example, at 100 mg/L, the concentrations for small and larger particles are calculated as 1.7×10^{20} particles (pts)/m^3 and 6.3×10^{18} pts/m^3 by assuming that the composition material is magnetite with a density of 5.3 g/cm^3. This

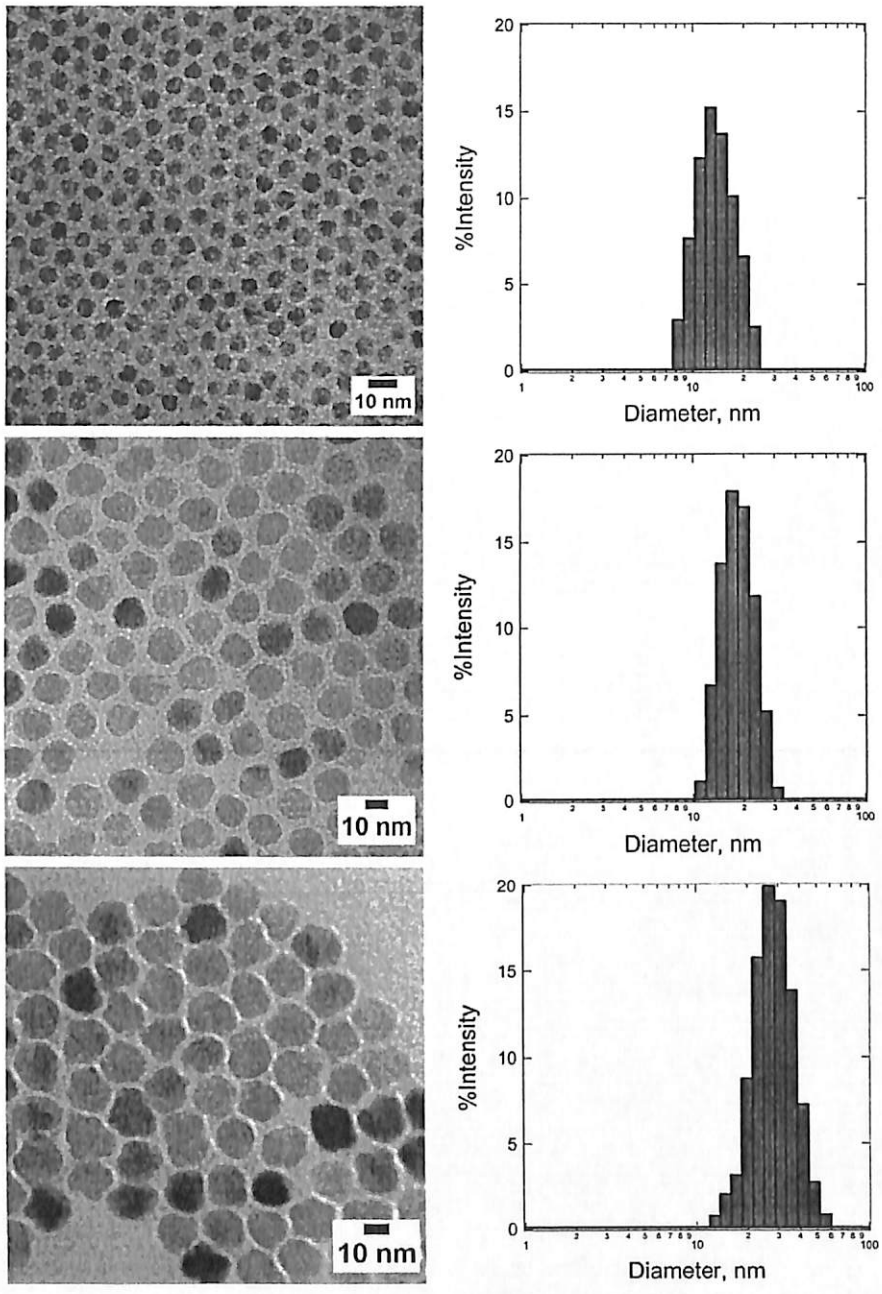

Figure 5 TEM micrographs of Fe_3O_4 MNPs with their size distribution determined by DLS. The *Z*-average of MNP calculated from the DLS data is (top) 16.9 ± 5.2 nm, (middle) 21.1 ± 5.5 nm, and (bottom) 43.1 ± 14.9 nm, respectively.

Table 3 Diameter of Fe_3O_4 MNP determined by TEM and DLS (*Z*-average)

Particle	TEM (nm)	DLS (nm)	Difference (nm)
Fe_3O_4	7.2	16.9	9.7
	14.5	21.1	6.6
	20.1	43.1	23.0

concentration translated to a collision frequency of 85,608 s^{-1} and 1,056 s^{-1}. So, at the same mass concentration, it is more likely for small particles to experience the non-self-diffusion motions.

For both species of particles, the upward trends of hydrodynamic diameter, which associates to the decrement of diffusion coefficient, reflect the presence of a strong interaction between the particles as MNP concentration

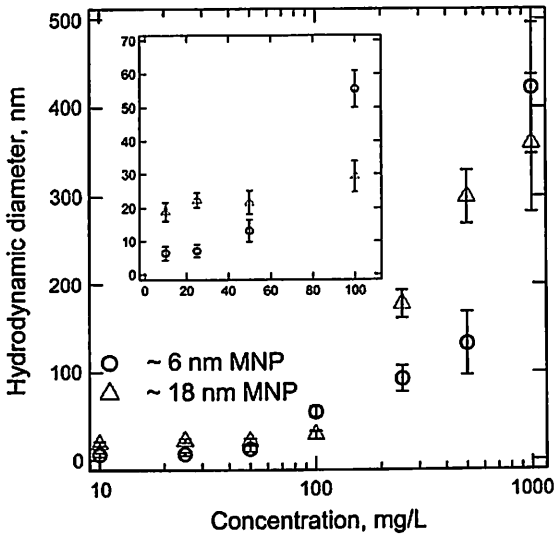

Figure 6 Particle concentration effects on the measurement of hydrodynamic diameter by DLS.

increases. Furthermore, since the aggregation rate has a second-order dependency on particle concentration [69], the sample with high MNP concentration has higher tendency to aggregate, leading to the formation of large particle clusters. Therefore, the initial efforts for MNP characterization by using DLS should focus on the determination of the optimal working concentration.

Colloidal stability of MNPs

Another important use of DLS in the characterization of MNPs is for monitoring the colloidal stability of the particles [70]. An iron oxide MNP coated with a thin layer of gold with a total diameter of around 50 nm is further subjected for surface functionalization by a variety of macromolecules [65]. The colloidal stability of the MNP coated with all these macromolecules suspended in 154 mM ionic strength phosphate buffer solution (PBS) (physiologically relevant environment for biomedical application) is monitored by DLS over the course of 5 days (Figure 7). The uncoated MNP flocculated immediately after their introduction to PBS and is verified with the detection of micron-sized objects by DLS.

As shown in Figure 7, both polyethylene glycol (PEG) 6k and PEG 10k are capable of tentatively stabilizing the MNPs in PBS for the first 24 and 48 h. Aggregation is observed with the detection of particle clusters with a diameter of more than 500 nm. After this period of relative stability, aggregation accelerated to produce micron-sized aggregates by day 3. Actually, the continuous monitoring of MNP size by DLS after this point is less meaningful as the dominating motion is the sedimentation of large aggregates [71]. For PEG 6k and PEG 10k that have a rather low degree of polymerization, the loss of stability over a day or two could have been due to slow PEG desorption that would not be expected of larger polymers. Nevertheless, PEG 100k-coated MNPs were not as well stabilized as the PEG 6k- or PEG 10k-coated ones, despite the higher degree of polymerization that one might expect to produce greater adsorbed layer thicknesses and therefore longer-ranged steric forces. In addition to the degree of polymerization, as discussed by Golas and coworkers [72], the colloidal stability of polymeric stabilized MNPs is also dependent on other structural differences of the polymer employed, such as the chain architecture and the identity of the charged functional unit. In their work, DLS was used to confirm the nanoparticle suspensions that displayed the least sedimentation which was indeed stable against aggregation.

In addition to the popular use of DLS in sizing individual MNPs, this analytical technique is also being employed to monitor the aggregation behavior of MNPs and the size of final clusters formed [55,73]. The study of particle aggregates is important since the magnetic collection is a cooperative phenomenon [74,75]. Subsequently, it is much easier to harvest submicron-sized MNP clusters than individual particles. Hence, a magnetic nanocluster with loss-packed structure and uniform size and shape has huge potential for various engineering applications in which the real-time separation is the key requirement [76]. Therefore, the use of DLS to monitor the aggregation kinetic of MNPs is important to provide direct feedback about the time scale associated with this process [55,77]. Figure 8 illustrates the aggregation behavior of three species of 40-nm reactive nanoscale iron particles (RNIP), 27.5-nm magnetite (Fe_3O_4) MNP, and 40-nm hematite (α-Fe_2O_3) MNP [73]. Phenrat and coworkers have demonstrated that DLS can be an effective tool to probe the aggregation behavior of MNPs (Figure 8a). The time evolution of the hydrodynamic radius of these particles from monomodal to bimodal distribution revealed the aggregation kinetic of the particles. Together with the in situ optical microscopy observation, the mechanism of aggregation is proposed as the transitions from rapidly moving individual MNPs to the formation of submicron clusters that lead to chain formation and gelation (Figure 8b). By the combination of small-angle neutron scattering and cryo-TEM measurements, DLS can also be used as an effective tool to understand the fractal structure of this aggregate [78].

DLS measurement of non-spherical MNPs

Even though, under most circumstances, a more specialized analytical technique known as depolarized dynamic light scattering is needed to investigate the structural contribution of anisotropic materials [79], it is still possible to extract useful information for rod-like MNPs by

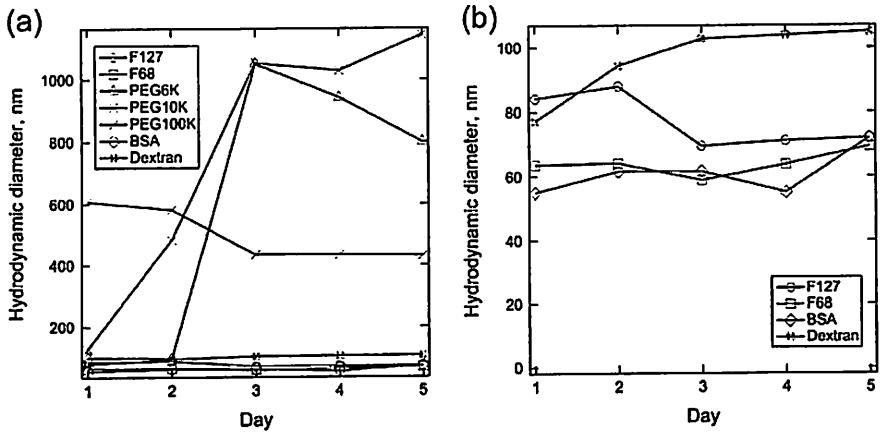

Figure 7 Intensity-weighted average hydrodynamic diameter for core-shell nanoparticles with different adsorbed macromolecules in PBS. (a) Extensive aggregation is evident with PEG 6k, PEG10k, and PEG100k, while **(b)** bovine serum albumin (BSA), dextran, Pluronic F127, and Pluronic F68 provided stable hydrodynamic diameters over the course of 5 days. 'Day 0' corresponds to the start of the overnight adsorption of macromolecules to the MNPs. Copyright 2009 American Chemical Society. Reprinted with permission from [65].

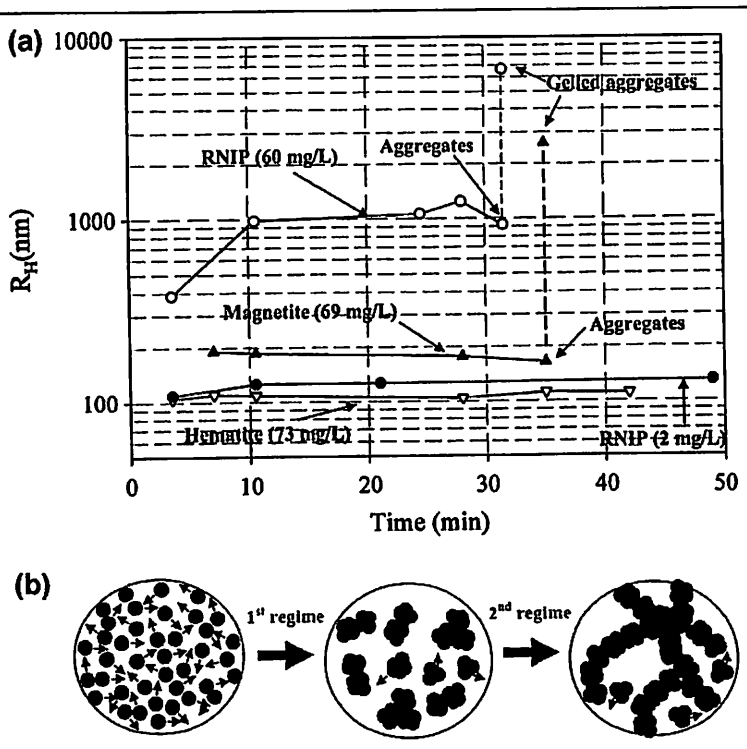

Figure 8 Evolution of hydrodynamic radius and MNP aggregation and gelation. (a) Evolution of the average hydrodynamic radius of dominant size class of MNPs as a function of time for RNIP (Fe^0/Fe_3O_4), magnetite, and hematite at pH 7.4. The particle size distribution for RNIP and magnetite becomes bimodal at the last measured point due to gelation of aggregates. **(b)** Rapid MNP aggregation and subsequent chain-like gelation: rapid aggregation of MNP to form micron-sized clusters (first regime) and chain-like aggregation and gelation of the micron-sized aggregates (second regime). Copyright 2007 American Chemical Society. Reprinted with permission from [73].

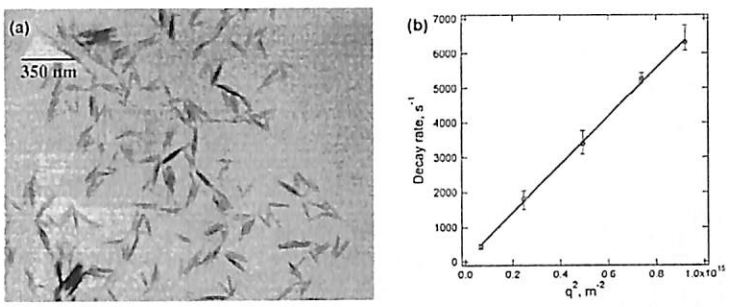

Figure 9 TEM images and graph of decay rate. **(a)** TEM images of β-FeOOH nanorods and **(b)** angle-dependent decay rate Γ of the nanorod showing a linear trend. Copyright 2009 Elsevier. Reprinted with permission from [86].

conventional DLS measurement [80,81]. For rod-like particles, the decay rate in Equation 6 can be defined as

$$\Gamma = q^2 D_T + 6D_R \tag{14}$$

where in a plot of Γ vs q^2, the value of rotational diffusion D_R can be obtained directly by an extrapolation of q to zero and the value of translational diffusion D_T from the slope of the curve [79]. For rigid non-interacting rods at infinite dilution with an aspect ratio (L/d) greater than 5, D_R and D_T can be expressed using Broersma's relations [82,83] or the stick hydrodynamic theory [84]. By performing angle-dependent DLS analysis on rod-like β-FeOOH nanorods as shown in Figure 9a, we found that the decay rate is linearly proportional to q^2 and passes through the origin (Figure 9b), suggesting that the nanorod motion is dominated by translational diffusion [85]. From Figure 9b, the slope of the graph yields the translational diffusion coefficient, $D_T = 7 \times 10^{-12}$ m^2/s. This value of D_T corresponds to an equivalent spherical hydrodynamic diameter of 62.33 nm, suggesting that the DLS results with a single fixed angle of 173° overestimated the true diameter [86]. By taking the length and width of the nanorods as 119.7 and 17.5 nm (approximated from TEM images in Figure 9a), the D_T calculated by the stick hydrodynamic theory and Broersma's relationship is 7.09 $\times 10^{-12}$ m^2/s and 6.84 $\times 10^{-12}$ m^2/s, respectively, consistent with the DLS results.

Since the β-FeOOH nanorods are self-assembled in a side-by-side fashion to form highly oriented 2-D nanorod arrays and the 2-D nanorod arrays are further stacked in a face-to-face fashion to form the final 3-D layered architectures, DLS can serve as an effective tool to monitor these transient behaviors [87]. Figure 10a depicts the structural changes of self-assembled nanorods over a time course of 7 h. To monitor the in situ real-time behavior of this self-assembly process, DLS was employed to provide the size distribution of the intermediate products that formed in the solution (Figure 10b). The temporal evolution of the detected size from 60 to 70 nm, to dual peaks, to eventually only a single distribution with a peak value of 700 nm

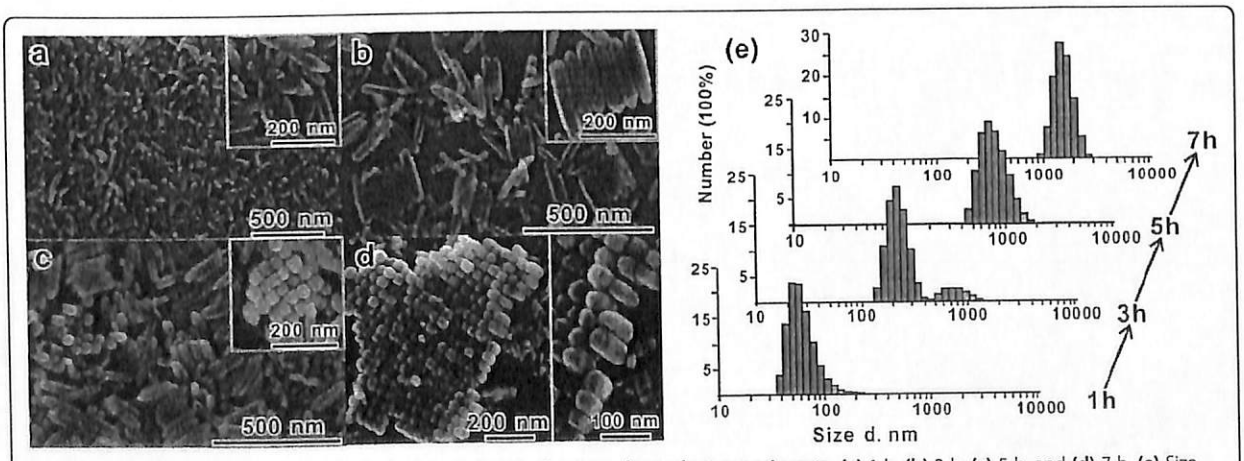

Figure 10 SEM images of the morphological evolution in the time-dependent experiments. **(a)** 1 h, **(b)** 3 h, **(c)** 5 h, and **(d)** 7 h. **(e)** Size distribution of the products obtained in the time-dependent experiments was monitored by DLS with the number averaged. Copyright 2010 American Chemical Society. Reprinted with permission from [87].

indicating that all the building blocks are self-assembled into the large aggregates within the experiment time frame agrees well with the SEM observation (Figure 10a). This kinetic data time scale is involved in the full assembly of anisotropic nanomaterials from single building blocks to 2-D arrays and, eventually, 3-D micron-sized assemblies.

Conclusion

Dynamic light scattering is employed to monitor the hydrodynamic size and colloidal stability of the magnetic nanoparticles with either spherical or anisotropic structures. This analytical method cannot be employed solely to give feedbacks on the structural information; however, by combining with other electron microscopy techniques, DLS provides statistical representative data about the hydrodynamic size of nanomaterials. In situ, real-time monitoring of MNP suspension by DLS provides useful information regarding the kinetics of the aggregation process and, at the same time, gives quantitative measurement on the size of the particle clusters formed. In addition, DLS can be a powerful technique to probe the layer thickness of the macromolecules adsorbed onto the MNP. However, the interpretation of DLS data involves the interplay of a few parameters, such as the size, concentration, shape, polydispersity, and surface properties of the MNPs involved; hence, careful analysis is needed to extract the right information.

Competing interests

The authors declare that they have no competing interests.

Authors' contributions

JKL synthesized the MNPs, carried out TEM analysis, and drafted the manuscript. SPY carried out DLS measurement and data analysis. HXC carried out DLS measurement and data analysis. SCL participated in the design of the study and drafted the manuscript. All authors read and approved the final manuscript.

Acknowledgements

This material is based on the work supported by Research University (RU) (grant no. 1001/PJKIMIA/811219) from Universiti Sains Malaysia (USM), Exploratory Research Grants Scheme (ERGS) (grant no. 203/PJKIMIA/6730013) from the Ministry of Higher Education of Malaysia, and eScience Fund (grant no. 205/PJKIMIA/6013412) from MOSTI Malaysia. JKL and SWL are affiliated to the Membrane Science and Technology Cluster of USM.

Received: 7 August 2013 Accepted: 30 August 2013
Published: 8 September 2013

References

1. Lu AH, Salabas EL, Schüth F: Magnetic nanoparticles: synthesis, protection, functionalization, and application. *Angew Chem Int Ed* 2007, 46:1222–1244.
2. Pankhurst QA, Connolly J, Jones SK, Dobson J: Applications of magnetic nanoparticles in biomedicine. *J Phys D Appl Phys* 2003, 36:R167.
3. Adolphi NL, Huber DL, Bryant HC, Monson TC, Fegan DL, Lim JK, Trujillo JE, Tessier TE, Lovato DM, Butler KS, Provencio PP, Hathaway HJ, Majetich SA, Larson RS, Flynn ER: Characterization of single-core magnetite nanoparticles for magnetic imaging by SQUID relaxometry. *Phys Med Biol* 2010, 55:5985–6003.
4. Gupta AK, Gupta M: Synthesis and surface engineering of iron oxide nanoparticles for biomedical applications. *Biomaterials* 2005, 25:3995–4021.
5. Hao R, Xing R, Xu Z, Hou Y, Gao S, Sun S: Sythesis, functionalization and biomedical applications of multifunctional magnetic nanoparticles. *Adv Mater* 2010, 22:2729–2742.
6. Cumbat L, Greenleaf J, Leun D, SenGupta AK: Polymer supported inorganic nanoparticles: characterization and environmental applications. *React Funct Polym* 2003, 54:167–180.
7. Yantasee W, Warner CL, Sangvanich T, Addleman RS, Carter TG, Wiacek RJ, Fryxell GE, Timchalk C, Warner MG: Removal of heavy metals from aqueous systems with thiol functionalized superparamagnetic nanoparticles. *Environ Sci Technol* 2007, 41:5114–5119.
8. Hu J, Lo IMC, Chen G: Comparative study of various magnetic nanoparticles for Cr(VI) removal. *Sep Purif Technol* 2007, 56:249–256.
9. Dobson J: Remote control of cellular behavior with magnetic nanoparticles. *Nat Nanotech* 2008, 3:139–143.
10. Gao J, Zhang W, Huang P, Zhang B, Zhang X, Xu B: Intracellular spatial control of fluorescent magnetic nanoparticles. *J Am Chem Soc* 2008, 130:3710–3711.
11. Fiedor JN, Bostick WD, Jarabek RJ, Farrell J: Understanding the mechanism of uranium removal from groundwater by zero-valent iron using X-ray photoelectron spectroscopy. *Environ Sci Technol* 1998, 32:1466–1473.
12. Feng J, Hu X, Yue PL, Zhu HY, Lu GQ: Degradation of azo-dye orange II by a photoassisted Fenton reaction using a novel composite of iron oxide and silicate nanoparticles as a catalyst. *Ind Eng Chem Res* 2003, 42:2058–2066.
13. Sun S: Recent advances in chemical synthesis, self-assembly, and applications of FePt nanoparticles. *Adv Mater* 2006, 18:393–403.
14. Park J, Joo J, Kwon SG, Jang Y, Hyeon T: Synthesis of monodisperse spherical nanocrystals. *Angew Chem Int Ed* 2007, 46:4630–4660.
15. Zborowski M, Sun L, Moore LR, Williams PS, Chalmers JJ: Continuous cell separation using novel magnetic quadrupole flow sorter. *J Magn Magn Mater* 1999, 194:224–230.
16. Purcell EM: Life at low Reynolds number. *Am J Phys* 1977, 45:3–11.
17. Lim JK, Eggeman A, Lanni F, Tilton RD, Majetich SA: Synthesis and single-particle optical detection of low-polydispersity plasmonic-superparamagnetic nanoparticles. *Adv Mater* 2008, 20:1721–1726.
18. Lim JK, Lanni C, Evarts ER, Lanni F, Tilton RD, Majetich SA: Magnetophoresis of nanoparticles. *ACS Nano* 2011, 5:217–226.
19. Nel A, Xia T, Mädler L, Li N: Toxic potential of materials at the nanolevel. *Science* 2006, 311:622–627.
20. Auffan M, Rose J, Bottero JY, Lowry GV, Jolivet JP, Wiesner MR: Towards a definition of inorganic nanoparticles from an environmental, health and safety perspective. *Nat Nanotech* 2009, 4:634–641.
21. Nel A, Madler T, Velegol D, Xia T, Hoek E, Somasundaran P, Klaessig F, Castranova V, Thompson M: Understanding biophysicochemical interactions at the nano-bio interface. *Nat Mater* 2009, 8:543–557.
22. Phenrat T, Kim HJ, Fagerlund F, Illangasekare T, Tilton RD, Lowry GV: Particle size distribution, concentration, and magnetic attraction affect transport of polymer-modified Fe^0 nanoparticles in sand columns. *Environ Sci Technol* 2009, 43:5079–5085.
23. Goon IY, Lai LMH, Lim M, Munroe P, Gooding JJ, Amal R: Fabrication and dispersion of gold-shell-protected magnetite nanoparticles: systematic control using polyethyleneimine. *Chem Mater* 2009, 21:673–681.
24. Takahashi K, Kato H, Saito T, Matsuyama S, Kinugasa S: Precise measurement of the size of nanoparticles by dynamic light scattering with uncertainty analysis. *Part Part Syst Charact* 2008, 25:31–38.
25. Goldburg WI: Dynamic light scattering. *Am J Phys* 1999, 67:1152–1160.
26. Chatterjee J, Haik Y, Chen CJ: Size dependent magnetic properties of iron oxide nanoparticles. *J Magn Magn Mater* 2003, 257:113–118.
27. DiPietro RS, Johnson HG, Bennett SP, Nummy TJ, Lewis LH: Determining magnetic nanoparticle size distributions from thermomagnetic measurements. *Appl Phys Lett* 2010, 96:222506.
28. Silva LP, Lacava ZGM, Buske N, Morais PC, Azevedo RB: Atomic force microscopy and transmission electron microscopy of biocompatible magnetic fluids: a comparative analysis. *J Nanopart Res* 2004, 6:209–213.
29. Dukhin AS, Goetz PJ: Acoustic and electroacoustic spectroscopy. *Langmuir* 1996, 12:4336–4344.
30. Chantrell RW, Wohlfarth EP: Rate dependent of the field-cooled magnetisation of a fine particle system. *Phys Status Solidi A* 1985, 91:619–626.

31. El-Hilo M, O'Grady K, Chantrell RW: Susceptibility phenomena in a fine particle system: I. Concentration dependence of peak. *J Magn Magn Mater* 1992, 114:295–306.
32. Jans H, Liu X, Austin L, Maes G, Huo Q: Dynamic light scattering as a powerful tool for gold nanoparticle bioconjugation and biomolecular binding studies. *Anal Chem* 2009, 81:9425–9432.
33. Ando K, Chiba A, Tanoue H: Uniaxial magnetic anisotropy of submicron MnAs ferromagnets in GaAs semiconductors. *Appl Phys Lett* 1998, 73:387.
34. Lacava LM, Lacava BM, Azevedo RB, Lacava ZGM, Buske N, Tronconi AL, Morais PC: Nanoparticles sizing: a comparative study using atomic force microscopy, transmission electron microscopy, and ferromagnetic resonance. *J Magn Magn Mater* 2001, 225:79–83.
35. Dukhin AS, Goetz PJ, Fang X, Somasundaran P: Monitoring nanoparticles in the presence of larger particles in liquids using acoustics and electron microscopy. *J Colloid Interface Sci* 2010, 342:18–25.
36. Van de Hulst HC: *Light Scattering by Small Particles*. New York: Dover Publications; 1981.
37. Hiemenz PC, Rajagopalan R: *Principles of Colloid and Surface Chemistry*. 3rd edition. New York: Marcel Dekker; 1997.
38. Berne BJ, Pecora R: *Dynamic Light Scattering: With Applications to Chemistry, Biology and Physics*. New York: Dover Publications; 2000.
39. He F, Zhao D: Manipulating the size and dispersibility of zerovalent iron nanoparticles by use of carboxymethyl cellulose stabilizers. *Environ Sci Technol* 2007, 41:6216–6221.
40. Tiraferri A, Chen KL, Sethi R, Elimelech M: Reduced aggregation and sedimentation of zero valent iron nanoparticles in the presence of guar gum. *J Colloid Interface Sci* 2008, 324:71–79.
41. Saleh N, Phenrat T, Sirk K, Dufour B, Ok J, Sarbu T, Matyjaszewski K, Tilton RD, Lowry GV: Adsorbed triblock copolymer deliver reactive iron nanoparticles to the oil/water interface. *Nano Lett* 2005, 5:2489–2494.
42. Vidal-Vidal J, Rivas J, López-Quintela MA: Synthesis of monodisperse maghemite nanoparticles by the microemulsion method. *Colloid Suface A: Physiochem Eng Aspects* 2006, 288:44–51.
43. Babič M, Horák D, Jendelová P, Glogarová K, Herynek V, Trchová M, Likavčannová K, Lesny P, Pollert E, Hájek M, Syková E: Poly(N, N-dimethylacrylamide)-coated maghemite nanoparticles for stem cell labelling. *Bioconjugate Chem* 2009, 20:283–294.
44. Kaufner L, Cartier R, Wüstneck R, Fichtner I, Pietschmann S, Bruhn H, Schütt D, Thünemann AF, Pison U: Poly(ethylene oxide)-block-poly(glutamic acid) coated maghemite nanoparticles: in vitro characterization and in vivo behavior. *Nanotechnology* 2007, 18:115710.
45. Thünemann AF, Schütt D, Kaufner L, Pison U, Möhwald H: Maghemite nanoparticles protectively coated with poly(ethyleneimine) and poly (ethylene oxide)-block-poly(glutamic acid). *Langmuir* 2006, 22:2351–2357.
46. Flesch C, Bourgeat-Lami E, Mornet S, Duguet E, Delaite C, Dumas P: Synthesis of colloidal superparamagnetic nanocomposites by grafting poly(ε-caprolactone) from the surface of organosilane-modified maghemite nanoparticles. *J Polym Sci A1* 2005, 43:3221–3231.
47. Nitin N, LaConte LEW, Zurkiya O, Hu X, Bao G: Functionalization and peptide-based delivery of magnetic nanoparticles as an intracellular MRI contrast agent. *J Biol Inorg Chem* 2004, 9:706–712.
48. Thompson Mefford O, Vadala ML, Goff JD, Carroll MRJ, Mejia-Ariza R, Caba BL, St Pierre TG, Woodward RC, Davis RM, Riffle JS: Stability of polydimethysiloxane-magnetite nanoparticle dispersions against flocculation: interparticle interactions of polydisperse materials. *Langmuir* 2008, 24:5060–5069.
49. Jain TK, Morales MA, Sahoo SK, Leslie-Pelecky DL, Labhasetwar V: Iron oxide nanoparticles for sustained delivery of anticancer agents. *Mol Pharmaceutics* 2005, 2:194–205.
50. Arsianti M, Lim M, Lou SN, Goon IY, Marquis CP, Amal R: Bi-functional gold-coated magnetite composites with improved biocompatibility. *J Colloid Interface Sci* 2011, 354:536–545.
51. Xie J, Xu C, Kohler N, Hou Y, Sun S: Controlled PEGylation of monodispersed Fe_3O_4 nanoparticles for reduced non-specific uptake by macrophage cells. *Adv Mater* 2007, 19:3163–3166.
52. Wan J, Cai W, Meng X, Liu E: Monodisperse water-soluble magnetite nanoparticles prepared by polyol process for high-performance magnetic resonance imaging. *Chem Commun* 2007,5004–5006.
53. Narain R, Gonzales M, Hoffman AS, Stayton PS, Krishnan KM: Synthesis of monodisperse biotinylated p(NIPAAm)-coated iron oxide magnetic nanoparticles and their bioconjugation to streptavidin. *Langmuir* 2007, 23:6299–6304.
54. Gonzales M, Krishnan KM: Phase transfer of highly monodisperse iron oxide nanocrystals with Pluronic F127 for biomedical applications. *J Magn Magn Mater* 2007, 311:59–62.
55. Yeap SW, Ahmad AL, Ooi BS, Lim JK: Electrosteric stabilization and its role in cooperative magnetophoresis of colloidal magnetic nanoparticles. *Langmuir* 2012, 28:14878–14891.
56. Lim JK, Derek CJC, Jalak SA, Toh PY: Mat Yasin NH, Ng BW, Ahmad AL: rapid magnetophoretic separation of microalgae. *Small* 2012, 8:1683–1692.
57. Taylor RM, Huber DL, Monson TC, Ali AMS, Bisoffi M, Sillerud LO: Multifunctional iron platinum stealth immunomicelles: targeted detection of human prostate cancer cells using both fluorescence and magnetic resonance imaging. *J Nanopart Res* 2011, 13:4717–4729.
58. Ahmad T, Ramanujachary KV, Lofland SE, Ganguli AK: Magnetic and electrochemical properties of nickel oxide nanoparticles obtained by the reverse-micellar route. *Solid State Sci* 2006, 8:425–430.
59. Horie M, Fukui H, Nishio K, Endoh S, Kato H, Fujita K, Miyauchi A, Nakamura A, Shichiri M, Ishida N, Kinugasa S, Morimoto Y, Niki E, Yoshida Y, Iwahashi H: Evaluation of acute oxidative stress induced by nio nanoparticles in vivo and in vitro. *J Occup Health* 2011, 53:64–74.
60. Zhang Y, Chen Y, Westerhoff P, Hristovski K, Crittenden JC: Stability of commercial metal oxide nanoparticles in water. *Water Res* 2008, 42:2204–2212.
61. King S, Hyunh K, Tannenbaum R: Kinetics of nucleation, growth, and stabilization of cobalt oxide nanoclusters. *J Phys Chem B* 2003, 107:12097–12104.
62. Baldi G, Bonacchi D, Franchini MC, Gentili D, Lorenzi G, Ricci A, Ravagli C: Synthesis and coating of cobalt ferrite nanoparticles: a first step toward the obtainment of new magnetic nanocarriers. *Langmuir* 2007, 23:4026–4028.
63. Min GK, Bevan MA, Prieve DC, Patterson GD: Light scattering characterization of polystyrene latex with and without adsorbed polymer. *Colloids Surf A* 2002, 202:9–21.
64. Koppel DE: Analysis of macromolecular polydispersity in intensity correlation spectroscopy: the method of cumulants. *J Chem Phys* 1972, 57:4814–4820.
65. Lim JK, Majetich SA, Tilton RD: Stabilization of superparamagnetic iron oxide-gold shell nanoparticles in high ionic strength media. *Langmuir* 2009, 25:13384–13393.
66. Zhang L, He R, Gu HC: Oleic acid coating on the monodisperse magnetite nanoparticles. *Appl Surf Sci* 2006, 253:2611–2617.
67. Wang Z, Wen XD, Hoffmann R, Son JS, Li R, Fang CC, Smilgies DM, Hyeon TH: Reconstructing a solid-solid phase transformation pathway in CdSe nanosheets with associated soft ligands. *Proc Natl Acad Sci USA* 2010, 107:17119–17124.
68. Gittings MR, Saville DA: The determination of hydrodynamic size and zeta potential from electrophoretic mobility and light scattering measurements. *Colloid Suface A: Physiochem Eng Aspects* 1998, 141:111–117.
69. Elimelech M, Gregory J, Jia X, Williams RA: *Particle Deposition and Aggregation: Measurement, Modeling and Simulation*. Stoneham: Butterworth-Heinemann; 1998.
70. Wiogo HTR, Lim M, Bulmus V, Yun J, Amal R: Stabilization of magnetic iron oxide nanoparticles in biological media by fetal bovine serum (FBS). *Langmuir* 2011, 27:843–850.
71. Donselaar LN, Philipse AP: Interactions between silica colloids with magnetite cores: diffusion sedimentation and light scattering. *J Colloid Interface Sci* 1999, 212:14–23.
72. Golas PL, Lowry GV, Matyjaszewski K, Tilton RD: Comparative study of polymeric stabilizers for magnetite nanoparticles using ATRP. *Langmuir* 2010, 26:16890–16900.
73. Phenrat T, Saleh N, Sirk K, Tilton RD, Lowry GV: Aggregation and sedimentation of aqueous nanoscale zerovalent iron dispersion. *Environ Sci Technol* 2007, 41:284–290.
74. Cuevas GDL, Faraudo J, Camacho J: Low-gradient magnetophoresis through field-induced reversible aggregation. *J Phys Chem C* 2008, 112:945–950.
75. Andreu JS, Camacho J, Faraudo J: Aggregation of superparamagnetic colloids in magnetic field: the quest for the equilibrium state. *Soft Matter* 2011, 7:2336–2339.
76. Ditsch A, Lindenmann S, Laibinis PE, Wang DIC, Hatton TA: High-gradient magnetic separation of magnetic nanoclusters. *Ind Eng Chem Res* 2005, 44:6824–6836.

77. Yeap SP, Toh PY, Ahmad AL, Low SC, Majetich SA, Lim JK: Colloidal stability and magnetophoresis of gold-coated iron oxide nanorods in biological media. *J Phys Chem C* 2012, 116:22561–22569.
78. Shen L, Stachowiak A, Fateen SEK, Laibinis PE, Hatton TA: Structure of alkanoic acid stabilized magnetic fluids. A small-angle neutron and light scattering analysis. *Langmuir* 2001, 17:288–299.
79. Lehner D, Lindner H, Glatter O: Determination of the translational and rotational diffusion coefficients of rodlike particles using depolarized dynamic light scattering. *Langmuir* 2000, 16:1689–1695.
80. Nath S, Kaittanis C, Ramachandran V, Dalal NS, Perez JM: Synthesis, magnetic characterization, and sensing applications of novel dextran-coated iron oxide nanorods. *Chem Mater* 2009, 21:1761–1767.
81. Lim JK, Tan DX, Lanni F, Tilton RD, Majetich SA: Optical imaging and magnetophoresis of nanorods. *J Magn Magn Mater* 2009, 321:1557–1562.
82. Broersma S: Rotational diffusion constant of a cylindrical particle. *J Chem Phys* 1960, 32:1626.
83. Broersma S: Viscous force and torque constants for a cylinder. *J Chem Phys* 1981, 74:6989.
84. Vasanthi R, Bhattacharyya S, Bagchi B: Anisotropic diffusion of spheroids in liquids: slow orientational relaxation of the oblates. *J Chem Phys* 2002, 116:1092.
85. Phalakornkul JK, Gast AP, Pecora R: Rotational and translational dynamics of rodlike polymers: a combined transient electric birefringence and dynamic light scattering study. *Macromolecules* 1999, 32:3122–3135.
86. Farrell D, Dennis CL, Lim JK, Majetich SA: Optical and electron microscopy studies of Schiller layer formation and structure. *J Colloid Interface Sci* 2009, 331:394–400.
87. Fang XL, Li Y, Chen C, Kuang Q, Gao XZ, Xie ZX, Xie SY, Huang RB, Zheng LS: pH-induced simultaneous synthesis and self-assembly of 3D layered β-FeOOH nanorods. *Langmuir* 2010, 26:2745–2750.

doi:10.1186/1556-276X-8-381
Cite this article as: Lim *et al.*: Characterization of magnetic nanoparticle by dynamic light scattering. *Nanoscale Research Letters* 2013 8:381.

Separation and Purification Technology 123 (2014) 171–174

Contents lists available at ScienceDirect

Separation and Purification Technology

journal homepage: www.elsevier.com/locate/seppur

Short Communication

Challenges associated to magnetic separation of nanomaterials at low field gradient

JitKang Lim [a,b,*], Swee Pin Yeap [a], Siew Chun Low [a]

[a] School of Chemical Engineering, Universiti Sains Malaysia, Nibong Tebal, Penang 14300, Malaysia
[b] Department of Physics, Carnegie Mellon University, Pittsburgh, PA 15213, USA

ARTICLE INFO

Article history:
Received 17 June 2013
Received in revised form 23 December 2013
Accepted 24 December 2013
Available online 8 January 2014

Keywords:
Magnetic separation
Magnetic nanoparticles
Low gradient magnetophoresis
Water remediation
Environmental engineering

ABSTRACT

Magnetic nanoparticles (MNPs) have been proposed as one of the effective tools for pollutant removal from aqueous environment. In most of the new strategies investigated, which involved the use of MNPs, the ability to reharvest back this nanomaterial by an externally applied magnetic field is always being emphasized. In this short communication, we discuss the challenges associated to the magnetic separation of MNPs from its suspending media through magnetophoresis under low magnetic field gradient. We highlight the major constraints, such as thermal energy, Stokes drag and gravitational pulling, which influence the successful separation of MNPs from aqueous environment by low gradient magnetic separation (LGMS). Dimensionless numbers are introduced to provide a more quantitative comparison between the aforementioned constraints with magnetophoresis at low field gradient. Finally, we focus our discussion on the role of (1) guided/self-assembly approaches and (2) on-site LGMS strategy as the most practical routes of using MNP for water remediation.

1. Introduction

In last decade, we have observed a booming of research findings on the huge potential of magnetic nanoparticles (MNPs) in removing dangerous pollutants, such as arsenic [1], heavy metals [2], chlorinated compounds [3], and also organic dyes [4] from water resources. One of the great advantages of this MNP based water treatment technique is the recollection ability of MNPs, which can be easily achieved by using a hand held permanent magnet [1,4], after the hazardous compound was adsorbed onto the particle surfaces. The underlying principle behind this separation technique is remarkably straightforward. It relies on the simple fact that the magnetic materials experience magnetophoretic force in the presence of magnetic field gradients and thus these materials can be physically separated out from the surrounding fluids by a magnetic source. In addition, MNPs can also be employed to impart a magnetic dipole moment to biological cells, through immobilization on the cell surfaces, which subsequently leading to magnetophoretic separation of biological substances [5].

The rapid magnetophoretic separation of MNPs under low magnetic field gradient ($\nabla B < 100$ Tesla/m), as observed by others is very likely through field-induced reversible aggregation of particles [6]. Under this scenario, the particle clusters formed would migrate to the region where the magnetic field gradient is the highest. Along its migration pathway, the moving MNP clusters collide with each other and integrated into larger aggregates with higher magnetophoretic velocity [6,7]. This mechanism is the key factor for successful separation of MNPs in real time and revealed the opportunity for the implementation of low gradient magnetic separation (LGMS) for engineering applications.

In contrast to conventional industry practice in which high gradient magnetic separation (HGMS) is normally being employed, the design rules for LGMS is ill-defined and poorly understood. Moreover, the key parameters involved for implementation of LGMS in water treatment technology are also not being fully explored yet. Recently, Mandel and Hutter have briefly discussed the problems related to MNPs separation [8]. They raised an interesting point in which the use of ferrofluid as a nanoemulsion provides better alternative for water treatment purpose compared to easily agglomerated MNP suspension. However, the liquid–liquid interface between the nanoemulsion and the aqueous media can be the major barrier toward the full realization of this noble idea. Nevertheless, the key question here is how the nanosized magnetic particles can be used effectively for water treatment, and more importantly, the recollection of these particles from their suspension. It is the purpose of this paper to illustrate some general rule of thumbs related to the separation of MNPs under low field gradient.

* Corresponding author at: School of Chemical Engineering, Engineering Campus, Universiti Sains Malaysia, Seri Ampangan, Nibong Tebal, Penang 14300, Malaysia. Tel.: +60 4 599 6423; fax: +60 4 599 1013.
E-mail address: chjitkangl@eng.usm.my (J. Lim).

1383-5866/$ - see front matter © 2014 Elsevier B.V. All rights reserved.
http://dx.doi.org/10.1016/j.seppur.2013.12.038

2. Underlying problems associated to LGMS

It is often being illustrated that by introduction of a magnetic field, the separation of MNPs from aqueous environment can be made possible in real time as shown in Fig. 1. Even though, the separation time involved is very feasible for practical usages at lab scale, the possibility for this kind of setup to be fully implemented for water treatment purposes is as good as none. By taking the example of a cylindrical NdFeB magnet, the magnetic field B_x along its symmetry axis as a function of the distance x away from the magnet pole face can be estimated quite accurately by following equation [9]:

$$B_x = \frac{B_r}{2}\left[\frac{x+L}{\sqrt{(L+x)^2+R^2}} - \frac{x}{\sqrt{x^2+R^2}}\right] \quad (1)$$

where R is the radius of the cylinder, L is the length of the cylinder, B_r is the remanence or residual induction of the magnetic material. For a grade N50 NdFeB, B_r is about 1.45 Tesla. This calculated B_x has a very good match with experimentally measured results [10] and for the permanent magnet shown in Fig. 1, with a dimension of $R = 0.7$ cm and $L = 1.5$ cm, its magnetic field B_x decay rapidly from the magnet pole face (Fig. 2). Once, the MNPs has been released into environment for water treatment purposes, there is no such magnet or magnetic separation devices/strategies can be employed to cope with the length scale involved, up to kilometers, in re-harvesting them back. For an example, according to Eq. (1), in order to generate an appropriate field gradient to achieve LGMS at separation distance of 1 km ($x = 1000$ m) would require a cylindrical NdFeB magnet (at the same aspect ratio of the magnet shown in Fig. 1) with radius of 140 m and length of 300 m.

This analogy bring out an important message in which for any in situ water treatment technology that involved the usages of MNPs, it is misleading to emphasize on its magnetic separation. Once being released into the environment there is no way for MNPs to be re-harvested back, at least not by magnetic separation. Thus, it is more appropriate for the implementation of MNPs under the setting of a on-site treatment facility. Under this context, the application of LGMS as a downstream separation unit can be both economical and technological feasible [5]. For engineering application, the (a) inhomogeneous field gradient and (b) complex distribution of magnetic field lines in three dimensional space of a permanent magnet can be extremely challenging to be properly integrated into a LGMS system.

3. Transport behaviors of MNPs due to "nanosize effects"

By taking non-interacting particles assumption, at magnetic field B, the magnetophoretic force F_{mag} needed to induce separation of spherical MNPs is [11,12]:

$$F_{mag} = \frac{4}{3}\pi r_{pt}^3 (M \cdot \nabla)B \quad (2)$$

where r_{pt} and M are the radius and the magnetization (per unit volume) of the MNP, respectively. By equating the F_{mag} with viscous drag force ($F_{drag} = 6\pi\eta r_{pt} \cdot u_{mag}$) experienced by a sphere [13], the magnetophoretic velocity u_{mag} can be calculated as

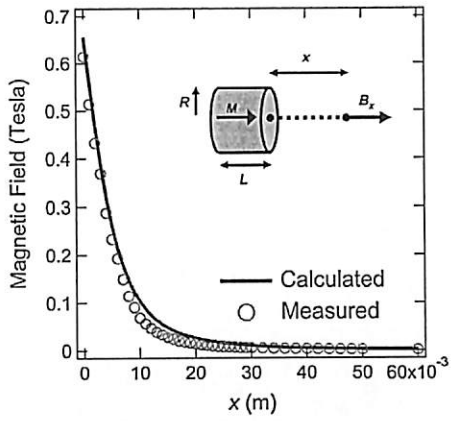

Fig. 2. Magnetic field B_x extended out from a cylindrical NdFeB magnet with radius of 0.07 m and length of 0.015 m. B_x is calculated by using Eq. (1).

$$u_{mag} = \frac{2r_{pt}^2}{9\eta}(M \cdot \nabla)B \quad (3)$$

where η is the viscosity of the suspending medium. For the case of very weak magnetic field, Eq. (2) can be further simplified to [14]:

$$F_{mag} = \frac{\Delta\chi V_p}{\mu_0}(\nabla B)B \quad (4)$$

where μ_0 is the vacuum permeability, V_p is the particle volume ($V_p = 4\pi r_{pt}^3/3$) and $\Delta\chi$ is the different in magnetic susceptibility between the particle and the fluid. Eq. (4) raised an interesting observation, in which the F_{mag} experienced by a nanoparticle is not only dependent on the magnetic field and field gradient but the volume of the MNP involved is equally important. For any design purposes which involved transport behaviors of MNP, knowing the value of u_{mag} is vital as various transport phenomena analyses can be performed [15].

Since the particle size is in nanometer range, its motion is heavily influenced by thermal energy and viscous drag; hence, conventional dimensionless number analysis can be very helpful to characterize the flow behavior. Table 1 summarized some of the useful dimensionless numbers which are familiar to the chemical and mechanical engineers and can serve as an effective way to rationalize the transport behavior of MNPs under magnetophoresis. By using the value of B and ∇B as shown in Fig. 2 and hydrodynamic radius of the MNPs (Fig. 1) at 150 nm as determined by dynamic light scattering (DLS), the Reynolds (Re), Péclet (Pe) and Froude (Fr) numbers with respect to the separation distance x from the pole surface of NdFeB magnet can be calculated (see Fig. 3a). Here we used the mathematical equations presented in Table 1 for the calculation of each dimensionless number and according to Eq. (3) the MNPs would typically having a magnetophoretic velocity within the range of 0.5 μm/s to around 9000 μm/s. As

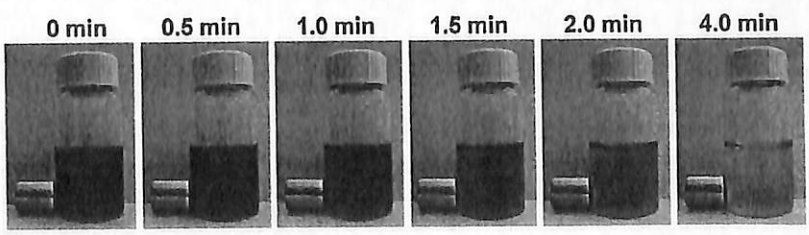

Fig. 1. Magnetophoretic collection of iron oxide MNPs with ~150 nm hydrodynamic radius in real time.

Table 1
Useful dimensionless number for characterization of MNP flow behaviors under magnetophoresis.

Dimensionless number	Equation[a]	Physical interpretation
Reynolds number, *Re*	$Re = \frac{\rho u_{mag} l}{\eta}$	*Re* defined the ratio of inertia to viscous force, as $Re \gg 1$, magnetophoresis dominated $Re \ll 1$, viscosity dominated
Péclet number, *Pe*	$Pe = \frac{u_{mag} l}{D}$	*Pe* defined the ratio of inertia to diffusion, as $Pe \gg 1$, magnetophoresis dominated $Pe \ll 1$, diffusion dominated
Froude number, *Fr*	$Fr = \frac{u_{mag}^2}{gl}$	*Fr* defined the ratio of inertia to gravitational pulling $Fr \gg 1$, magnetophoresis dominated $Fr \ll 1$, gravitational pulling dominated

[a] where l is the associated characteristic length scale, and for magnetophoresis study is concerned, it is typically taking as the diameter of MNP, ρ is the density of MNP and here we assumed it is purely magnetite with density of 5.2 g/cm^3, D is the diffusivity of MNP and can be calculated by using Stokes–Einstein equation, and g is the acceleration due to gravity.

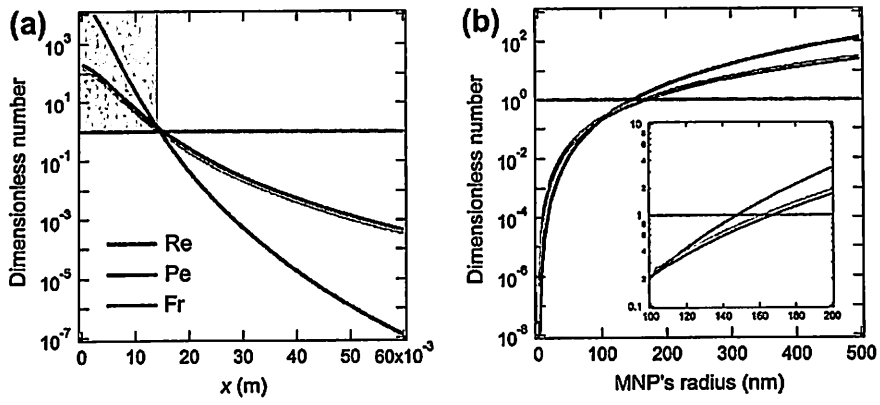

Fig. 3. Reynolds (*Re*), Péclet (*Pe*) and Froude (*Fr*) numbers calculated at (a) separation distance *x* from surface of a cylindrical NdFeB with varying *B* and ∇*B* values as shown in Fig. 2 and (b) different radius of MNPs at $B = 0.049$ Tesla and $\nabla B = 6.62$ Tesla/m. Broken line indicate the dimensionless number at one, so, above this point the magnetophoretic flow of the MNP dominates viscous drag, thermal randomization and also gravitational pulling.

clearly depicted in Fig. 3a, under this setup there presents a critical distance at around $x = 15$ mm in which magnetophoresis of a spherical MNP dominates other disturbances, such as Brownian motion, viscous drag and gravitational pulling. Below this separation distance, all three calculated dimensionless numbers are greater than unity. The shaded area above the broken line in Fig. 3a defines the effective operation region where the magnetophoretic collection could occur deterministically. In fact, this is the same area in which magnetic field *B* decayed drastically with respect to the separation distance *x* as shown in Fig. 2. The averaged magnetic field gradient ∇*B* within this zone at around 54.67 Tesla/m certified the nature of this process as LGMS. Detailed spatial resolution revealed by this dimensionless number analysis provides useful information for the design of LGMS system.

In general, the migration of MNPs under LGMS as shown in Fig. 1 is a complex interplay between magnetophoresis, viscous drag and random Brownian motion in which all these phenomena scale differently with the particle size. By taking $B = 0.049$ Tesla and $\nabla B = 6.62$ Tesla/m at critical separation distance of 15 mm, the Reynolds (*Re*), Péclet (*Pe*) and Froude (*Fr*) numbers can be calculated (see Fig. 3b) for MNPs with different radius. For magnetophoresis to play a dominant role, by having all three dimensionless numbers to be greater than one, MNP with radius between 140 nm and 180 nm is required. By taking the superparamagnetic size limit of magnetite (Fe_3O_4) particles at around $r = 17.5$ nm [16] gives dimensionless number of $Re = 0.0013$, $Pe = 0.0002$ and $Fr = 0.0011$, respectively. These very low values of *Re*, *Pe* and *Fr* numbers implied that the magnetophoretic motion of the MNP at this size would be overwhelmed by viscous drag, thermal energy and also gravitational pulling. This examination is contradicting with the surprised results as observed by Yavuz and coworkers [1]. In directly, it has suggested the cooperative nature of the magnetophoresis and can also be generalized to our observation in Fig. 1.

At very high concentration in which the non-interacting particles assumption is not longer valid and magnetophoresis become concentration dependent [6], Eq. (3) alone is not suffice to estimate u_{mag} accurately. Under this scenario, a more sophisticated mathematic analysis such as the one suggested by Faraudo and Camacho is needed to estimate the separation time by taking into account the field induced aggregation of MNPs during the magnetophoresis [6,17]. For cooperative magnetophoresis, it is estimated that the recorded velocity can be 65 times higher than those predicted by conventional method [18]. Nevertheless, the dimensionless number analysis is still an easy route to provide quick feedback for checking the relation among important physical properties relevant to magnetophoresis of MNPs under LGMS as long as the u_{mag} can be estimated reasonably. More importantly, it also gives a useful approach to rationalize the complex interplay between the magnetophoresis with thermal energy, Stokes drag and gravitational pulling that eventually dictates the success or failure of LGMS in harvesting MNPs.

4. MNPs for engineering applications

For environmental engineering applications are concerned, MNP is typically being surface functionalized by macromolecules. This step is taken to mitigate the nanotoxicity associated to its small dimension [19], and to maintain its colloidal stability in

suspension [20]. However, just recently our group has revealed the conflicting role of colloidal stability in suppressing the magnetophoretic separation of MNPs [21,22]. After achieved good dispersibility, the polyelectrolyte coated iron oxide MNP become extremely difficult to be magnetophoretically separated out from its suspension even with the introduction of very high magnetic field gradient $\nabla B > 1000$ Tesla/m [22]. This in turn would suppress the cooperative effect as discussed in previous section and also prevent the chaining of MNPs that ultimately contribute to the rapid magnetophoresis [6]. The huge time lag and low efficiency observed might posed a serious challenge for the effective use of surface functionalized MNPs in any applications that required rapid separation.

It is obvious that MNPs cannot be a standalone nanoagent for most of the water treatment technology that required good colloidal stability and achieving rapid magnetophoretic separation while maintaining its other important properties, such as high specific surface area, catalytic activity, low nanotoxicity and etc. We anticipated that MNPs need to be combined with other components to fully realize its potential for water treatment applications. The integration of MNPs into polymeric microcapsule can be a feasible solution [23,24]. Other guided/self-assembly approaches, such as magnetoliposomes [25], pickering emulsion [26], templated-structure like silica-MNPs and activated carbon-MNPs [27,28], can also be a viable option. For the development of next generation MNP-enhanced nanomaterials for water treatment applications, the synthesis proceduce employed should be cost effective, environmental friendly and can produce large amount of nanomaterials within reasonable time frame. In addition, the magnetophoretic property should also be emphasized. This feature is necessary to ensure full recovery of the MNPs from treated water.

5. Conclusion

A more localized usages of MNP for water treatment purpose, such as in an on-site treatment facility, should be implemented in order to take full advantage of its magnetophoretic property. The idea of releasing enormous amount of MNPs into environment for water treatment purpose and magnetophoretically re-collecting this nanomaterial back is highly unrealistic. Cooperative phenomenon during the MNP magnetophoresis has greatly complicated the mathematical analysis on predicting the MNP velocity. In addition, the contribution of colloidal stability of MNPs toward LGMS is critical and should not be overlooked in any engineering applications. Dimensionless number calculation provides a fast and reliable analysis on the flow behavior of the MNPs under magnetophoresis. This analysis also related important physical properties associated to the magnetophoresis of MNPs under low field gradient. There are still many interesting opening questions related to magnetophoresis of MNPs [29]. More research efforts are needed in developing a practicable guided/self-assembly approach and efficient LGMS process for full utilization of MNPs in environmental engineering applications.

Acknowledgements

This material is based on the work supported by Research University (RU) (Grant No. 1001/PJKIMIA/811219) from Universiti Sains Malaysia (USM), Exploratory Research Grants Scheme (ERGS) (Grant No. 203/PJKIMIA/6730013) from the Ministry of Higher Education of Malaysia, and eScience Fund (Grant No. 205/PJKIMIA/6013412) from MOSTI Malaysia. JKL and SWL are affiliated to the Membrane Science and Technology Cluster of USM. JK Lim thanks Lee R. More and Maciej Zborowski from Cleveland Clinic and Sara A. Majetich from Carnegie Mellon University for discussion related to Fig. 2.

References

[1] C.T. Yavuz, J.T. Mayo, W.W. Yu, A. Prakash, J.C. Falkner, S. Yean, L. Cong, H.J. Shipley, A. Kan, M. Tomson, D. Natelson, V.L. Colvin, Low-field magnetic separation of monodisperse Fe_3O_4 nanocrystals, Science 314 (2006) 964–967.
[2] W. Yantasee, C.L. Warner, T. Sangvanich, R.S. Addleman, T.G. Carter, R.J. Wiacek, G.E. Fryxell, C. Timchalk, M.G. Warner, Removal of heavy metals from aqueous systems with thiol functionalized superparamagnetic nanoparticles, Environ. Sci. Technol. 41 (2007) 5114–5119.
[3] Y. Liu, T. Phenrat, G.V. Lowry, Effect of TCE concentration and dissolved groundwater solutes on NZVI-promoted TCE dechlorination and H_2 evolution, Environ. Sci. Technol. 41 (2007) 7881–7887.
[4] B. Saha, S. Das, J. Saikia, G. Das, Preferential and enhanced adsorption of different dyes on iron oxide nanoparticles: a comparative study, J. Phys. Chem. C. 115 (2001) 8024–8033.
[5] P.Y. Toh, S.P. Yeap, L.P. Kong, B.W. Ng, C.J.C. Derek, A.L. Ahmad, J.K. Lim, Magnetophoretic removal of microalgae from fishpond water: feasibility of high gradient and low gradient magnetic separation, Chem. Eng. J. 211–212 (2012) 22–30.
[6] G. Cuevas, J. Faraudo, J. Camacho, Low-gradient magnetophoresis through field-induced reversible aggregation, J. Phys. Chem. C. 112 (2008) 945–950.
[7] M. Benelmekki, C. Caparros, A. Montras, R. Goncalves, S. Lanceros-Mendez, L.I.M. Martinez, Horizontal low gradient magnetophoresis behavior of iron oxide nanoclusters at the different steps of the synthesis route, J. Nanopart. Res. 13 (2011) 3199–3206.
[8] K. Mandel, F. Hutter, The magnetic nanoparticle separation problem, Nano Today 7 (2012) 485–487.
[9] V. Schaller, U. Kräling, C. Rusu, K. Petersson, J. Wipenmyr, A. Krozer, G. Wahnström, A. Sanz-Velasco, P. Enoksson, C. Johansson, Motion of nanometer sized magnetic particles in a magnetic field gradient, J. Appl. Phys. 104 (2008) 093918.
[10] J.K. Lim, C.J.C. Derek, S.A. Jalak, P.Y. Toh, N.H.M. Yasin, B.W. Ng, A.L. Ahmad, Rapid magnetophoretic separation of microalgae, Small 8 (2012) 1683–1692.
[11] G.D. Moeser, K.A. Roach, W.H. Green, T.A. Hatton, P.E. Laibinis, High-gradient magnetic separation of coated Magnetic nanoparticles, AIChE J. 50 (2004) 2835–2848.
[12] G.P. Hatch, R.E. Stelter, Magnetic design considerations for devices and particles used for biological high-gradient magnetic separation (HGMS) systems, J. Magn. Magn. Mater. 225 (2001) 262–276.
[13] M. Zborowski, L. Sun, L.R. Moore, P.S. Williams, J.J. Chalmers, Continuous cell separation using novel magnetic quadrupole flow sorter, J. Magn. Magn. Mater. 194 (1999) 224–230.
[14] N. Pamme, A. Manz, On-chip free-flow magnetophoresis: continuous-flow separation of magnetic particles and agglomerates, Anal. Chem. 76 (2004) 7250–7256.
[15] J.K. Lim, D.X. Tan, F. Lanni, R.D. Tilton, S.A. Majetich, Optical imaging and magnetophoresis of nanorods, J. Magn. Magn. Mater. 321 (2009) 1557–1562.
[16] D.J. Dunlop, Magnetite: behavior near the single-domain threshold, Science 176 (1972) 41–43.
[17] J. Faraudo, J. Camacho, Cooperative magnetophoresis of superparamagnetic colloids: theoretical aspects, Colloid Polym. Sci. 288 (2010) 207–215.
[18] J.S. Andreu, J. Camacho, J. Faraudo, M. Benelmekki, C. Rebollo, L.I.M. Martínez, Simple analytical model for the magnetophoretic separation of superparamagnetic dispersions in a uniform magnetic gradient, Phys. Rev. E 84 (2011) 021402.
[19] A. Verma, F. Stellacci, Effect of surface properties of nanoparticle–cell interactions, Small 6 (2010) 12–21.
[20] P.L. Golas, S. Louie, G.V. Lowry, K. Matyjazsewski, R.D. Tilton, Comparative study of polymeric stabilizers for magnetite nanoparticles using ATRP, Langmuir 26 (2010) 16890–16900.
[21] S.P. Yeap, P.Y. Toh, A.L. Ahmad, S.C. Low, S.A. Majetich, J.K. Lim, Colloidal stability and magnetophoresis of gold-coated iron oxide nanorods in biological media, J. Phys. Chem. C. 116 (2012) 22561–22569.
[22] S.P. Yeap, A.L. Ahmad, B.S. Ooi, J.K. Lim, Electrosteric stabilization and its role in cooperative magnetophoresis of colloidal magnetic nanoparticles, Langmuir 28 (2012) 14878–14891.
[23] A.F. Ngomsik, A. Bee, J.M. Siaugue, V. Cabuil, G. Cote, Nickel adsorption by magnetic alginate microcapsules containing an extractant, Water Res. 40 (2006) 1848–1856.
[24] L.P. Kong, X.J. Gan, A.L. Ahmad, B.H. Hameed, E.R. Evarts, B.S. Ooi, J.K. Lim, Design and synthesis of magnetic nanoparticles augmented microcapsule with catalytic and magnetic bifunctionalities for dye removal, Chem. Eng. J. 197 (2012) 350–358.
[25] M. Gonzales, K.M. Krishnan, Synthesis of magnetoliposomes with monodisperse iron oxide nanocrystal cores for hyperthermia, J. Magn. Magn. Mater. 293 (2005) 265–270.
[26] A. Kaiser, T. Liu, W. Richtering, A.M. Schmidt, Magnetic capsules and pickering emulsions stabilized by core-shell particles, Langmuir 25 (2009) 7335–7341.
[27] W. Zhao, J. Gu, L. Zhang, H. Chen, J. Shi, Fabrication of uniform magnetic nanocomposite spheres with a magnetic core/mesoporous silica shell structure, J. Am. Chem. Soc. 127 (2005) 8916–8917.
[28] M. Schwickardi, S. Olejnik, E.L. Salabas, W. Schmidt, F. Schüth, Scalable synthesis of activated carbon with superparamagnetic properties, Chem. Commun. (2006) 3987–3989.
[29] J. Faraudo, J.S. Andreu, J. Camacho, Understanding diluted dispersion of superparamagnetic particles under strong magnetic fields: a review of concepts, theory and simulation, Soft Matter 9 (2013) 6654–6664.

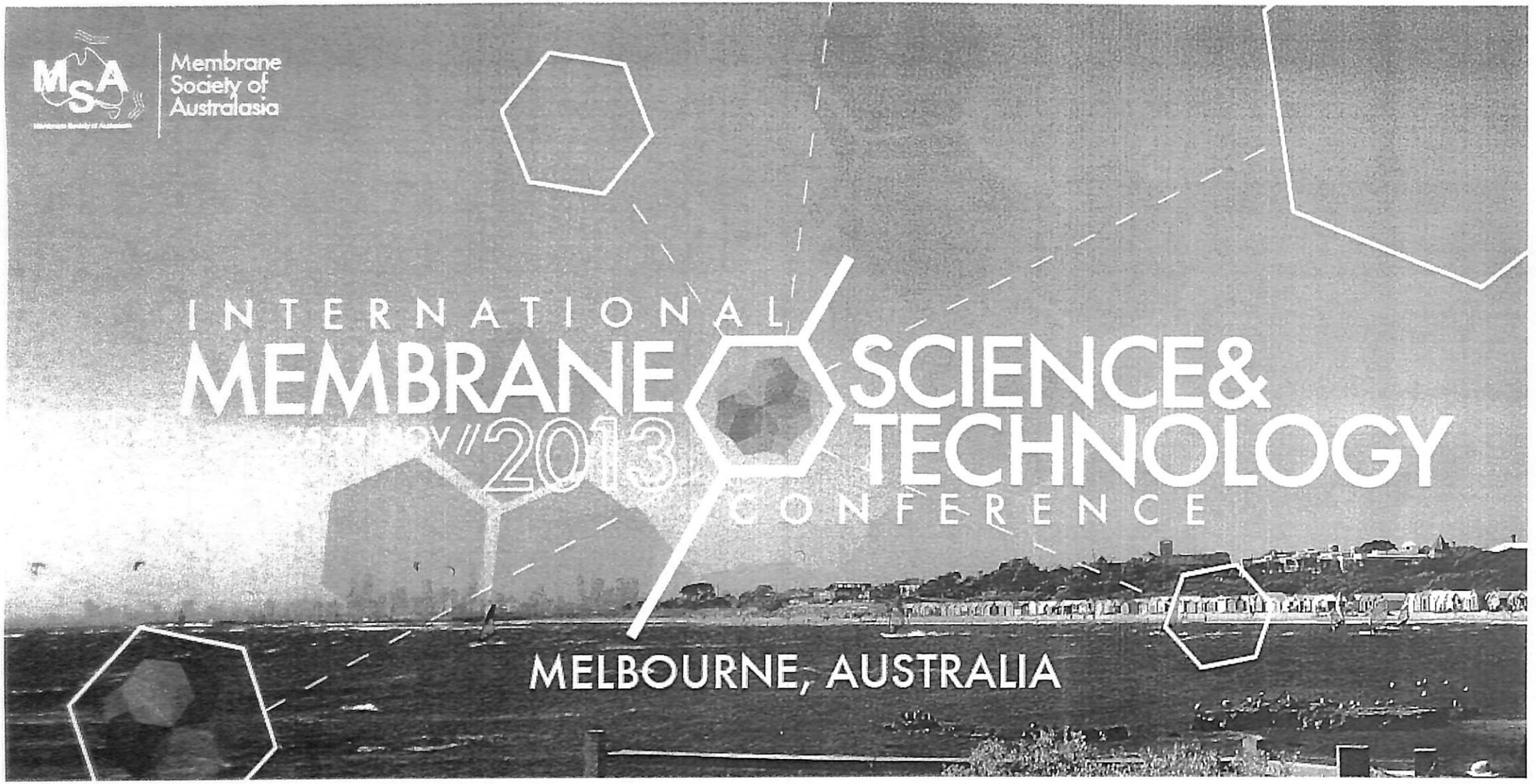
MSA
Membrane
Society of
Australasia
INTERNATIONAL
MEMBRANE
SCIENCE&
TECHNOLOGY
CONFERENCE
2013
MELBOURNE, AUSTRALIA

Evaluation of Film Structure and Adsorption Kinetics of Magnetically Responsive PES Membrane for Potent Antifouling Behaviour

Q. H. Ng[1], J. K. Lim[1], B. S. Ooi, A. L. Ahmad[1], S. C. Low*[1]

[1]*School of Chemical Engineering Campus, UniversitiSains Malaysia, Seri Ampangan, 14300 NibongTebal S.P.S. Penang, Malaysia,* chsclow@eng.usm.my

This study presenting surface forces and macromolecular properties of magnetically responsive polyethersulfone (PES) membranes in relate to their potent antifouling behaviour. The functionalized superparamagnetic iron oxide (Fe_3O_4) nanoparticles were end-capped to the surface of PES membrane, to provide magneto-induced rotation motions of the magnetic nano-colloids in 3-dimensional space, with the help of an external magnetic field (magnetic rod). In the present work, alternate adsorption of polymers, poly(sodium 4-styrene sulfonate) (PSS) and/or polycation poly(diallyldimethylammonium chloride) (PDDA) to the surface of PES ultrafiltration membrane is carried out by a layer-by-layer self-assembly method and then end-capped with the functionalized magnetite nanoparticles. By used of a quartz crystal microbalance with dissipation (QCM-D), we investigated the structural properties and adsorption kinetics of multilayers which composed of different polyelectrolyte pairs that deposited to the surface of PES coated gold crystal cells. The combined measurement of shifts in frequency (Δf) and changes in the dissipation factor (ΔD) provides information about the viscoelastic properties of the adsorbed adlayers and the surrounding bulk liquid environment. The frequency change (Δf) results demonstrated that the exponential growth trend of Fe_3O_4 nanoparticles on PES polymer gradually becomes dominant with the sequential deposition of polyelectrolyte PSS and PDDA. Meanwhile, the observed changes in dissipation factor (ΔD) indicated the adherence of the multilayer polymers (PSS, PDDA and Fe_3O_4) to the surface of PES is comprises of a large degree of motional freedom. Atomic force microscopy (AFM) and field emission scanning electron microscopy (FESEM) measurements pointed out the roughness and surface morphology of the multilayers, which may be controlled by the assembly conditions that modify the layer structures and subsequently the polyelectrolyte chain conformation. Furthermore, present study demonstrated that such magnetically responsive nano-composite membrane could significantly improved the flux and rejection performances based upon the rotational motions of the magnetic nano-colloid under an oscillating external magnetic field, which in turn reduces the fouling by colloids presented in aqueous feed.

Key Words: QCM-D, membrane fouling; magnetophoretic actuation; water treatment

MST 2013

11TH INTERNATIONAL CONFERENCE ON MEMBRANE SCIENCE AND TECHNOLOGY

Abstract Book

SERI PACIFIC HOTEL, KUALA LUMPUR

27-29TH AUGUST 2013

AMTEC Advanced Membrane Technology Research Centre

:ORGANIZED BY:

UTM UNIVERSITI TEKNOLOGI MALAYSIA

IN COLLABORATION WITH

Universiti Kebangsaan Malaysia

USM Universiti Sains Malaysia

NUS National University of Singapore

Nanyang Technological University

Conference on Membrane Science and Technology 2013 (MST 2013)

Studying the role of magnetite (Fe_3O_4) colloids functionality on PES membrane in removing of humic acid foulant using QCM-D

Q. H. Ng,[a] J. K. Lim,[a] A. L. Ahmad,[a] B. S. Ooi,[a] S. C. Low [a,*]

[a] *School of Chemical Engineering Campus, UniversitiSains Malaysia, Seri Ampangan, 14300 NibongTebal S.P.S. Penang, Malaysia*

*Corresponding author: *chsclow@eng.usm.my*, *Tel: +6-04-5996412, Fax: +6-04-5941013*

Graphical abstract

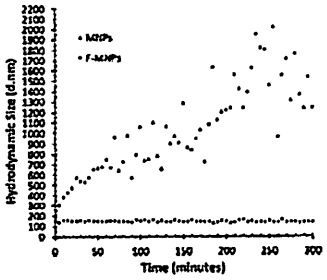

Abstract

Membrane fouling remains as one of the most critical issues in water and wastewater treatment. Organic foulant such as humic acid substances contribute to the irreversible fouling and flux decline in membrane separation processes. To reduce the membrane fouling potential, the present work explored the end-capped of the functionalized nanostructured magnetite (Fe_3O_4) colloids with poly(sodium 4-styrene sulfonate) (PSS) onto the surface of polyethersulfone (PES) membrane. Multilayer modification method using polyelectrolytes PSS and poly(diallyldimethylammonium chloride) (PDDA) were served as the intermediate precursor towards the end-capped of the Fe_3O_4 to the PES polymer. By using quartz crystal microbalance with dissipation (QCM-D), we investigated the structural properties and adsorption kinetics of the multilayers, comprising of the polyelectrolyte layers and the end-capped Fe_3O_4 which onto the crystal surface with a thin layer of PES polymer as the model membrane. By monitoring the frequencies and dissipation shifts of QCM-D, the results has demonstrated the exponential growth trend for the Fe_3O_4 that dispersed in ultrapure water, which has confirmed the better end-capped ability of the nanoparticles onto the PES polymer. In addition, the foulant analysis of the modified (PES- Fe_3O_4) and unmodified (PES) membranes were also being investigated using QCM-D through the adsorption study and the cleaning of the humic acid from the PES polymer. Result shows that Fe_3O_4 has increased the hydrophilicity and drastically changed the membrane surface morphology, hence promoting the detachment of the humic acid.

Keywords: Surface functionalization; QCM-D, Membrane Fouling; Water Treatment.

1.0 INTRODUCTION

Over the past few decades, the usage of membrane for potable water production has progressed remarkable due to the compact design of the membrane module, lower energy consumption, and reliable effluent quality. However, membrane fouling still remains as a critical issue in many applications of water filtration processes that restricts the widespread application of membranes. In water treatment, humic acid (HA) has been considered to be one of the most significant foulants among many potential natural organic matter (NOM) in both surface and ground water (1, 2). Previous studies of HA fouling were focused on the role of several important factors in humic acid solutions (2, 3). For an example, the membrane fouling increases with the decreasing of pH or increasing of ionic strength of HA solution (2, 3), as observed in many studies dealing with various types of membranes. However, this kind of research approach is labor intensive, and normally requires tedious analysis for the feed stream before the filtration process.

In general, hydrophilic membranes exhibit lower level of fouling and increased flux reversibility at their surfaces (3, 4). Many approaches have been taken to improve the hydrophilicity of membranes, including the blending of the hydrophilic polymers and the surface modification of membrane (5-7). However, the polymer chain undergoing chemical modification sometimes becomes highly swollen, leading to the low membrane's mechanical properties (8). As solution, the integration of nanoparticles into the membrane matrix allows both control of the membrane fouling and the ability to produce specific functionalities to the membrane (9, 10). Generally, this composite membrane can be produced through polyelectrolyte multilayer modification (PEM) method, phase inversion techniques, self-assembly through covalent attachment or blending with a polymer casting solution (11-13).

The Quartz Crystal Microbalance with Dissipation monitoring (QCM-D) technology is a surface sensitive technique which gives real time information about the deposition of the thin surface layers by measuring the changes of mass and viscoelastic properties at a surface. It has been used to evaluate the surface adsorption kinetic and offers the opportunity to analysis the nanoparticle-surface interactions in real time (14, 15). Serious of reports have presented the membrane fouling using QCM-D technique and proved its effectiveness in assessing the adsorption and viscoelastic properties of the foulants (organic and inorganic) onto the membrane surfaces (16-18).

In present study, we aimed to quantify the adsorption of F-MNPs onto the PES membrane surfaces in different dispersants (DI water and PSS) at condition with or without PSS and PDDA as precursors through QCM-D measurement. First, the MNPs were functionalized using PSS polymer and flocculation studies for the nano-colloids were carried out. Then, different membrane surfaces functionalities in adsorptive fouling by common organic foulants (HA) were elucidated.

2.0 EXPERIMENTAL

2.1 Materials

The magnetite Fe_3O_4 was supplied by NanoAmor (USA). PSS and PDDA polyelectrolyte were purchased from Sigma (St. Louis, USA). Ultrafiltration PES membrane with molecular weight cut-off 20,000 was obtained from GE Osmonics (USA). In this study, PES polymer supplied by BASF was used as the model membrane using in QCM-D measurement. The solvent N-methyl-2-pyrrolidone (NMP) and humic acid used as the membrane foulant were purchased from Merck (Germany) and Aldrich (Switzerland), respectively. NaOH (Merck, Germany) and HCl were used for pH adjustment.

2.2 Functionalization of nanoparticles

A suspension with 2500ppm of Fe_3O_4 was prepared using deionized water and ultrasonicated to break the existing aggregates. Similarly, PSS solution (0.00412 g/mL) were prepared and ultrasonicated to promote good dispersity of polymeric solution. Both colloids suspension and PSS solution were adjusted to pH 3.5 before the former was added drop wise into the latter solution, where the physisorption process was allowed to occur for 1 day. The PSS-coated nanoparticles (F-MNPs) were then separated using a permanent magnet and pre-washed before final dispersion in deionized water or PSS. Dynamic light scattering (Zetasized) was used to determine the size distribution and colloidal stability of naked Fe_3O_4 and functionalized Fe_3O_4 in suspension. The measurement was performed at an angle of 90° under a light source of 650 nm, and the calculation was based on the assumption of spherical particles in Brownian motion and single scattering.

2.3 Quartz Crystal Microbalance with Dissipation (QCM-D)

The QCM-D measurements were performed with AT-cut quartz crystals mounted in an E1 system (Q-sense, Goteborg, Sweden). 1 % w/v of PES polymer dissolved in NMP was spin coated onto the gold quartz crystal (Q-sense, Sweden) and evaporated at room temperature for 24 hours. All QCM-D measurements were conducted under flow-through condition via a digital peristaltic pump operating in sucking mode at a constant flow rate 50 $\frac{\mu L}{min}$ and at 25°C. The ATR-FTIR spectra of the commercial PES membrane and the model PES membrane coated on the quartz crystal were analyzed using Thermo Scientific Fourier transform infrared spectrometer (NICOLET iS10, USA) to confirm the similarly of the functional groups. Each spectrum was obtained from 32 scans with 4 cm^{-1} resolutions at a 45° incident angle using a diamond crystal over the wavenumber range of 4000-600 cm^{-1}.

2.3.1 Monitoring F-MNPs adsorption

The dynamic adsorptions of F-MNPs onto the PES surface in condition with or without precursors (PSS/PDDA) as well as the effects of dispersants (DI water/PSS) were monitored using QCM-D, as the experimental protocols were shown in Table 1. Adsorbed mass of F-MNPs on difference combination surface were modeled using the viscoelastic modeling in QTools provided by Q-Sense.

Table 1 List of the different samples combination

No. Sample	Precursor	Dispersant of F-MNPs
1	-	Ultrapure water
2	-	PSS
3	PDDA	Ultrapure water
4	PDDA	PSS
5	PSS then PDDA	Ultrapure water
6	PSS then PDDA	PSS

2.3.2 Monitoring of HA adsorption/cleaning of adsorbed HA on membranes surface

The foulant (HA) analysis of the modified (PES- Fe_3O_4) and unmodified (PES) membranes were investigated using QCM-D through the adsorption study and cleaning of the humic acid from the membranes. After a stable baseline of the QCM-D signal was achieved while flowing with ultrapure water, HA foulants (25ppm) were allowed to flow across the quartz crystal surface for two hours, followed by washing using ultrapure water for another 30 min. The adsorbed mass (Δm) as well as the removed cleaning mass per unit surface of HA from the difference quartz crystal surfaces (modified PES-Fe_3O_4 and unmodified PES model membranes) were evaluated based on the Sauerbrey equation (19):

$$\Delta f = -\frac{n}{C}\Delta m \qquad \text{(Eq. 1)}$$

where n is overtone number (n=3 in this study) and C is the mass sensitivity constant of the QCM-D (C=17.7 ng*cm^{-2}*Hz^{-1} at f=4.95 MHz).

■3.0 RESULTS AND DISCUSSION

3.1 Stability of the functionalized MNPs and characteristics of the model PES membrane

Dynamic Light scattering (DLS) was used to measure size distribution as well as to study the flocculation kinetic of MNPs and F-MNPs, where the colloidal suspension was diluted to 6ppm in 3.0 ml of deionized water. As shown in Figure 1, the bare MNPs were started to flocculate from its initial hydrodynamic diameter at around 306 nm to form the larger clusters up to ~2000 nm in size. The flocculation of MNPs was probably due to the small particles tend to agglomerate to reduce the energy associated with high surface area to volume ratio of the nano sizes particles (20). Moreover, the large clusters formed may also because of the exited of attractive forces from van der Waals and magnetostatic interactions within the intermolecular MNPs (21) . Hence, surface modification/functionalization of MNPs is necessary to preserve good colloid stability and provide a better layer dispersion of MNPs on the membrane surface.

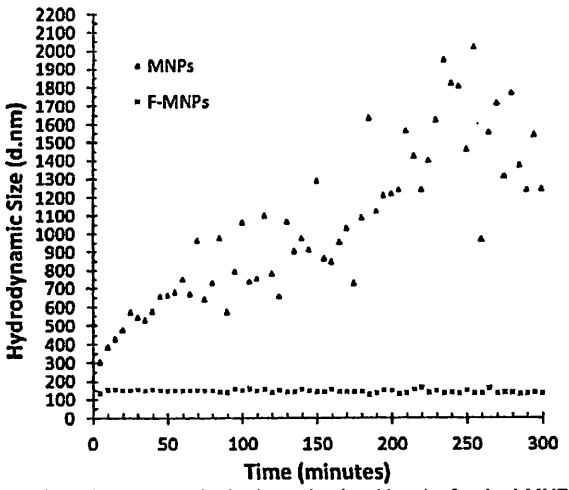

Figure 1 Flocculation kinetic profile presenting the average hydrodynamic size (d.nm) of naked MNPs and PSS coated F-MNPs vs. time (minutes)

As shown in Figure 1, MNPs functionalized using PSS (F-MNPs) were showed to have smaller hydrodynamic size compared to the bare MNPs at its initial stage. Moreover, the F-MNPs do not shown any obvious clustering behavior throughout the similar measuring time scale and behaved almost constant in size (145.49 ± 7.60 nm). This is a result of the steric (osmotic and elastic) and electrostatic repulsion existed between the F-MNPs because of the adsorbed polyelectrolyte layer that rendering the restricted intermolecular interactions among the polyelectrolyte coated particles (21), hence, enhance the MNPs stability.bATR-FTIR was used to characterize the model PES coated on the gold crystal to confirm the similar functionalities to those of the commercial PES membrane, as the spectra are shown in Figure 2, and the peak assignments (22) are given in Table 2. Both commercial PES membrane and PES coated onto gold quartz crystal demonstrated the same spectra, with the revealed characteristic vibrations at the peaks for the aromatic bands at 1576 and 1484 cm^{-1}, the symmetric vibration of the SO_2 groups at 1146 cm^{-1}, the Ar-O-Ar groups at 1236 cm^{-1}, and the C-S groups at 1484 cm^{-1}(23).

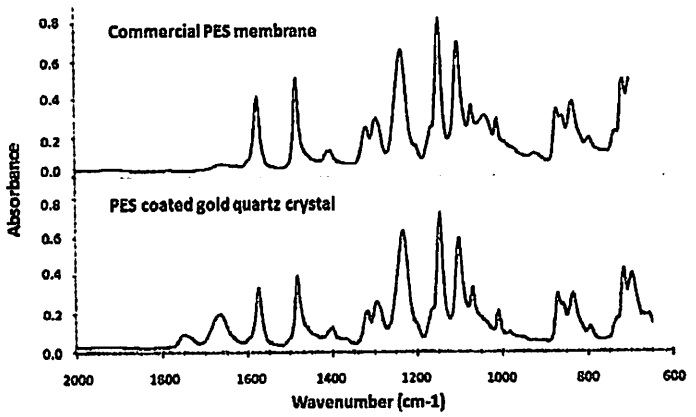

Figure 2 ATR-FTIR spectra for commercial PES membrane and PES coated on crystal

Table 2 Possible assignments of the FTIR spectra of PES membrane

Peak (cm^{-1})	Range given in the literature (22)	Assignment
1576	About 1580	Aromatic stretching vibration
1484	1460-1550	C-S stretch
1236	1275-1200	Ar-O-Ar stretching vibration
1146	1160-1120	SO_2 stretching

3.2 The F-MNPs adsorption onto PES model membrane

After functionalized MNPs with PSS, the F-MNPs were dispersed in either PSS or DI solution. The higher charge density of the PSS polyelectrolyte present in the solution is expected to demonstrate higher adsorption of the F-MNPs onto the PES polymer. However, at all conditions stated in Table 1, the adsorbed mass of the F-MNPs that dispersed in DI (conditions 1, 3 and 5) were relatively higher compared to the F-MNPs that was dispersed in PSS (conditions 2, 4 and 6). It was suspected due to the adsorption competition existing between the F-MNPs and free PSS polymer that deposited onto the coated surface of the quartz crystal. Thus, the average zeta potential for the polyelectrolytes and F-MNPs were evaluated, as shown in Table 3. From the Table 3, the free PSS polymer exhibited higher negative charge density compared to the F-MNPs. This is because the neutralization of charge occurs during the functionalization of MNPs (positive charge) with PSS (negative charge). Hence, free PSS polymer has the high affinity to adsorb onto the surface compare to the F-MNPs. In addition, of the lower component charge density for the F-MNPs were removed easier from the surface during the washing process (24). In regards, the F-MNPs that were dispersed in DI will be further used for the membrane fouling study by humic acid.

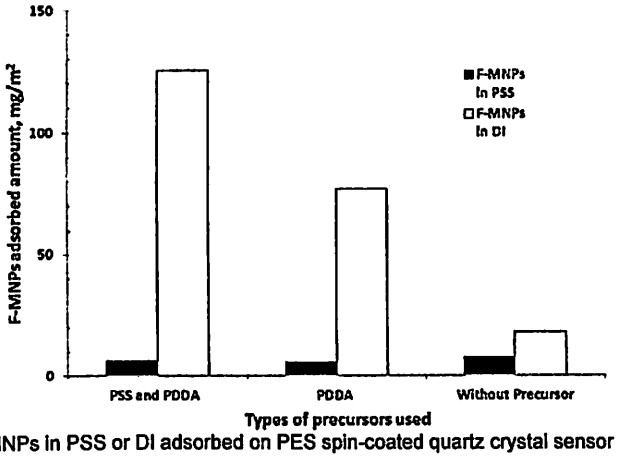

Figure 3 Amount of F-MNPs in PSS or DI adsorbed on PES spin-coated quartz crystal sensor with or without precursor

Table 3 Details on average zeta potential for polyelectrolytes and F-MNPs

Polyelectrolyte	Average zeta potential (mV)
PSS	-63.40±3.41
PDDA	+63.83±3.76
F-MNPs	-40.53±0.81

As for the effects of the present of precursor on the interactions with the F-MNPs, the results (Figure 3) shows that the lower adsorbed mass of F-MNPs on the PES surface in condition without precursor. This might because only weak hydrogen bonding and hydrogen-hydrogen interactions between F-MNPs and the PES membrane (25). In the comparison between the PDDA and PSS/PDDA precursors, the combination of PSS/PDDA precursors showing higher F-MNPs adsorbed mass (125.61 mg/m^2) than the sample using PDDA precursor (77.18 mg/m^2). This is due to the weakly adsorption of PDDA on the PES polymer which further caused the detachment of the PDDA together with the adsorbed F-MNPs from the PES surface. However, with the coated PSS precursor film covered the PES surface prior to the assembly of PDDA onto the crystal cell, the combinations (PES→PSS→PDDA) will forming a strong "polycation blanket" with a well charged outermost layer compare the previous combination contained only a layer of PDDA onto PES coated crystal cell (PES→PDDA) (26). Consequently, increased the adsorption of the F-MNPs on the polyelectrolyte multilayer (PES→ PSS→PDDA) was observed. Furthermore, the additional of the polyelectrolytes layers would expect to produce a more continuous film with increased surface charge (positive charge in this study) and more ion-exchange sites for the adsorption of F-MNPs (27); nevertheless, the number of bilayer of PSS/PDDA was limited to 1 to reduce the membrane thickness to avoid flux decline during the membrane application later.

3.2 Adsorption of HA foulant on the membrane surface

QCM-D was used to study the interactions between foulants and membrane surface, as shown in Table 4. The amount of HA adsorbed on pure PES membrane was much higher than that of the modified PES-Fe_3O_4 membrane. This is due to the increase of negative charge density and hydrophilicity on the surface of modified membrane that makes them less vulnerable to fouling. Almost all foulants were washed out (95.27%) from the modified PES-Fe_3O_4 membrane surface compared to only 33.63% of HA was removed or 56.15 ng/cm^2 retained on the PES membrane surface after the washing step. There is only weak interactions existed between the HA foulant and the modified membrane due to the impregnation of the negative charge and hydrophilicity properties of F-MNPs to the PES membrane, thus, reduced the attachment of HA foulant which has the similar negative charged. In contrast, the stronger attachment of HA foulant occurred when strong hydrophobic-hydrophobic interactions occurred between the HA and the unmodified PES membrane.

Table 4 Adsorption level for HA on different membrane surface and % mass of adsorbed layer (HA) removed by pure water

Membrane	Adsorbed Mass (ng/cm^2)	% HA Mass Removed after washing
PES	84.60	33.63
PES-Fe_3O_4	63.51	95.27

However, some minor HA foulant were still deposited on the surface of the modified membrane (3 ng/cm^2) due to the higher membrane roughness by the present of the nanoparticles. However, this deposited of HA foulant (3 ng/cm^2) was negligible compare to the unmodified PES membrane (56.15 ng/cm^2), showed the lower irreversible fouling occurs for the modified PES-Fe_3O_4 during fouling experiments.

■4.0 CONCLUSION

A good colloid stability of surface modification/functionalization of MNPs was successfully end-capped to the surface of PES membrane. In this study, membrane modified with F-MNPs in the present of PSS/PDDA existed as the precursors exhibited lower membrane fouling by the HA foulant, due to the present of highly negatively charge and hydrophilicity surface. The F-MNPs modified membrane developed in this work achieved high efficiency for the removal of humic substances up to 97.25%, which make the membrane processes more economical (longer life span of the membrane) and more sustainable.

Acknowledgement. The authors wish to thank the financial support granted by The Institution of Higher Education ERGS grant (6730013) and USM Membrane Cluster.

References

(1) V. Lahoussine-Turcaud, M. R. Wiesner, J.-Y. Bottero. 1990. *Journal of Membrane Science*. 52: 173.
(2) Z. Wang, Y. Zhao, J. Wang, S. Wang. 2005. *Desalination*. 178: 171.
(3) K. L. Jones, C. R. O'Melia. 2000. *Journal of Membrane Science*. 165: 31.
(4) K. L. Jones, C. R. O'Melia. 2001. *Journal of Membrane Science*. 193: 163.
(5) P. D. Peeva, T. Pieper, M. Ulbricht. 2010. *Journal of Membrane Science*. 362: 560.
(6) H. Ma, L. F. Hakim, C. N. Bowman, R. H. Davis. 2001. *Journal of Membrane Science*. 189: 255.
(7) R. Malaisamy, M. L. Bruening. 2005. *Langmuir*. 21: 10587.
(8) C. Mbareck, Q. T. Nguyen, O. T. Alaoui, D. Barillier. 2009. *Journal of Hazardous Materials*. 171: 93.
(9) J. H. Li, Y. Y. Xu, L. P. Zhu, J. H. Wang, C. H. Du. 2009. *Journal of Membrane Science*. 326: 659.
(10) D. McLachlan. 2010. *Water SA*. 36: 641.
(11) Y. Liu, A. Wang, R. O. Claus. 1997. *Applied Physics Letters*. 71: 2265.
(12) J. S. Taurozzi, H. Arul, V. Z. Bosak, A. F. Burban, T. C. Voice, M. L. Bruening, V. V. Tarabara. 2008. *Journal of Membrane Science*. 325: 58.
(13) C. Schlemmer, W. Betz, B. Berchtold, J. Rühe, S. Santer. 2009. *Nanotechnology*. 20.
(14) K. L. Chen, M. Elimelech. 2006. *Langmuir*. 22: 10994.
(15) D. Xu, C. Hodges, Y. Ding, S. Biggs, A. Brooker, D. York. 2010. *Langmuir*. 26: 18105.
(16) E. Arkhangelsky, F. Wicaksana, C. Tang, A. A. Al-Rabiah, S. M. Al-Zahrani, R. Wang. 2012. *Water Research*. 46: 6329.
(17) A. E. Contreras, Z. Steiner, J. Miao, R. Kasher, Q. Li. 2011. *Environmental Science & Technology*. 45: 6309.
(18) M. Hashino, K. Hirami, T. Katagiri, N. Kubota, Y. Ohmukai, T. Ishigami, T. Maruyama, et al. 2011. *Journal of Membrane Science*. 379: 233.
(19) G. Sauerbrey. 1959. *Zeitschrift für Physik*. 155: 206.
(20) A.-H. Lu, E. L. Salabas, F. Schüth. 2007. *Angewandte Chemie International Edition*. 46: 1222.
(21) J. K. Lim, D. C. J. Chieh, S. A. Jalak, P. Y. Toh, N. H. M. Yasin, B. W. Ng, A. L. Ahmad. 2012. *Small*. 8: 1683.
(22) J. Coates. 2000. *Interpretation of Infrared Spectra, A Practical Approach. Encyclopedia of Analytical Chemistry*. New York: John Wiley & Sons Ltd
(23) C. Liu, R. Bai. 2005. *Journal of Membrane Science*. 267: 68.
(24) O. J. Rojas, M. Ernstsson, R. D. Neuman, P. M. Claesson. 2002. *Langmuir*. 18: 1604.
(25) F. Diagne, R. Malaisamy, V. Boddie, R. D. Holbrook, B. Eribo, K. L. Jones. 2012. *Environmental Science & Technology*. 46: 4025.
(26) F. Hua, Y. M. Lvov. 2008. *Layer-by-layer assembly. The New Frontiers of Organic and Composite Nanotechnology*. Amsterdam: Elsevier.
(27) G. Liu, D. M. Dotzauer, M. L. Bruening. 2010. *Journal of Membrane Science*. 354: 198.

The 10th international conference on Membrane Science & Technology 2012 (MST2012)

"Membrane for Sustainable Energy & Environment"

22-24 August 2012

Bangkok, Thailand

Development of Magnetite Nano-composite Membrane for Membrane Defouling

A. N. Atiah [a], Q. H. Ng [a], A.L. Ahmad [a], S.C. Low [a*]

[a] School of Chemical Engineering Campus, Universiti Sains Malaysia, Seri Ampangan, 14300 Nibong Tebal S.P.S. Penang, Malaysia
* chsclow@eng.usm.my

Abstract – This research proposes to untangle the membrane fouling by introducing nanostructured magnetite (Fe_3O_4) colloids into the polymeric membrane. In present study, nanostructure magnetite nanoparticles (MNPs) were synthesized via co-precipitation method with ammonium hydroxide and sodium hydroxide as the precipitation agents at different pH condition. The synthesized MNPs were functionalized with poly(diallyldimethylammonium chloride) (PDDA) and then spin coated on the surface of the ultrafiltration cellulose acetate (CA) membrane. Intrinsic properties for this nano-composite membrane, in regards to the physical structures, surface negative charge density and the membrane filtration performance, on surface fouling by humic acid solutions were investigated. Experimental results demonstrated that, the nano-composite membrane has significantly reduced the humic acid fouling on the membrane surface. This could be explained by the electrostatic interactions between negatively charged humic acid molecules and the nano-composite membrane. Throughout the study, the results provide some fundamental insights into the physical interactions that governing the membrane fouling during filtration.

Keywords: Fouling; Magnetite nanoparticles; Humic acids; Nano-composite membrane; Water treatment

1. Introduction

In recent years, various water treatment technologies are actively being pursued in both academic world and industry due to the rapid deterioration of water quality worldwide. The stringent regulations for drinking water quality have stimulated the membrane filtration to become one of the best alternatives that replacing the conventional drinking water treatment technologies [1-3].

Fouling remains a critical issue in many water filtration processes and serves as the dominant factor that restricts its widespread application [3, 4]. The fouling causes a rapid irreversible loss of flux through the membrane which leads to the progressive deterioration of membrane performance [5].

Periodic hydraulic backwash procedures were usually employed in reducing the effects of fouling. However, the used of hydraulic backwash is practical in removing the reversible foulant. Some deposited matter on the membrane surface and inside the pores cannot be removed and formed the irreversible part of fouling [6].

Recently, the synthesized of nanosized magnetic material have drawn much attention due to their unique properties and potential applications in biomedical [7, 8], heat transfer enhancement and environmental applications [9-11]. Magnetite (Fe_3O_4) nanoparticles are preferred because of its high magnetic susceptibility, non-toxic, low cost instrument and low detection limit [12].

Currently the magnetic actuated membrane is an improvement of the membrane process in removing the foulant. The nano-composite membrane consist of a highly elastic polymer matrix with embedded nanosized of magnetic particles [13], which is sensitive to the magnetic field. In the presence of a local magnetic field, the magnetic membrane could be stiffened. This will reduced the object and membrane contact area and allowed the object to be either relocated or released.

The aimed of the present study is to untangle the fouling mechanism through magnetically actuated nano-composite membrane. The research efforts were dedicated to formularize a simple experimental protocol for surface functionalization of the polymeric membrane. Through electrostatic interaction between nanostructure magnetite (Fe_3O_4) colloids and

membrane, it provided the flexibility on the motion control of magnetite nanoparticles on the membrane surface. Defouling performance of the nano-composite membrane was tested accordingly by using humic acid substances as the foulant.

2. Research methodology

2.1 Materials

Iron (III) chloride hexahydrate ($FeCl_3.6H_2O$), iron (II) chloride tetrahydrate ($FeCl_2.4H_2O$), sodium hydroxide (NaOH) and hydrochloric acid fuming 37% (HCL) were purchased from Merck (Darmstadt, Germany). Ammonium hydroxide solution 28% in water (NH_4OH) and poly(diallyl-dimethyl ammonium chloride) (PDDA) were supplied by Sigma-Aldrich (St. Louis, MO). All chemicals used in this study were analytical grade standards and used without further purification.

2.2 Synthesis of Fe_3O_4 nanoparticles

The magnetite nanoparticles were prepared via co-precipitation method. 4mL of 0.5M $FeCl_3 \cdot 6H_2O$ was mixed with 1mL of 1M $FeCl_2 \cdot 4H_2O$ at 25°C and stirred at stirring speed of 1100rpm. A 25mL of NH_4OH or NaOH (with pH ranging from 9 to 14) that acted as the precipitating agent was immediately added into the mixture and stirred for 30min. Upon the completion of the co-precipitation process, the synthesized magnetite nanoparticles were collected by an NdFeB permanent magnet. Collected magnetite nanoparticles were washed with deionized water (DI) and centrifuged to ensure that pure magnetite was obtained (repeated three times). The magnetites were then sonicated to allow monodisperse of magnetite in DI water.

2.3 Functionalization of Fe_3O_4 nanoparticles

1000 ppm of magnetite nanoparticles suspension was prepared using DI water and sonicated. Similarly, 0.01667 g/mL of PDDA was prepared and undergo sonication. The pH of both magnetite nanoparticles (MNPs) suspension and PDDA solution was adjusted to pH~8.0 to facilitate physisorption of PDDA on MNPs via electrostatic attraction for 1 day in rotator mixer. The PDDA-coated magnetite nanoparticles were then collected using an Nd-FeB permanent magnet and pre-washed before dispersed in DI water.

2.4 Development of Nano-composite membrane

The nano-composite membrane was prepared using Flat sheet CA membrane was placed onto the glass plate and fitted onto the vacuum chuck of spin coater. Subsequently, polymer solution containing PDDA-coated magnetite nanoparticles was dispersed onto the membrane surface at rotation speed of 300 rpm and rotation time of 900s until a homogeneous thin film polymer was formed. The nano-composite membrane was then air dried.

2.5 Membrane performance test

The performance of the nano-composite membrane toward reducing the nano-composite membranes were test. CA membranes were cut into the dimension of 1×1cm and labeled as sample 1 and sample 2. Both samples were immersed in humic acid (HA) solutions for 13 hours, where the external magnetic field (magnetic bar) was imposed to the sample 1. The introduction of external magnetic field at sample 1 would induce magneto rotation motions of MNPs that bound on the membrane surface and further removed the deposited HA molecules. After 13 hours, the membrane samples were air dried for 24 hours prior analyzed using ATR-FTIR.

2.6 Characterization

2.6.1 Particle size and polydispersity index of Fe_3O_4 nanoparticles

Average particle size and polydispersity index of magnetite nanoparticles were determined using DLS (Malvern Instruments Nanosizer ZS). The light scattering intensity autocorrelation function was fitted by the CONTIN algorithm to produce an intensity-weighted distribution of hydrodynamic radii. For DLS measurement, the sample was prepared by dispersed the 0.01ml of magnetite suspension to 3.5ml of DI water.

2.6.2 Attenuated Total Reflection Fourier Transform Infrared (ATR-FTIR)

The fouling level of the nano-composite membrane was investigated using Thermo Scientific FTIR spectrometer system (NICOLET iS10, USA). The membranes spectra were analyzed using Diamond crystal over wavenumber range of 4000-600 cm^{-1} with 32 scans at 4 cm^{-1} resolutions.

3. Results and discussion

3.1 Synthesis of magnetite nanoparticles

Ammonium hydroxide and sodium hydroxide were selected as the precipitation agents to synthesis the magnetite nanoparticles under different pH condition (from pH 9 to pH 14). It was observed that, different precipitate colour were obtained when co-precipitation process were carried under the different pH conditions. Black precipitate solutions were observed at pH 11 and pH 12 in Fig. 1 and pH 14 in Fig. 2. These solutions were shown to have magnetophoretic responses when imposed to the external magnetic field (magnetic bar). In this regards, the synthesized MNPs were magnetite responsive

which is expected able to perform the magneto rotation motions when bound on the membrane surface and further detached the foulants away from the membrane surface.

However, clear yellow solutions were observed throughout the reaction of NH_4OH at pH 9 and pH 10 in Fig. 1 and NaOH from pH 9 and pH 12 in Fig. 2. These yellow colour solutions were the intermediate form of solutions due to the insufficient of precipitation agent. This intermediate forms would change if the precipitation agent continuously added to the process until the OH^- ions sufficient to form MNPs. Knowing that, NaOH solution contained of higher density of OH^- than NH_4OH solution with the same molarities. However the used of strong alkaline media such as NaOH, can caused the formation of non-magnetic iron compound [14] such as α-FeOOH and other ion compounds [15].

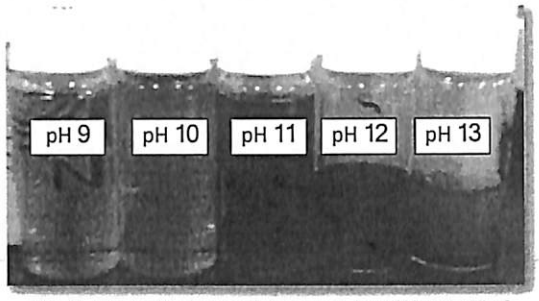

Fig. 1. Magnetite nanoparticle prepared at different pH of ammonium hydroxide (NH_4OH)

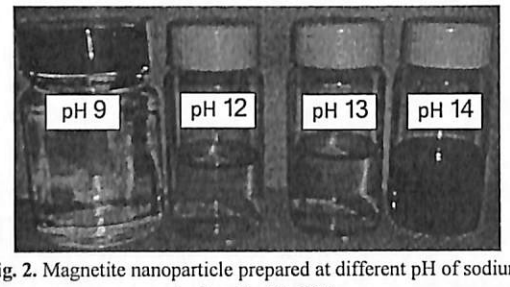

Fig. 2. Magnetite nanoparticle prepared at different pH of sodium hydroxide (NaOH)

Fluctuate trends were observed for both hydrodynamic diameter size (Fig. 3) and PDI (Fig. 4) of MNPs when NH_4OH was used as the precipitation agent in co-precipitation process. The interesting finding is that both highest and lowest readings were found at the narrow pH range within pH 11 to pH 12, respectively. MNPs showed to have the average hydrodynamic size of 1046.4 ± 200 nm at pH 11 and only 132.1 ± 0.55 nm at pH 12. PDI was also followed the trend of hydrodynamic size where showed to be 0.798 at pH 11 and monodisperse 0.253 at pH 12. The monodisperse of MNPs at pH 12 might due to electrostatic interaction that leads the repulsion between the negatively charge MNPs. MNPs carry negative surface charge at pH higher than its point zero charge [16, 17].

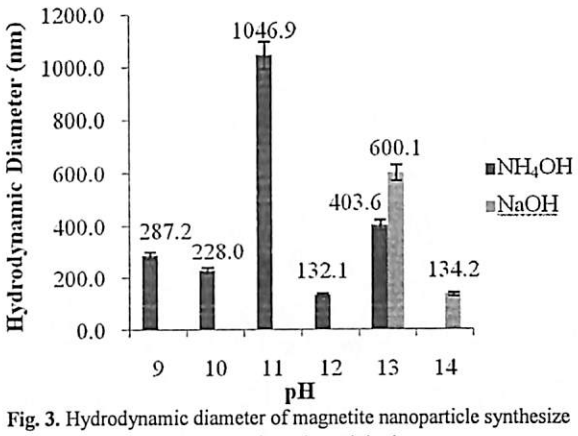

Fig. 3. Hydrodynamic diameter of magnetite nanoparticle synthesize at different pH ratio and precipitation agent

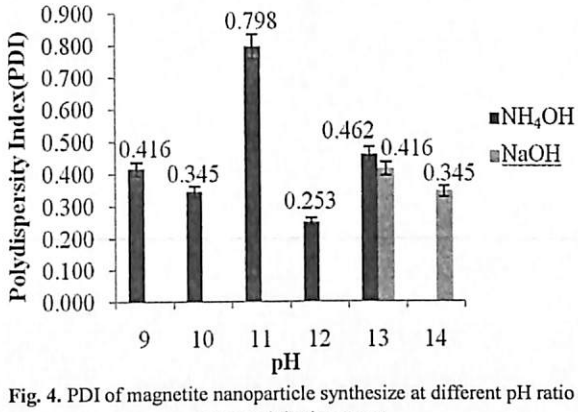

Fig. 4. PDI of magnetite nanoparticle synthesize at different pH ratio and precipitation agent

As for NaOH, MNPs were only able to produce at pH 13 or higher. This might be due to the density of OH^- ions in the NaOH solution at certain pH. It is well known that pH value is responsible for the charge density of OH^- ions, which responsible for the formation of MNPs. NaOH solution at pH below 12 resulted to have low density of ions OH^-, thus, restricted the formation of magnetic responsive nanoparticles and maintained as intermediate form of solutions. However, the interest was focused on pH 14 since the MNPs were magnetite responsive (black color of solution) under this pH condition. At pH 14, the produced MNPs appeared in small hydrodynamic diameters of 134.2 ± 2.27 nm and low PDI of 0.345. Under the consideration of both small hydrodynamic diameter and low PDI, both NH_4OH and NaOH were giving the similar characteristics of produced MNPs. However, NH_4OH was selected as precipitation agent for further study due to the lower pH condition (pH 12) was preferred for membrane filtration process.

3.2 Defouling performance of magnetite nano-composite membrane

Membrane defouling study was carried out by immersing the membrane sample in HA solution for 13 hours. The fouling level of HA onto membrane surface was analyzed using ATR-FTIR spectrophotocopy, as shown in Fig. 5. Samples 1 (membrane that exposed to the external magnetic field) and sample 2 (membrane that did not exposed to the external magnetic field) showed two significantly different transmission peaks at 1733 and 1636-1581 cm^{-1} wavenumber respectively.

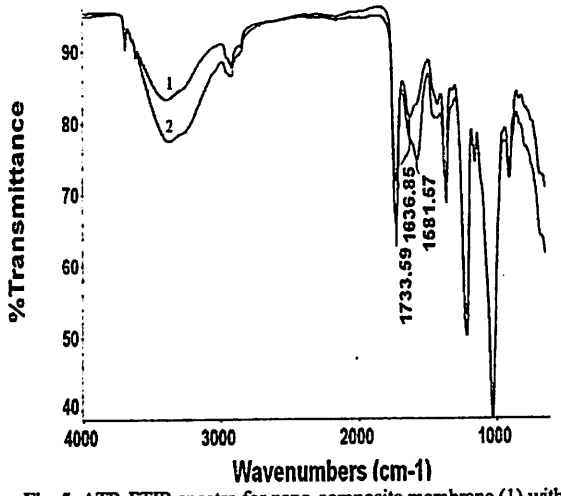

Fig. 5. ATR-FTIR spectra for nano-composite membrane (1) with and (2) without the introduction of external magnetic field

The peak at 1733 cm^{-1} could be attribute to the presence of C=O stretching in carboxylic acid groups. The peak at 1636 and 1581 cm^{-1} attribute to the presence of C=C and N-H group respectively. At peak of 1733 cm^{-1}, sample 1 with the exposed to the external magnetic field was found to have a stronger absorption band and vice versa at the overlapping peak of 1581-1636cm^{-1}. Based on these two peaks, it shows that the membrane sample 2 contained higher number of HA molecules that deposited on the membrane surface. These prove that, magnetite nano-composite membrane with the introducing of external magnetic field was could detached the HA precipitation on the membrane surface, thus, reduced the membrane fouling. When the magnetic nano-composite membrane was exposed to the external magnetic field, it will promote the alignment of MNPs that bound onto the membrane surface in one direction. In this regards, the magneto-induced rotation motions within the membrane polymer matrix were performed if two opposite directions were take placed in sequence. The rotational motions of the MNPs, promoted the detachment of the HA from the CA membrane. In turn, HA could easily remove from the MNPs and membrane surface and reduce fouling.

4.0 Conclusion

In present study, MNPs with small particle size and polydispersity index were successfully synthesis by using 25mL of NH_4OH at pH 12 with average hydrodynamic diameters of 132.1nm and PDI of 0.253. The synthsised MNPs were further stabilized using PDDA and coated onto CA membrane to form magnetic nano-composite membrane. The results demonstrated high efficiency of the removal of humic acid from the membrane surface, in the advantage that the movement of the magnetically responses of MNPs on the membrane surface suppresses fouling.

Acknowledgment

The authors wish to thank the financial support granted by The Institution of Higher Education ERGS grant (6730013) and USM Membrane Science and Technology Cluster.

References

[1]. Z. Domany, *et al.*, "Humic substances removal from drinking water by membrane filtration," *Desalination*, vol. 145, pp. 333-337, 2002.

[2]. V. Siyanytsya, *et al.*, "Natural organic matter removal from water by complexation-ultrafiltration," *Desalination*, vol. 223, pp. 91-96, 2008.

[3]. X. Fu, *et al.*, "Effect of surface morphology on membrane fouling by humic acid with the use of cellulose acetate butyrate hollow fiber membranes," *Journal of Membrane Science*, vol. 320, pp. 483-491, 2008.

[4]. D. B. Mosqueda-Jimenez, *et al.*, "Fouling characteristics of an ultrafiltration membrane used in drinking water treatment," *Desalination*, vol. 230, pp. 79-91, 2008.

[5]. K. Katsoufidou, *et al.*, "A study of ultrafiltration membrane fouling by humic acids and flux recovery by backwashing: Experiments and modeling," *Journal of Membrane Science*, vol. 266, pp. 40-50, 2005.

[6]. G. F. Crozes, *et al.*, "Impact of ultrafiltration operating conditions on membrane irreversible fouling," *Journal of Membrane Science*, vol. 124, pp. 63-76, 1997.

[7]. J. Mürbe, *et al.*, "Synthesis and physical characterization of magnetite nanoparticles for biomedical applications," *Materials Chemistry and Physics*, vol. 110, pp. 426-433, 2008.

[8]. K. Nishio, *et al.*, "Preparation of size-controlled (30–100 nm) magnetite nanoparticles for biomedical applications," *Journal of Magnetism and Magnetic Materials*, vol. 310, pp. 2408-2410, 2007.

[9]. X. M. Li, *et al.*, "Magnetic Fe 3O 4 nanoparticles: Synthesis and application in water treatment," *Nanoscience and Nanotechnology - Asia*, vol. 1, pp. 14-24, 2011.

[10]. W. Yantasee, *et al.*, "Removal of heavy metals from aqueous systems with thiol functionalized superparamagnetic nanoparticles," *Environmental Science and Technology*, vol. 41, pp. 5114-5119, 2007.

[11]. F. Ge, *et al.*, "Effective removal of heavy metal ions Cd 2+, Zn 2+, Pb 2+, Cu 2+ from aqueous solution by polymer-modified magnetic nanoparticles," *Journal of Hazardous Materials*, vol. 211-212, pp. 366-372, 2012.

[12]. H. Guo, *et al.*, "Application of magnetic nanoparticles for UF membrane integrity monitoring at low-pressure

operation," *Journal of Membrane Science,* vol. 350, pp. 172-179, 2010.

[13]. C. Schlemmer, *et al.*, "The design of thin polymer membranes filled with magnetic particles on a microstructured silicon surface," *NANOTECHNOLOGY,* p. 9, 2009.

[14]. G. Gnanaprakash, *et al.*, "Effect of initial pH and temperature of iron salt solutions on formation of magnetite nanoparticles," *Materials Chemistry and Physics,* vol. 103, pp. 168-175, 2007.

[15]. I. Martínez-Mera, *et al.*, "Synthesis of magnetite (Fe3O4) nanoparticles without surfactants at room temperature," *Materials Letters,* vol. 61, pp. 4447-4451, 2007.

[16]. J.-D. Hu, *et al.*, "Effect of dissolved organic matter on the stability of magnetite nanoparticles under different pH and ionic strength conditions," *Science of The Total Environment,* vol. 408, pp. 3477-3489, 2010.

[17]. E. Illés and E. Tombácz, "The effect of humic acid adsorption on pH-dependent surface charging and aggregation of magnetite nanoparticles," *Journal of Colloid and Interface Science,* vol. 295, pp. 115-123, 2006.

FINANCE STATEMENT

Purchase Requisition ▸ Purchase Order ▸ Suppliers ▸ Maintenance ▸ Financials ▸ Coda Info ▸ Reports ▸ Admin ▸

UserCode: NORMIE / USMKCTLIVE / PJKIMIA **Program Code: Votebook9100** **Current Program : Votebook (Header)**

Current Date : 03/03/2014 2:17:48 PM **Version: 15.19, Last Updated at 06/02/2013** **DB: 13.00, 9/18/2010 VB: 13.01, 3/14/2011** **Switch Language : English /Malay**

Wildcard : eg. Like 100%, Like 10%1, Like %1

Element 1: % Element 2: % Element 4: PJKIMIA

Element 5: 6730013 Year: 2014

Detail	Excel	Budget Rule	Budget Control	Account Description	Budget Account Code	Roll over	Budget	Cash Received	Advanced	Commit	Actual	Available	Percentage
Detail	Excel	163	T	Pembangunan Penyelidikan	203.111.0.PJKIMIA.6730013	-2,311.23	0.00	0.00	0.00	0.00	2,600.00	-4,911.23	0.00%
		163	T	SubTotal		-2,311.23	0.00	0.00	0.00	0.00	2,600.00	-4,911.23	0.00%
Detail	Excel	164	T	Pembangunan Penyelidikan	203.221.0.PJKIMIA.6730013	11,268.00	0.00	0.00	0.00	0.00	0.00	11,268.00	0.00%
Detail	Excel	164	T	Pembangunan Penyelidikan	203.224.0.PJKIMIA.6730013	-93.84	0.00	0.00	0.00	0.00	0.00	-93.84	0.00%
Detail	Excel	164	T	Pembangunan Penyelidikan	203.227.0.PJKIMIA.6730013	78.39	0.00	0.00	0.00	0.00	2,810.00	-2,731.61	0.00%
Detail	Excel	164	T	Pembangunan Penyelidikan	203.229.0.PJKIMIA.6730013	-13,172.18	0.00	0.00	0.00	0.00	0.00	-13,172.18	0.00%
		164	T	SubTotal		-1,919.63	0.00	0.00	0.00	0.00	2,810.00	-4,729.63	0.00%
Detail	Excel	165	T	Pembangunan Penyelidikan	203.335.0.PJKIMIA.6730013	9,644.00	0.00	0.00	0.00	0.00	0.00	9,644.00	0.00%
		165	T	SubTotal		9,644.00	0.00	0.00	0.00	0.00	0.00	9,644.00	0.00%
		9999		GrandTotal		5,413.14	0.00	0.00	0.00	0.00	5,410.00	3.14	0.00%